Surface Documentation of a 3-D Supersonic, Shock-Wave/ Boundary-Layer Interaction

Jeffrey K. Wideman, University of Missouri, Columbia, Missouri
James L. Brown, Ames Research Center, Moffett Field, California
John B. Miles, University of Missouri, Columbia, Missouri
Oktay Özcan, Istanbul Technical University, Istanbul, Turkey

June 1994

NASA

National Aeronautics and
Space Administration

Ames Research Center
Moffett Field, California 94035-1000

NOMENCLATURE

a	constant in Sun and Childs' wall-wake correlation
A	coefficient defined by equation 3-7, also the sum of α and s
B	coefficient defined by equation 3-8
C_f	local skin-friction coefficient ($\equiv \tau / \frac{1}{2}\rho_\infty U_\infty^2$)
C_{f_x}	local streamwise skin-friction coefficient ($\equiv \tau_x / \frac{1}{2}\rho_\infty U_\infty^2$)
C_{f_z}	local transverse skin-friction coefficient ($\equiv \tau_z / \frac{1}{2}\rho_\infty U_\infty^2$)
C_p	specific heat at constant pressure
C_1	constant defined by equation 4-9
d_f	laser Doppler velocimetry fringe spacing
f	frequency
g	acceleration due to gravity [$= 9.81$ m/s^2]
h	convective heat transfer coefficient
k	incremental fringe number, also turbulent kinetic energy
l_a	attachment length parameter
l_{pk}	peak pressure length parameter
l_s	separation length parameter
l_u	upstream influence length parameter
M	Mach number
M_∞	free-stream Mach number
n_{air}	refractive index of air
n_o	refractive index of oil
n_s	refractive index of substrate
N	fringe number
N_o	reference fringe number
N'	effective fringe number
P	local surface pressure
P_a	afterbody pressure
P_{pk}	peak pressure
P_s	separation pressure
P_t	total pressure
P_∞	free-stream static pressure
Pr^*	Prandtl number based on Eckert reference temperature
q''	heat flux
r	radial coordinate from cylinder centerline, also temperature recovery factor
r_c	correlation coefficient
R	calculated result based on a set of measurements
Re	Reynolds number
Re^*	Reynolds number based on Eckert reference temperature
s	oil viscosity-temperature coefficient
St^*	Stanton number based on Eckert reference temperature
t	time
t_c	temperature corrected time

t_f	$\equiv t_o + t_i$
t_i	incremental oil-flow time
t_o	reference oil-flow time
t'	effective oil-flow time
T	temperature
T_{aw}	adiabatic wall temperature
T_r	reference temperature
T_s	surface temperature
T_t	total temperature
T_{tc}	thermocouple temperature
T_w	wall temperature
T^*	Eckert reference temperature
T_∞	free-stream static temperature
u, v, w	streamwise, vertical, and transverse instantaneous velocities
u', v', w'	streamwise, vertical, and transverse fluctuating velocities
U, V, W	streamwise, vertical, and transverse mean velocities
U_τ	friction velocity
U^*	Van Driest generalized velocity
U_∞	free-stream velocity
W	Coles' wake function
x	streamwise coordinate, also distance from oil leading edge to measurement beam
x_a	location of attachment
x_j	location of cylinder-flare junction along azimuth ϕ
x_{pk}	location of peak pressure
x_s	location of separation
x_u	location of upstream influence
y	vertical coordinate measured radially from model surface, also oil thickness
z	transverse coordinate
α	coefficient of expansion
α_{oil}	slope of oil leading edge
β	flow angle with respect to free-stream direction
γ	specific heat ratio
δ	boundary-layer thickness
δ_{oil}	stationary oil thickness
Δ	uncertainty
Δ_p	optical path length difference
ϵ	correction parameter, also turbulent dissipation rate
θ_t	incident beam angle
θ_t	transmitted beam angle
κ	Von Kármán constant, also half-angle between laser Doppler velocimetry beams
λ	laser wavelength
μ_∞	free-stream absolute viscosity [N s/m^2]
μ_o	absolute viscosity [N s/m^2] of oil
ν_∞	free-stream kinematic viscosity [m/s^2]

ν_r	reference kinematic viscosity [m^2/s = 10^6 cs] of oil
ν_o	kinematic viscosity [m^2/s = 10^6 cs] of oil
Π	wake-strength profile parameter
ρ	density
ρ_o	density of oil
ρ_r	reference density of oil
ρ_t	total density
ρ_∞	free-stream density
ρ^*	density based on Eckert reference temperature
σ	standard deviation
τ	local shear stress at the wall
τ_c	corrected local shear stress at the wall
τ_x	local streamwise shear stress at the wall
τ_z	local transverse shear stress at the wall
ϕ	azimuthal coordinate

Units

atm	atmosphere
cc	cubic centimeter
cm	centimeter
cs	centistoke
deg	degrees
Hz	hertz
K	kelvin
kPa	kilopascal
kg	kilogram
m	meter
mm	millimeter
mW	milliwatt
MHz	megahertz
MPa	megapascal
N	newton
psi	pounds per square inch
s	seconds
W	watt
μm	micrometer

SUMMARY

An experimental study has been conducted in a three-dimensional (3-D) supersonic shock-wave/ boundary-layer interaction (SW/BLI) to provide accurate data for 3-D turbulence modeling and computational fluid dynamics (CFD) code validation. The experiment was performed in the High Reynolds Channel 1 wind tunnel at NASA Ames Research Center. The test was conducted at a Mach number of $M_\infty = 2.89$ and at a Reynolds number of $Re = 15 \times 10^6/\text{m}$. The model consisted of a sting-supported ogive-nose cylinder aligned with the tunnel axis and a 20° half-angle conical flare offset 1.27 cm from the cylinder centerline. The generated shock system was verified to be steady by spark schlieren visualization. The emphasis of the study was the acquisition of 3-D skin-friction data by a laser interferometric skin friction instrument. Extensive surface pressure measurements were obtained in 15° intervals around the cylinder and flare. Additional measurements included surface oil flow and laser light sheet illumination to document the flow topology. Skin-friction measurements are proving to be a challenging test of CFD predictive capability. However, at the present time there is a limited amount of accurate skin-friction data in complex flows such as in 3-D SW/BLI. The laser interferometric skin friction technique is advantageous as compared to other skin-friction measurement techniques for application in complex flows like the present since it is nonintrusive and is capable of performing measurements in flows with large shear and pressure gradients where the reliability of other techniques is questionable. Thus, the present skin-friction data will prove valuable for 3-D turbulence modeling and CFD code validation efforts.

1 INTRODUCTION

1.1 Background and Motivation

The flow field surrounding aerodynamic vehicles can be quite complex. The nature of practical flows is typically compressible, turbulent, and three-dimensional (3-D). In addition, at supersonic speeds shock waves exist which interact with boundary layers on flight surfaces. The adverse pressure gradient associated with shock-wave/boundary-layer interactions (SW/BLI) can cause the boundary layer to separate, thus altering aircraft performance. Hence, there is a need to better understand and predict these SW/BLI.

Over the years, computational fluid dynamics (CFD) has augmented the experimental research on SW/BLI. Although a full computational simulation of flow fields instead of wind tunnel documentation is appealing, much work needs to be done before complete computational solutions to 3-D SW/BLI problems can be reliably achieved. In solving the Navier–Stokes equations, closure of the equation set is achieved by modeling the turbulence. These turbulence models need to be developed through reliance on measurements of the physical phenomenon of the interaction. There is also a need to provide experimental data to validate the computational results from CFD. Thus, experiments and computations are complementary tools that can extend the present understanding of fluid dynamics and produce methods by which SW/BLI can be accurately predicted.

The present study (see also ref. 1) was undertaken, in the context of previous related SW/BLI studies (refs. 2–9), with the goal of acquiring accurate data in a 3-D SW/BLI to guide the development of turbulence modeling and for the validation of CFD codes. Because of the scarcity of accurate skin-friction data in SW/BLI, the emphasis of this study was on the acquisition of skin-friction data. A laser interferometric skin friction (LISF) instrument was used to acquire the skin-friction data in a complex flow characterized by large pressure and shear gradients where the reliability of other techniques would be questionable.

1.2 Scope of Investigation

The experiment was conducted in the NASA Ames High Reynolds Channel 1 (HRC-1) wind tunnel on a 3-D, supersonic SW/BLI. The model consisted of a sting-supported cylinder with its axis aligned parallel to the flow. A 1.1 cm thick axisymmetric, turbulent boundary layer developed on this cylinder and encountered a 20° half-angle conical flare which was mounted on the cylinder. The axis of this conical flare was offset 1.27 cm from the cylinder centerline to provide a highly swept 3-D geometry (fig. 1). The experiment was performed at a Mach number of $M_\infty = 2.89$ and a unit Reynolds number of $Re = 15 \times 10^6/\text{m}$. The generated shock system was verified to be steady through the schlieren technique. The highlight of the study was the acquisition of 3-D skin-friction data by a laser interferometric skin friction (LISF) instrument along various azimuthal planes at several locations. These included measurements located upstream of the interaction on the cylinder, through the interaction on the flare ramp, and along the afterbody for three azimuths. Surface pressure measurements were obtained in 15° intervals around the cylinder and flare. The velocity profile in the undisturbed boundary layer was measured with a laser Doppler velocimetry (LDV) system. Additional measurements included surface oil flow and laser light sheet illumination, which were used to document the flow topology.

2

2 EXPERIMENTAL DESCRIPTION

2.1 Test Facility and Conditions

This experimental study was conducted at NASA Ames Research Center in the High Reynolds Number Channel 1 wind tunnel. High-pressure air for the blow-down facility, supplied from an extensive 20.7 MPa reservoir, passed through a control valve, a 2.14 m diameter settling chamber, a contraction section, a nominal Mach 3 nozzle, and then through the test section followed by a diffuser. The air then discharged into as many as five vacuum spheres, each of diameter 22.9 m. Typically, for a 1.7 atm stagnation pressure, the tunnel could be operated for approximately 12 minutes before a shock wave would form in the diffuser section and propagate upstream into the test section. However, during the laser light illumination and the laser interferometric skin friction phases of the study only one vacuum sphere was available for use, restricting the run duration to 3 minutes. The tunnel can be configured with different nozzles and test sections. The test section was 25.4 cm wide by 38.1 cm high. Optical access was provided by two 29.4 cm by 38.1 cm optical crown glass windows, one on each side of the tunnel.

The average operating conditions for the study are given in table 1. All test runs were conducted at a nominal total pressure of 172.37 kPa (1.7 atm). A nominal value of 280 K was chosen to represent the total temperature for this test. The total temperature typically would decrease approximately 10 K during a 3 minute run. The total temperature would vary from run to run depending on previous history of the high-pressure air reservoir. Seasonal variations in the total temperature were also observed, being about 10 K lower in the winter. The Mach number in the test chamber in the vicinity of the model was $M_\infty = 2.89$ and the nominal free-stream velocity was 593 m/s. The unit Reynolds number was $Re = 15.0 \times 10^6$/m. The boundary-layer thickness just upstream of the interaction was determined to be $\delta = 1.10$ cm.

2.2 Test Model

The axisymmetric boundary layer developed on a 5.08 cm diameter stainless steel cylinder aligned with the tunnel axis (fig. 1). A 40.0 cm long cusped ogive nose minimized the generation of extraneous shock-waves. The nose section was followed by a 36.5 cm uninstrumented cylinder and a 30.5 cm instrumented cylinder, both composed of stainless steel. The instrumented cylinder was, in turn, connected to another cylindrical section which was supported by a sting located well downstream of the interaction region. The instrumented cylinder possessed four rows of static pressure taps along azimuths spaced 90° apart. Each row consisted of 22 taps with a streamwise spacing of 0.5 cm. The particular model was chosen because the shock system was found to be steady via comparison of several spark schlieren photographs (fig. 2).

The instrumented 3-D flare slid over and was secured to the most downstream cylindrical section. The flare was fabricated as if it were a 20° half-angle axisymmetric cone with its centerline displaced 1.27 cm from the centerline of the cylinder axis. The flare was terminated with a 12.70 cm diameter afterbody, the centerline of which matched that of the cylinder. The length along the inclined ramp

was 11.14 cm along both the $\phi = 0°$ and the $\phi = 180°$ azimuth. The length of the afterbody varied from 12.06 cm along the $\phi = 0°$ azimuth to 5.08 cm along the $\phi = 180°$ azimuth. The cylinder-flare junction along $\phi = 180°$ was located 6.98 cm downstream of $\phi = 0°$. The streamwise locations of the cylinder-flare junction for various azimuths are given in table 2.

The surface of the aluminum flare was anodized black. The flare possessed 13 rows of 22 static pressure taps for a total of 286 taps. The rows of taps were along both sides of the symmetry plane so that the pressure measurements, when combined, would document one region of symmetry ($\phi = 0° - 180°$) in intervals of 15°. The first 19 taps of each row were located along the ramp with a streamwise spacing of 0.50 cm. Three taps were located along the flare afterbody with a streamwise spacing of 1.50 cm. The distance between the first tap on the flare and the flare-cylinder junction varied slightly from row to row and was dependent on the fabrication of the flare. Each static pressure tap was 0.0305 cm in diameter and was drilled normal to the surface. Two iron-constantan thermocouples were located within the flare along $\phi = 90°$ and $\phi = -90°$ at $x = 12.5$ cm.

The coordinate system with respect to the model is shown in figure 1. The x–ϕ–r coordinate system is a cylindrical system aligned with respect to the cylinder centerline axis with $x = 0$ cm located at the leading edge of the offset flare. The coordinate y coincided with the r coordinate but was measured from the model surface. The coordinate z was in the transverse direction.

2.3 Oil Flow Visualization

Surface tracer techniques display characteristics of the flow such as the local flow direction and the location of separation and attachment. One such technique involves the placement of a tracing fluid on the model surface prior to each run. During a run, the fluid traces out paths of streamlines close to the surface. The tracing fluid will experience a force due to the shear of the air blowing over it, a force due to the tracing fluid's own viscosity, and a pressure force as a consequence of its finite height when in a region of nonzero pressure gradient. The information obtained from 18 independent test runs devoted to surface oil flows was interpreted and a resulting skin-friction line pattern was developed which describes the surface topology of the interaction.

Over the course of investigating the surface topology, several different liquid mixtures of varying viscosities and constituents were utilized. The tracer method employed during the majority of these runs has been referred to as the the oil-dot method (ref. 10). Vacuum pump oil was mixed with titanium dioxide, a white powdered pigment. A small amount of oleic acid was added to prevent the pigment particles from coagulating. The viscosity of the oil mixture was varied according to a trial and error procedure by altering the amount of titanium dioxide powder. This mixture was dabbed onto the model as small drops in a somewhat organized pattern. Proper distribution of the drops and the amount of oil facilitated the post-run interpretation of the streaks. During the run, the aerodynamic shear of the air causes the drops of oil to spread in the direction of flow. The length of the oil track is dependent upon the shear stress of the air flow. A disadvantage of this particular technique was that on shut-down, the oil was subject to further movement and some details were smeared due to shut-down transients. An additional complication occurred after the run when condensation would, at times, form on the surface due to the relatively cold temperature of the model. The moisture caused a slight smearing of the oil record which affected the quality of the post-run documentation.

4

The procedure to perform an oil-dot test was as follows. The model was first covered with black, adhesive-backed mylar known as MonoKote (Top Flite, Hobbico, Inc., Champaign, Illinois). MonoKote is often used in the construction of model airplanes and is available from hobby shops. Three different pieces of MonoKote were cut to fit on the cylinder, the flare, and the afterbody. The oil was applied to the model and the tunnel was prepared for a run. During a run, which typically lasted five minutes, the oil-streak patterns were video-taped which provided a record of the temporal development of the oil-streak pattern. After the run, the test chamber was brought up to atmospheric pressure by the injection of dry air. The tunnel remained sealed for approximately one hour to allow the model to warm in order to minimize the formation of moisture on the surface. After removal of the tunnel window, the oil-streak patterns were photographed while the MonoKote sections were still on the model. The MonoKote sections were then carefully removed from the model and placed on a flat backing and photographed.

In addition to the vacuum pump oil and titanium dioxide mixture, other types of fluids were used during the tests including mixtures of diesel fuel and kerosene with chalk, and general purpose lubricating oil with chalk. The viscosity of these mixtures was controlled by the percentage of chalk included. For tests involving these tracing mixtures, the model was completely covered with the mixtures prior to the run. During the run, the mixtures would move in the direction of flow. Meanwhile, the kerosene would eventually evaporate leaving behind the chalk. Additional documentation included using a high-speed video system to record two of the runs in which the petroleum mixtures were used.

2.4 Laser Light Sheet

The laser light sheet illumination technique was applied in an attempt to visualize the topology of the flow away from the surface. An existing 15 W argon-ion laser from the HRC-1 LDV system was operated in the single-color mode to produce a violet laser beam of wavelength 0.4765 μm (fig. 3). The laser power was nominally set within the range of 0.1 W to 1.0 W. The laser beam was directed by several mirrors through a cylindrical lens which expanded the beam in one direction forming a sheet of light. A final output mirror directed the light sheet into the tunnel. The plane of the light sheet was perpendicular to the free-stream flow direction. An output lens used in the LDV system to focus the laser beams to a spot size of around 500 μm was used to focus the thickness of the laser light sheet at the model. The laser and associated optics were located on an optical table equipped with stepper motors. The motion control system was operated with software run on a MicroVAX (Digital Equipment Corp., Maynard, Massachusetts) from a terminal inside the control room allowing the light sheet to be scanned to any streamwise location during a run.

Initial attempts at visualizing the flow centered around globally seeding the entire flow with light scattering particles. The atomizing nozzle normally used for the LDV seeding system was employed for this purpose. The nozzle was located in the tunnel stagnation chamber and utilized 600 kPa shop air to assist in atomizing the fluid. The first fluid injected was water. The second fluid injected was a mixture normally used for seeding the flow for LDV measurements and consisted of 0.5 μm latex particles in alcohol and water. The global seeding attempts were not particularly successful.

Emphasis was then shifted to local visualization. This was achieved by introducing different fluids into the flow through pressure taps on the cylinder. The pressure in the tunnel was substantially below

5

atmospheric so that the liquid could be drawn through the tap without any extra back pressure. The pressure tap was connected to plastic tubing which was connected to a metering valve to control the flow rate and then to a reservoir containing the fluid.

The manner in which the flow is seeded is important, as is the method in which the light sheet is viewed and recorded. Having the direction of observation perpendicular to the sheet would avoid distortion due to perspective and would avoid focusing difficulties associated with a camera's depth of field. One drawback is that the intensity of the scattered light is less compared to a viewing angle more on-axis with the projected light sheet. For the present test with optical access consisting of two windows on opposite sides of the tunnel, the range of locations at which the camera could be placed to view the sheet was limited. Most of the still photos and the video were observed from an angle 45° from the light sheet projection. The height of the camera with respect to the model was altered run by run depending on the situation.

A Sony MVC-5000 ProMavica Still Video Camera Recorder was used to document the light sheet images. The camera was triggered by a remote control unit operated from within the tunnel control room. Still images were recorded on a 2 inch still video floppy disk. The recorded images could be seen on a still video player or printed as a hardcopy image. The camera was equipped with a video output which was connected to a monitor inside the control room and recorded by a 0.5 inch video recorder.

2.5 Laser Doppler Velocimetry

The mean and fluctuating velocities of the undisturbed boundary layer were measured with both a two- and three-channel LDV. A schematic of the system is shown in figure 4. The LDV technique measures the instantaneous fluid velocity by detecting the Doppler frequency shift of the laser light. The light is scattered by particles following the flow which pass through the measuring probe volume. The technique requires no calibration other than determining beam angles and is relatively independent of temperature and density. The small measuring volume and fast signal processing electronics allow for high spatial and temporal resolution. The nonintrusive characteristic of LDV is particularly important in supersonic flows and in separated regions.

The three mean orthogonal velocities (U, V, W) along with the ensemble-averages of the fluctuating components can be obtained from the 3-D LDV system measurements. The simplest of the fluctuating terms are mean-squared quantities and second order products, namely $< u'^2 >$, $< v'^2 >$, $< w'^2 >$, $< u'v' >$, $< u'w' >$, and $< v'w' >$. Even though each of these six terms needs to be multiplied by the density to give the units of stress, they are commonly referred to as Reynolds stresses. The first three are apparent normal stresses and the latter three are apparent shear stresses. Each of the Reynolds stresses can be thought of as a mean rate of momentum transfer by the fluctuating motion per unit area.

The mean-velocity profiles are useful to the present study because the local skin friction can be deduced from the profiles using similarity techniques. The law-of-the-wall equation predicts the velocity

6

profile in the logarithmic region as

$$\frac{U}{U_\tau} = \frac{1}{\kappa} \ln \frac{y U_\tau}{\nu} + C \qquad (2\text{-}1)$$

where U_τ is the friction velocity defined as $\sqrt{\frac{\tau}{\rho}}$, κ is the Von Kármán constant, and C is an empirical constant. In order to include the outer regions of the boundary layer, Coles (ref. 11) combined his universal wake function to the law-of-the-wall. This universal correlation was shown to describe adequately most incompressible boundary-layer profiles outside of the viscous sublayer. The incompressible wall-wake profile is given by

$$\frac{U}{U_\tau} = \frac{1}{\kappa} ln \frac{y U_\tau}{\nu} + C + \frac{\Pi}{\kappa} W(\frac{y}{\delta}) \qquad (2\text{-}2)$$

where Π is a wake strength profile parameter. Coles' wake function (W) varies from a value of zero at the surface to a value of two at the boundary-layer edge and can be approximated by the expression

$$W(\frac{y}{\delta}) = 1 - \cos(\pi \frac{y}{\delta}) \qquad (2\text{-}3)$$

An expression based on the boundary-layer edge conditions can be obtained by making the substitutions of $U = U_\infty$ and $y = \delta$ into equation (2-2). Subtracting equation (2-2) as shown above from the expression based on the edge conditions yields a velocity-defect form of the incompressible wall-wake as given by

$$\frac{U_\infty}{U_\tau} - \frac{U}{U_\tau} = -\frac{1}{\kappa} \ln(\frac{y}{\delta}) + \frac{\Pi}{\kappa} [2 - W(\frac{y}{\delta})] \qquad (2\text{-}4)$$

Van Driest (ref. 12) obtained a law-of-the-wall expression for compressible flow by introducing compressibility into the differential equations of continuity, momentum, and energy for turbulent flow. His equation was of the form

$$\frac{U_\infty^*}{U_\tau} - \frac{U^*}{U_\tau} = -\frac{1}{\kappa} \ln(\frac{y}{\delta}) \qquad (2\text{-}5)$$

The generalized velocity, U^*, is given by

$$U^* = U_\infty \frac{1}{A} \arcsin \frac{2A^2 (U/U_\infty) - B}{(B^2 + 4A^2)^{1/2}} \qquad (2\text{-}6)$$

where

$$A^2 = \frac{[(\gamma - 1)/2] M_\infty^2}{T_w/T_\infty} \qquad (2\text{-}7)$$

and

$$B = \frac{1 + [(\gamma - 1)/2] M_\infty^2}{T_w/T_\infty} - 1 \qquad (2\text{-}8)$$

Maise and McDonald (ref. 13) combined Van Driest's compressible law-of-the-wall and Coles' universal wake function to obtain a compressible wall-wake correlation. Their expression was identical to equation (2-4) except that Van Driest's generalized velocity U^* was used instead of the velocity U. Their compressible wall-wake correlation was shown to be in good agreement with existing zero pressure-gradient data.

Matthew, Childs, and Paynter (ref. 14) also developed a compressible wall-wake correlation and verified their expression with data from flows both with and without pressure gradients. However, Sun and Childs (ref. 15) pointed out that Matthew, Childs, and Paynter's expression and equation (2-2) both possess a nonzero velocity gradient at the boundary-layer edge. Consequently, Sun and Childs developed a modified wall-wake profile in which the velocity gradient was equal to zero at the boundary-layer edge. Instead of assuming a constant shear stress when deriving the law-of-the-wall, they assumed the shear-stress distribution within the boundary layer was described by $\tau = \tau_w[1 - (y/\delta)]^a$, where a is some real constant and τ_w is the shear stress at the wall. With this expression and incorporating the effects of compressibility, they derived their modified wall-wake correlation which is given by

$$
\frac{U}{U_\infty} = \frac{(B^2 + 4A^2)^{1/2}}{2A^2} \sin\left[\arcsin\frac{2A^2 - B}{(B^2 + 4A^2)^{1/2}}\left[1 + \frac{1}{\kappa}\frac{U_\tau}{U_\infty^*}\left(\ln(y/\delta) + \frac{2(1 - (y/\delta)^a)^{1/2}}{a}\right.\right.\right.
$$

$$
\left.\left.\left. - \frac{2}{a}\ln(1 + (1 - (y/\delta)^a)^{1/2})\right) - \frac{\Pi}{\kappa}\frac{U_\tau}{U_\infty^*}(2 - W(y/\delta))\right]\right] + \frac{B}{2A^2} \tag{2-9}
$$

With the development of these universal correlations, the friction velocity, and hence the skin friction, could be indirectly determined from the experimental velocity profile. Sun and Childs (ref. 16) published a FORTRAN computer code which could perform a least squares curvefit of their modified wall-wake profile to experimentally measured boundary-layer profile data. Their analysis was used to examine the present LDV mean-velocity data. The value of the wake strength profile parameter was obtained as a consequence of evaluating the correlation at the edge of the boundary layer. By fitting the correlation to the data, the skin friction could be deduced.

2.6 Surface Pressure

Surface pressures were measured through static pressure taps on the cylinder and on the 20° 3-D flare by means of seven pressure sensor modules. Six of the modules were Pressure Systems Inc. (Hampton, Virginia) Series 1600 modules, each of which contained 16 strain gage differential pressure transducers addressed through a 4-bit binary code. The seventh module, from the same manufacturer, contained 32 individual transducers, of which only 16 were used. All pressure transducers were referenced to the upstream static pressure, which, was sensed by a 1000 torr absolute Barocel (Edward High Vacuum International, Wilmington, Massachusetts). The total pressure was sensed by a 100 psi differential Barocel referenced to atmospheric conditions.

Of the 112 individual pressure transducers, one was allocated to measure the upstream static pressure, 67 were allocated to measure the pressure from taps along the cylinder, leaving 44 transducers to measure pressures on the flare. For each run, two of the 13 rows of taps along the flare were connected to the transducers. To increase the resolution of the data along the cylinder where the tap spacing was 0.50 cm, all runs were repeated with the flare relocated 0.25 cm from its reference streamwise position. This represented half the distance between the taps, which doubled the resolution of the measurements on the cylinder. In all, nearly 150 runs were required to document the pressures on the surface of the model.

Prior to every run, the pressure transducers were calibrated. This was accomplished by exposing the transducers through a calibration port to several pressure levels representative of the operating conditions. This calibration pressure was also measured by the static pressure Barocel. The result was a calibration curve for each cell of voltage vs. pressure as measured by the Barocel. A quadratic least-squares curvefit to this calibration data for each individual transducer was then obtained. The pressure acquisition software was written in FORTRAN and was run on a MicroVAX. The pressure acquisition system was similar to that reported by Olsen and Seegmiller (ref. 17), where a detailed pressure accuracy analysis is presented. Based on that analysis, the accuracy of the pressure measurements for the present test is estimated to be within 0.1%.

3 LASER SKIN FRICTION INTERFEROMETRY

3.1 Literature Survey

Tanner and Blows (ref. 18) proposed that the skin friction on a surface could be determined by using photographic interferometry to measure the thickness variation of silicone oil films. The motion of an oil film under the influence of gravity, pressure gradients, and skin friction was analyzed with the first two influences becoming less significant as the oil thins out. Expressions relating the oil-film thickness variation to the skin friction were presented. Six different experiments were carried out to validate the new method. One involved the effect of gravity only, a second involved a rotating plate, and the rest were conducted in a low-speed wind tunnel. These included a flat-plate flow with zero pressure gradient, two flows with pressure gradient (one with and one without separation), and, finally, a 3-D flow. The thickness variation of the oil film over the surface of the glass plates was determined by acquiring interferograms at specified time intervals. These interferograms measured both the oil thickness and the plate thickness, requiring that the latter be subtracted out to obtain the correct oil thickness variation. The first experimental results were consistent with their theoretical predictions.

Tanner and Kulkarni (ref. 19) refer to this method of measuring skin friction as the viscosity balance method, since it is a somewhat direct measurement technique similar to the floating element balance. The technique of using oil droplets in contrast to a continuous oil film was introduced. Favorable comparisons of experimental results with theory further supported the validity of the technique with emphasis on its suitability to 3-D flows. The authors remarked that this new skin-friction measurement technique could provide data in flows which would otherwise be difficult or impossible to document with other methods.

In contrast to photographic documentation of the oil thickness distribution, Tanner (ref. 20) simplified the technique by measuring the temporal variation of the oil thickness at a single point near the upstream edge of the oil film. One of two focused laser beams was used to locate the oil leading edge while the second beam with a known separation from the first was employed as the measurement beam. The reflected light from the air-oil interface was allowed to interfere with the reflected light from the underlying reflective substrate at a photodetector. The output, as documented by a pen recorder, demonstrated a wave-like behavior indicating constructive and destructive interference. The crests of this fringe record were then used to determine the variation of the oil thickness with time. Even though this single-beam method sacrificed the ability to obtain the skin-friction distribution over a wide area of the surface, it could be used on much less restrictive types and shapes of surfaces. The skin-friction measurements using the single-beam approach were consistent with theoretical predictions.

Tanner (ref. 21) made the first comparison of measurements from the viscosity balance technique with measurements from another skin-friction measurement technique. The flow was a two-dimensional (2-D), turbulent boundary layer with zero pressure gradient. The Preston tube was selected for comparison since it was considered to be the most reliable technique available. The results from both methods were in good agreement. Tanner concluded that the viscosity balance method should be accepted as a direct method for the measurement of skin friction in the sense that, under proper conditions, it is independent of the properties of the boundary layer.

10

Monson and Higuchi (ref. 22) improved upon the viscosity balance method by overcoming some of the practical difficulties of Tanner's original procedure. The work was carried out at NASA Ames Research Center. One such difficulty was the inaccuracy introduced in the measurement of the oil-flow time due to tunnel start-up transients. This was alleviated by deriving an effective fringe number and an effective oil-flow time. A second difficulty was the inaccuracy in measuring the distance between the oil leading edge and the measurement beam. This difficulty was avoided by introducing a two-beam instrument in which both beams with a known separation were used to perform measurements. The validity of the system was verified by experimentally measuring the skin friction in a low-speed axisymmetric, turbulent boundary layer and comparing the results to Preston tube measurements. The existence of dust particles was believed to be the largest cause of the scatter in the data. Comparisons were also made to similarity methods using mean velocity data and with computational predictions from a boundary layer code.

Monson, Driver, and Szodruch (ref. 23) applied an LISF instrument to several complex flows including a subsonic rearward-facing step, a 2-D supersonic flow over a flat plate, and to a 3-D supersonic flow over a delta wing at an angle of attack. The rearward-facing step flow demonstrated the value of the LISF technique in making measurements in separated and near-attached regions where other techniques are not reliable. The 2-D supersonic experiment was conducted at two Mach numbers, $M = 2$ and $M = 3$, over a range of Reynolds numbers on a flat plate. This was the first attempt to apply the LISF technique to a supersonic flow. The problem of surface waves at higher shear stresses was encountered, limiting the technique to a maximum shear stress measurement of $120 \ N/m^2$. The supersonic delta wing flow pointed out the importance of measuring the surface temperature. A correction to the oil viscosity as a result of the changing surface temperature was applied assuming a simple, linear temperature distribution. A theoretical analysis was introduced for the application of the LISF instrument to 3-D flows.

Monson (ref. 24) extended the LISF technique to the measurement of skin friction in 3-D flows of unknown direction. A shear-driven flow was created when a low-speed, swirling boundary layer produced on a rotating cylinder encountered a stationary section and began turning back toward the free-stream direction. Both the axial and transverse components of skin friction were measured from which the skin-friction magnitude and direction were resolved. The skin-friction results were in good agreement with the results from a bi-directional surface-fence gauge.

Westphal, Bachalo, and Houser (ref. 25) developed a two-beam LISF system to perform measurements in a 2-D incompressible boundary layer. One of their two main objectives was to maximize the signal visibility. A second objective was to automate the data acquisition and reduction procedures. The computerized data reduction routines helped alleviate the subjectivity of the identification of bad records. The system was applied to a boundary layer free of pressure and shear gradients. The minimum number of fringes included in the data reduction was 20.

Settles (ref. 26) surveyed recent developments on the various techniques to measure skin friction. Included in his survey was a progress report and description of the LISF instrument developed at Pennsylvania State University to be used in supersonic flows. A more comprehensive description of this LISF instrument and its application in compressible flows was presented by Kim (ref. 27). The instrument was first verified in a low-speed flow and then in a supersonic flow on a polished stainless steel flat plate (see also ref. 28). The supersonic calibration experiment was carried out at three different

Mach numbers (M = 2.45, 2.98, and 3.51) utilizing several oils of differing viscosities. The LISF results, with a reported repeatability of ±4%, were compared to estimates from the Van Driest II theory and a wall-wake law curvefit of measured boundary-layer profiles. A new data reduction procedure was presented that differed slightly from previous studies which involved incompressible flows. This reduction procedure stemmed from the limited number of fringes available in high shear-stress flows. This work set the stage to perform measurements in a swept SW/BLI.

Kim (ref. 27) demonstrated the usefulness of the LISF technique in a complex flow by performing measurements in a 3-D swept SW/BLI generated by a fin located on a flat plate. Two sets of data, with fin angles of 10° and 16°, were collected in a nominally M = 3 flow. Taking advantage of the quasi-conical similarity of the flow, only one arc of data through the interaction was acquired to document the flow. The single-beam method was employed. To perform measurements in the 3-D flow, the flow direction was first determined by an oil-flow visualization technique. The oil leading edge was then applied perpendicular to this direction as was the single measurement beam. The high shear stress flow led to surface waves in the oil film, limited tunnel run time, and forced the data reduction to be done on as few as two interference fringes. The maximum level of shear stress as measured by an LISF instrument was extended to 600 N/m^2. The pressure and shear gradients present in the complex flow were found to have a negligible effect on the LISF measurements since the oil film was thin. In contrast, these same effects can cause other techniques to be unreliable in complex flows. Comparison of the LISF data in the SW/BLI was made with two different computations.

Kim et al. (ref. 29) further extended the LISF technique to measure shear stress levels of 1000 N/m^2. Measurements were made in an M = 4 interaction with a sharp unswept fin at two angles of attack, 16° and 20°. The two data sets from the M = 3 experiment of Kim (ref. 27) were also summarized. As before, measurements in the 3-D flow were accomplished by first determining the surface streamline directions by kerosene-lampblack surface flow visualization. A slight peak in the skin-friction distribution was observed between the upstream influence and the primary separation line for the weakest interaction. A peak in the distribution was also observed near the secondary separation line. For all four cases, the maximum skin-friction value near reattachment increased with increasing interaction strength. For the M = 4, 16° case, the peak skin-friction value was almost an order of magnitude higher than the upstream value. Results were compared to Navier–Stokes computations which utilized four different turbulence models. The computations significantly underpredicted the peak skin-friction levels as compared to the LISF measurements. The cause for the discrepancies was attributed to the turbulence models and not to the grid resolution. The results using the simpler algebraic turbulence models were in better agreement with the data than the more complex $k - \epsilon$ models.

Seto and Hornung (ref. 30) at the California Institute of Technology introduced a new variation of the technique to measure the thickness of the oil film. Instead of measuring the variation of the oil film at a particular point, the spatial variation of the oil-film thickness within a spot was measured by capturing images with a linear charge coupled device (CCD) array at successive intervals. The particular instrument constructed allowed measurements to be performed from within the model. A fiber optic cable transmitted the laser light to the model which, for their case, was a flat plate. After collimation, the diameter of the beam was 4 mm. The beam passed through a beamsplitter which redirected part of the incident beam toward one surface of the beamsplitter which also served as a part of the model surface. The measurements were performed on that surface. Oil was released through a porous material located within the wall upstream of the beamsplitter. From the spatial record of the interference pattern,

12

the slope of the oil film was determined which was used to calculate the shear stress. Measurements were performed in a turbulent flat-plate flow at low speeds subject to various flow conditions. For a zero pressure-gradient flow, the measurements from the new technique compared favorably with measurements performed with a floating-element balance. The technique was also applied to flows with different imposed pressure gradients. For these cases, the measurements with the new technique had to be performed near the leading edge after the oil had thinned significantly so that the effect of the pressure gradient on the shape of the oil film was negligible.

Seto and Hornung (ref. 31) further refined their instrument. The fringe pattern within a 1 mm beam spot was recorded at 20 discrete times during each run. Comparisons made with measurements from floating-element balances for a zero pressure case were in agreement. The new oil-film skin-friction meter was capable of measuring both the magnitude and the direction of the skin friction. The authors emphasized the possible application of the technique to acquiring measurements on a vehicle in flight.

Bandyopadhyay and Weinstein (ref. 32) developed a reflection-type oil-film skin-friction meter. Instead of interferometrically measuring the thickness of the oil, from which the oil-film slope can be deduced, the oil-film slope was measured directly. This was accomplished by utilizing a position sensing photodiode to track the location of a laser beam that had reflected from the oil film. The technique was applied to both the low-speed flow in a pipe and on a flat plate. The data scatter was originally very large prompting some changes in the data reduction method. The advantages of such a technique are that it does not rely on interferometry and does not require a special surface to perform measurements on. The technique, however, may be susceptible to errors due to vibration and model movement.

The LISF technique was applied to an SW/BLI at Mach 8.2 as reported by Knight, Horstman, and Monson (ref. 33). The interaction was generated by a sharp fin on a flat plate. Two cases were examined with fin angles of 10° and 15°. Originally, the data were reduced based on a dual-beam approach in which the data from the beams from two different runs were combined to correct for beam movement during the run. The data were reanalyzed using the single-beam approach and the effect of beam movement was found to be small. This is the highest speed flow in which the LISF technique has been used to acquire data.

Typically, the duration of tunnel runs is long enough so that the LISF technique can acquire data. In other words, there is enough time for a sufficient number of fringes to pass through the stationary measurement location. However, for some supersonic and hypersonic facilities, the run time is limited. Hubner and Carroll (ref. 34) made a comparison of two oil-film skin-friction techniques in a short duration supersonic tunnel. One method acquired data using the dual-beam approach which documents the time-fringe pattern. A second method acquired data using the expanded laser beam approach which documented the spatial fringe pattern by a CCD array. This technique captures the oil-film slope on each image. For the run times of less than five seconds, the expanded laser beam approach possessed lower uncertainties than the dual-beam approach since the time envelope to acquire sufficient data is shorter for the former. For longer run times, the uncertainties associated with both methods were comparable. The skin-friction results from both techniques agreed with Preston probe measurements.

Monson, Mateer, and Menter (ref. 35) introduced the fringe-imaging skin friction (FISF) technique. The method was an improvement upon the earlier photographic technique of Tanner and Blows (ref. 18). Unlike the latter, the new technique did not require a glass plate as a test surface. A line of oil was

placed on a 2-D wing model covered with a clear plastic. The subsonic flow sheared the oil. After the run, the oil film was illuminated with monochromatic light and the resulting interference fringe pattern was recorded with a CCD camera. The images were digitized and analyzed. The fringe patterns were useful in indicating the location of transition. Provided that a reference value of skin friction was known at some location on the model, then the the images could be reduced to yield a global distribution of the skin friction. In contrast, single-beam LISF is a point measurement technique which would require numerous tunnel runs to acquire the data captured in just one run using the FISF method.

Since Tanner and Blows first introduced the theoretical basis for the oil-film skin-friction technique, there have been many different approaches to implementing the theory. The oil-film skin-friction technique is nonintrusive and is quasi-direct in determining the shear stress at the wall. The technique does not require calibration. The cost of the oil-film skin-friction instrument is relatively low. Since its inception, the technique has been applied to flows of increasing complexity. It is in these complex flows, such as SW/BLI, that the real advantage of the oil-film skin-friction technique comes to light because it is capable of performing accurate skin-friction measurements in flows with large pressure and shear gradients.

3.2 Theoretical Background

Detailed derivations of the fundamental equations of the LISF technique are given by Tanner and Blows (ref. 18), Monson (ref. 36), and Kim (ref. 27). Consequently, a detailed derivation of those same equations is not included here. Instead, only a brief description of the pertinent LISF equations will be given. This will be followed by a more in-depth presentation of the data reduction theory used in the present study.

3.2.1 Basic Theory

Briefly, the LISF technique requires a thin film of transparent oil on the test surface. This oil is drawn out into a continuous film by the shearing stress of the air flow (fig. 5). To measure the time-dependent thickness of this oil film, a focused laser beam is directed toward the oil. A portion of the laser beam is reflected from the air-oil interface and another portion is reflected from the oil-model interface. The light reflected from the two interfaces is imaged onto a photocell using collecting lenses. The path length of the light reflected from these two interfaces from the laser to the photocell differs according to the oil-film thickness. As the oil film thins, a time sequence of interference fringes occurs at the photocell due to the varying path length difference. The time-varying voltage output of the photocell is referred to as the fringe record and consists of a series of peaks and valleys related to the time-varying oil thickness.

An oil film subjected to a constant shear stress will assume a wedge shape. The basic LISF equation (ref. 18) for the shear stress at the wall is

$$\tau = \frac{\rho_o \nu_o x}{yt} \qquad (3\text{-}1)$$

14

where τ is the local shear stress at the wall, ρ_o is the oil density, ν_o is the oil kinematic viscosity, x is the distance between the measurement beam and the oil leading edge, y is the local oil thickness, and t is the oil flow time. This equation is valid for flows free of pressure gradient effects, shear gradient effects, and gravity effects. Under these conditions the equation determining the shear stress at the wall is independent of the properties of the boundary layer. Typically, the distance between the measurement beam and the oil leading edge is held constant during a run. Assuming a steady oil temperature leads to a constant value for the oil density and viscosity. Consequently, the numerator in equation (3-1) is constant. This condition, together with the assumption of a flow with a steady shear stress over time, implies that the product of the oil thickness and the time (yt) must also be a constant. A value for this product can be obtained from the LISF instrument.

An expression for the thickness of the oil film in terms of measurable optical quantities can be derived with the assistance of thin-film theory. Assume an incident laser beam initially in air encounters a thin film of oil on some substrate (fig. 6). The refractive indices of the air, oil, and the substrate are designated by n_{air}, n_o, and n_s, respectively. The incident beam of light at some angle θ_i will partially reflect off the air-oil interface at point A. The rest of the beam will be refracted at some angle θ_t. The refracted beam then reflects off the underlying oil-substrate interface at point B and exits the oil at point C. Since the two beams have traveled different distances, a relative phase difference exists between them.

From figure 6, the optical path length difference (Δ_p) between the two beams is

$$\Delta_p = n_o(AB + BC) - n_{air}(AD) \tag{3-2}$$

From geometric considerations, the optical path length difference can be expressed in terms of the oil thickness and the internal angle of the refracted beam as

$$\Delta_p = 2yn_o \cos \theta_t \tag{3-3}$$

The term $\cos \theta_t$ can be related to the incident beam angle, θ_i, by

$$\cos \theta_t = \cos\left(\arcsin\left(\frac{1}{n_o}\sin\theta_i\right)\right) \tag{3-4}$$

An additional path length difference can arise as a result of phase changes which can occur at reflection. For the present case, however, both reflections are external ($n_{air} < n_o < n_s$) so that the relative phase difference between the two beams due to reflection is zero.

When the two reflected beams are combined, constructive interference occurs when the path length difference is some integer multiple of the light wavelength

$$\Delta_p = N\lambda \tag{3-5}$$

where N is the fringe number and λ is the wavelength of the light beam. Combining equations (3-3) and (3-5) leads to an expression for the thickness of the oil film

$$y = \frac{N\lambda}{2n_o \cos \theta_t} \tag{3-6}$$

15

Upon substitution of the oil thickness from equation (3-6) into equation (3-1), the expression for the wall shear stress becomes

$$\tau = \frac{2n_o x \rho_o \nu_o \cos\theta_t}{N\lambda t} \tag{3-7}$$

3.2.2 Three-Dimensional Measurements

Skin-friction measurements in 3-D flows can be obtained in several different ways by the LISF technique. If the local flow direction is known, then the measurement direction of the LISF technique can be aligned with the flow direction in order to determine the magnitude of the skin friction. (Note that the measurement direction of the LISF will be normal to the leading edge of the oil film.) If the flow direction is not known, then two LISF measurements are required in orthogonal directions. From these two measurements, the magnitude and direction of the resultant skin friction can be resolved. For the present experiment, the flow direction was known from the surface oil-flow documentation. However, two orthogonal measurements were performed anyway at selected locations within highly 3-D regions. The resolved flow direction from these skin-friction measurements could then be checked against the flow direction results from the oil-flow visualization technique.

3.2.3 Incremental-Peak Method

The main quantity to be determined from the LISF fringe record is the product of the fringe number and time (Nt). The following analysis was suggested by Bouslog (ref. 37) in order to accurately determine a value for the fringe-time product from LISF data. His method will be referred to here as the "incremental-peak method." Equation (3-7) can be rearranged to obtain

$$1/N = \frac{\tau\lambda}{2n_o x \rho_o \nu_o \cos\theta_t} t \tag{3-8}$$

Continuing with the assumptions of steady wall shear stress and oil temperature, a constant C_1 can be assigned to be

$$C_1 \equiv \frac{\tau\lambda}{2n_o x \rho_o \nu_o \cos\theta_t} \tag{3-9}$$

so that equation (3-8) now reads

$$1/N = C_1 t \tag{3-10}$$

Examining a portion of a fringe record such as is shown in figure 7, a reference fringe peak can be arbitrarily selected. A fringe number (N_o) and the time (t_o) can be assigned to that peak even though the actual values are unknown. Inserting these variables into the previous equation yields

$$1/N_o = C_1 t_o \tag{3-11}$$

Proceeding through the rest of the fringe record, each successive peak is assigned an integer (k_i) which is incremented by one for each peak. If both the peaks and valleys are included in the analysis, then each extreme would increase the variable (k_i) by $\frac{1}{2}$. Thus, some extreme occurring in time after the reference fringe may be identified by its fringe number and time as given by

$$N = N_o - k_i \tag{3-12}$$

16

$$t = t_o + t_i \tag{3-13}$$

where t_i represents the incremental time. Thus, as t increases, N must decrease since the two are in a reciprocal relationship with each other. These two expressions can be inserted into equation (3-10) to obtain

$$\frac{1}{N_o - k_i} = C_1(t_o + t_i) = C_1 t_o + C_1 t_i \tag{3-14}$$

Recalling that $C_1 = 1/N_o t_o$ and introducing two new constants, the previous equation can be rearranged to read

$$\frac{1}{k_i} = \frac{t_o}{t_i N_o} + \frac{1}{N_o} = \frac{C_2}{t_i} + C_3 \tag{3-15}$$

where the constants are defined as

$$C_2 \equiv t_o/N_o \tag{3-16}$$

$$C_3 \equiv 1/N_o \tag{3-17}$$

The incremental values for the fringe number and time, k_i and t_i, in equation (3-15) are obtained from the LISF fringe record once a reference fringe is chosen and can be plotted as shown in figure 8. Due to the selection of the coordinate axes, the data point for the reference fringe is located at the origin of the plot. The time at which the flow began does not need to be known for this analysis. Equation (3-15) contains two unknown constants C_2 and C_3 which can be determined as follows. Rearranging equation (3-15) into the form

$$k_i = \frac{t_i}{C_2 + C_3 t_i} \tag{3-18}$$

one can perform, by iteration (ref. 38), a least squares curvefit to the incremental fringe number versus time data as shown in figure 8 according to the above equation. The curvefit yields values to the constants C_2 and C_3. These two constants can be combined to determine the constant C_1 by

$$C_1 = C_3{}^2/C_2 \tag{3-19}$$

And finally, by rearranging equation (3-9), the local shear stress at the wall can be calculated from

$$\tau = \frac{2n_o \rho_o \nu_o x \cos\theta_t \ C_1}{\lambda} \tag{3-20}$$

To recapitulate, once a fringe record is experimentally obtained with the LISF instrument, a reference fringe is chosen. The incremental fringe number and time of each extreme is determined and plotted. The data are analyzed by performing a curvefit of the data using equation (3-18). The curvefit yields the values for the constants which together can yield the value for the fringe-time product. Knowing the properties of the oil and the characteristics of the LISF instrument, the local shear stress at the wall can be computed using equation (3-20).

3.2.4 Wall Temperature Correction

In the preceding derivation, the temperature of the oil was assumed to be constant but this may not always be valid. Since the temperature of the test surface may be changing during a tunnel run, this

17

will directly affect the oil temperature. If the oil temperature changes with time, then the oil properties are also changing so that each extreme in the fringe record occurred at a time when the viscosity of the oil was different. It is desirable to normalize the fringe data with some reference oil temperature and oil viscosity. The provision for a changing oil temperature with time is included in the data reduction as follows. Returning to equation (3-1), there are two oil properties, ρ_o and ν_o, which are dependent upon the oil temperature and, hence, are dependent on the time as a result of the temporal variation of temperature. Rewriting equation (3-8) and indicating which terms are dependent upon the changing oil temperature leads to

$$\frac{1}{N} = \frac{\tau\lambda}{2n_o x \cos\theta_t} \frac{t}{\rho_o(t)\nu_o(t)} \tag{3-21}$$

The oil temperature is assumed to equal the temperature of the test surface. For the present supersonic case, the surface temperature distribution could be curvefit with the second-order polynomial

$$T_s(t) = a_1 + a_2 t + a_3 t^2 \tag{3-22}$$

where $T_s(t)$ is time dependent temperature of the surface. The density and viscosity of the oil can be expressed as being exponentially dependent upon temperature by the expressions

$$\nu_o(t) = \nu_r e^{-s\left(T_s(t) - T_r\right)} = \nu_r e^{-s(a_1 + a_2 t + a_3 t^2 - T_r)} \tag{3-23}$$

$$\rho_o(t) = \rho_r e^{-\alpha\left(T_s(t) - T_r\right)} = \rho_r e^{-\alpha(a_1 + a_2 t + a_3 t^2 - T_r)} \tag{3-24}$$

where ν_r and ρ_r are known reference values determined at a reference temperature T_r. The constant s for the viscosity expression is the viscosity-temperature coefficient of the oil. The constant α for the density expression is the coefficient of expansion of the oil. The temperature has a much more significant effect on the kinematic viscosity than on the density.

The differential form of equation (3-21) can be integrated from some reference fringe N_o at time t_o to some other fringe $N_o - k_i$ at later time $t_o + t_i$.

$$\int_{\frac{1}{N_o}}^{\frac{1}{N_o - k_i}} d\left(\frac{1}{N}\right) = \frac{\tau\lambda}{2n_o x \cos\theta_t} \int_{t_o}^{t_o + t_i} \frac{dt}{\rho_o(t)\nu_o(t)} \tag{3-25}$$

Substituting the temperature dependent expressions for the oil density and viscosity, the right hand side integral reads

$$\int_{t_o}^{t_o + t_i} \frac{dt}{\rho_o(t)\nu_o(t)} = \frac{1}{\rho_r \nu_r} \int_{t_o}^{t_o + t_i} e^{\left((\alpha+s)(a_1 + a_2 t + a_3 t^2 - T_r)\right)} dt \tag{3-26}$$

The value of this integral is defined as the temperature corrected time t_c

$$t_c = \int_{t_o}^{t_o + t_i} e^{\left((\alpha+s)(a_1 + a_2 t + a_3 t^2 - T_r)\right)} dt \tag{3-27}$$

18

The following approximation can be used for the exponential term inside the integral

$$e^x \approx e^a \left(1 + (x - a) + \frac{(x - a)^2}{2!} + \ldots \right)$$ (3-28)

thus,

$$e^{A(a_1 + a_2 t + a_3 t^2 - T_r)} \approx e^{A(a_1 - T_r)} \left[1 + Aa_2 t + A(a_3 + \frac{1}{2}Aa_2^2)t^2 + \right.$$

$$\left. A^2(a_2 a_3 + \frac{1}{6}Aa_2^3)t^3 + \frac{1}{2}A^2(a_3^2 + Aa_2^2 a_3)t^4 \right]$$ (3-29)

with the higher order terms neglected and $A \equiv \alpha + s$. Using equation (3-29), equation (3-27) can be integrated to yield the corrected time

$$t_c = e^{A(a_1 - T_r)} \left[(t_f - t_o) + \frac{1}{2}Aa_2(t_f^2 - t_o^2) + \frac{1}{3}A(a_3 + \frac{1}{2}Aa_2^2)(t_f^3 - t_o^3) \right.$$

$$\left. + \frac{1}{4}A^2(a_2 a_3 + \frac{1}{6}Aa_2^3)(t_f^4 - t_o^4) + \frac{1}{10}A^2(a_3^2 + Aa_2^2 a_3)(t_f^5 - t_o^5) \right]$$ (3-30)

where the simplification of $t_f \equiv t_o + t_i$ has been made.

Thus, to account for the temporal variation of the oil temperature, a reference condition is selected and the corrected time is computed according to equation (3-30). This corrected time is then used in equation (3-14), and in the solution process as outlined by equation (3-14) through equation (3-20).

3.2.5 Pressure-Gradient and Gravity Correction

Up to this point, the analysis has not taken into account the effect that gravity or a nonzero pressure gradient may have on the oil film. Since the oil film is very thin, these effects are usually small and thus can be accounted for by applying a correction to the measured value of the shear stress at the wall. Following Tanner and Blows (ref. 18) and Monson, Driver, and Szodruch (ref. 23), the corrected shear stress is computed by

$$\tau_c = \frac{\tau}{1 - \epsilon}$$ (3-31)

where τ_c is the corrected shear stress. The correction parameter, ϵ, is determined from the equation

$$\epsilon = \frac{\overline{N'}\lambda}{2n_o \tau \cos \theta_t} \left[\frac{\partial P}{\partial x} - (\rho_o g \sin \theta)_x \right]$$ (3-32)

where θ is the test surface inclination with respect to the horizontal. The term $\overline{N'}$ is an average value of the effective fringe number during the time interval of analysis and is simply a measure of the average thickness of the oil.

$$\overline{N'} = N' + \frac{\Delta N_{i-f}}{2}$$ (3-33)

The use of an effective fringe number instead of the actual fringe number arises as a consequence of the difficulty in determining the actual oil-flow time due to start-up transients of the wind tunnel.

19

The derivation of the effective equations is as follows. If a small degree of roughness is assumed to be present on the surface, then a thin layer of oil adjacent to the surface will be stationary. This thickness is designated as δ_{oil} and the leading edge slope for the oil as α_{oil}. By rearranging equation (3-1) to obtain

$$x = \frac{\tau y t}{\rho_o \nu_o} \tag{3-34}$$

the effects of the stationary oil and the leading edge slope can be incorporated so that

$$x = \frac{\tau (y - \delta_{oil}) t}{\rho_o \nu_o} + \frac{(y - \delta_{oil})}{\alpha_{oil}} \tag{3-35}$$

Upon the substitution of equation (3-6) for the oil thickness, the above equation can be reduced to read

$$x = \left(\frac{\tau \lambda}{2 n_o \rho_o \nu_o \cos \theta_t} \right) N' t' \tag{3-36}$$

where N' and t' are the effective fringe number and the effective oil flow time respectively which are given by

$$N' = N - \frac{2 n \delta_{oil} \cos \theta_t}{\lambda} \tag{3-37}$$

$$t' = t + \frac{\rho_o \nu_o}{\alpha_{oil} \tau} \tag{3-38}$$

The effective fringe number is not an integer and differs from the actual value of the fringe number by a constant so incremental changes in both will be equal. By recalling that under proper conditions the product of the time and oil thickness is a constant, the following expression can be obtained

$$N' t' = (N' + \Delta N_1)(t' + \Delta t_1) = (N' + \Delta N_2)(t' + \Delta t_2) \tag{3-39}$$

The meaning of this equation is that the product of the effective fringe and time $(N' t')$ for a particular extreme is equal to the fringe-time product of another extreme as represented by an incremental change in fringe number, ΔN_1, and time, Δt_1. Likewise, the products are equal to a third product from another extreme represented by the incremental changes ΔN_2 and Δt_2. Solving equation (3-39), the effective fringe number and time of the extreme of interest can be determined by

$$N' = \frac{\Delta N_2 (1 - \Delta t_2 / \Delta t_1)}{(\Delta N_2 / \Delta N_1 - \Delta t_2 / \Delta t_1)} \tag{3-40}$$

$$t' = -\Delta t_1 \left(\frac{N'}{\Delta N_1} + 1 \right) \tag{3-41}$$

Thus, the effective values of any extreme can be determined from the information about any other two extremes. Some LISF data reduction techniques utilize these effective values instead of the actual fringe number and oil flow time.

20

3.3 Apparatus

3.3.1 Hardware

Some of the components of the LISF apparatus used by Monson, Driver, and Szodruch (ref. 23) were used in the present apparatus. Some characteristics of the LISF system are listed in table 3 and a schematic is shown in figure 9. For discussion purposes, the LISF apparatus can be divided into a transmitting side and a receiving side. The transmitting side of the instrument included a 5.0 mW helium–neon laser that produced a coherent light beam at a wavelength of 0.6328 μm. A spatial filter and a combination of lenses expanded the beam and allowed adjustment of the beam focus location. A 6.330 mm thick interferometric flat made of fused silica was used to split the beam. By positioning the flat at a 45° angle with respect to the incident beam, the reflection from the front and the back of the flat provided two beams of nearly the same intensity with a spacing of 5 mm. The intensity of each beam was nominally 0.1 mW. A vertical assembly containing several mirrors directed the two laser beams into the tunnel and toward the model. The laser and all of the transmitting optics were rigidly secured to an optical table.

The receiving side included a lens to collimate the reflected light from the model. A second lens focused the collimated light from the two measurement spots onto different sides of a reflective-coated prism. The prism directed the beams into two separate photodiodes operated in the photovoltaic mode. The signal from each photodiode was amplified by battery powered amplifiers and then passed through a 30 Hz low-pass filter. Typical signal levels at the analog-to-digital board were one volt. The receiving optics were located on the same optical table as the transmitting optics.

The optical table was secured to the main HRC-1 optical table located on the opposite side of the tunnel by a cantilevered structure underneath the tunnel. Motion of the entire carriage system, including both the main and the cantilevered optical tables, was controlled in the vertical and streamwise directions by two stepper motors.

3.3.2 Single-Beam Technique

Although two beams with a known spacing were available, the single-beam approach was used to perform the skin-friction measurements. The dual-beam approach typically has the advantage of not requiring a measurement of the distance between the leading edge and the laser beam. Another approach is to use one of the two beams to locate the oil leading edge and to use the second beam to perform measurements. But the present motion control system provided a way to quickly and accurately position the beams anywhere in the tunnel, thus simplifying the task of finding the leading edge with one of the beams and then relocating that same beam to the desired measurement location.

Another reason for selecting the single-beam approach had to do with the size of the flow field interaction. Some distinct regions of the flow field were small, posing problems in making measurements with the dual-beam method with a nominal 5 mm spacing. A second interferometric flat of thickness 3.165 mm was available to replace the thicker interferometric flat which would reduce the beam spacing to 2.5 mm. But even with this spacing it was still difficult to perform measurements in some regions of interest. Although the single-beam approach was used to make the primary measurements, the signal from the second beam was also recorded when possible. Both signals from a typical run are shown in

21

figure 10. The signal from this downstream beam was adversely affected by surface waves for a longer amount of time. When the results from the downstream beams are reported, they are clearly described as such.

3.3.3 Beam Orientation

The original intent of the study was to perform all measurements in the plane on top of the cylinder. In light of this, coupled with the optical access consisting of two windows on either side of the tunnel, the glancing-angle approach for the incident beam was initially attempted. The transmitting hardware was originally installed on one side of the tunnel and the receiving hardware was installed on the opposite side. The measurement beams were aligned to reflect off the top surface. It was quickly discovered that the location of the reflected beams at the receiving optics moved once the tunnel was evacuated just prior to the tunnel run. This indicated that the cylinder and/or tunnel was moving slightly with respect to the laser beams. Due to the glancing-angle approach and the radius of the cylinder, any slight movement of the model would result in a much larger re-direction of the reflected laser beams. The movement appeared to occur with a change in the test-section pressure, but the model did not appear to fluctuate during a run.

Due to this slight movement of the model during tunnel evacuation, the setup of the instrument was changed so that the measurement beams approached the model at near-normal incidence angles. This method was much less sensitive to model movement than the glancing angle approach. In addition, the near-normal approach is advantageous over the glancing-angle approach which causes the impinging measurement beam spots to be elongated increasing the size of the beam spot. Such an increase in the diameter of the beam spot can decrease the visibility of the signal. Due to the side optical access to the tunnel, both the receiving and transmitting hardware were located on the same side of the tunnel and the flare was rotated so that the azimuth to be measured was aligned with the side of the cylinder. All skin-friction results reported were acquired with the flare rotated in that position.

3.3.4 Surface Preparation

The properties of the surface upon which the oil flows and from which a portion of the laser beam reflects are important. First, the surface must be smooth and free of imperfections (such as scratches). Second, it is desirable that the intensity of the reflected beam from the oil-surface interface be comparable to the intensity of the reflected beam from the air-oil interface in order to maximize visibility. The most logical starting place in surface preparation was the polishing of the stainless steel cylinder. A small region on the cylinder upstream of the interaction was polished to perform some preliminary LISF measurements. Achieving a good polish on the cylinder was complicated by the fact that the cylinder could not be removed from the tunnel without running the risk of altering the flow field after re-installation. In contrast to the cylinder, the flare was manufactured from aluminum and epoxy. The portion of the flare that was composed of epoxy could not be polished. Although the aluminum could have been polished, it was not attempted since aluminum does not typically maintain a good polish.

An alternative to polishing the test surface was sought. First, a layer of white or black MonoKote was applied to the surface. Then a clear plastic (ref. 35) with an adhesive backing was placed over the MonoKote. The clear plastic provided a smooth surface where the oil could flow and also reflected

22

a portion of the incident beam that was comparable to the intensity of the reflection from the air-oil interface (fig. 11). Note, the beams which reflect from the oil-plastic interface and the plastic-Monokote interface have a fixed relative phase during any particular run. The Monokote covered the model surface and absorbed the portion of the incident beam that passed through both the oil and the clear plastic. The Monokote and clear plastic also served the viable task of covering over the static pressure taps on the cylinder guarding against any interference from the taps on the LISF measurements. A second technique of preparing the surface was to spray paint the surface black and then attach the clear plastic. As before, the clear plastic reflected a portion of the incident beam, whereas the blackened surface served to minimize extra specular reflections.

3.3.5 Oil Properties and Application Methods

The oils used in this test were Dow Corning 200 Silicone Fluids with three different nominal viscosities: 200, 500, and 1000 cs. Some properties of these oils are summarized in table 4. These oils are suited for use in LISF measurements because they are clear and free of any suspended matter. The oils possess a low surface tension and a low vapor pressure relative to tunnel operating conditions. Kim (ref. 27) estimated that the evaporation of the oil is negligible for a supersonic test under conditions similar to the present test. Since the viscosity must be accurately known over the range of temperatures for the test, the oils used in this study were examined by an independent laboratory (Gascogne Laboratories Inc., Baltimore, MD), which used a glass capillary kinematic viscometer to measure the viscosity of each oil at certain temperatures. The dependence of viscosity upon temperature was found to be best described by equation (3-23). A value for the viscosity-temperature coefficient for each oil was determined by performing a curvefit of the previous equation to the viscosity data. The data and the curvefit for the three oils used in the test are shown in figure 12.

The LISF measurements were performed on the side of the model which, in fact, facilitated the application of the oil prior to the test run. A small amount of oil was applied to the surface using an eye dropper. The oil was placed on the model at a position vertically higher than the measurement beam location and the oil was allowed to flow downward. In this way, the leading edge of the oil was assured to be perpendicular to the streamwise measurement direction. Depending on the beam location, the excess oil was then carefully wiped off. After the tunnel was sealed, but before the tunnel run, the pressure in the test section was equalized to the vacuum sphere pressure. The main valve between the test section and the vacuum sphere was opened as quickly as possible resulting in a brief burst of airflow. The shear from this airflow thinned the oil without changing the location of the leading edge which was the upstream edge of the oil film.

A slightly different oil application technique was required when performing measurements within the separated region along $\phi = 180°$ where the flow direction was pointed upstream. A small amount of oil was placed vertically higher and downstream of the measurement beam location. As before, the oil was allowed to flow under the influence of gravity and the excess oil was wiped from the surface. The pressure inside the test section was equalized to the pressure inside the vacuum sphere slowly through a small diameter bypass valve. In contrast to using the main valve, this technique minimized the amount of pre-run airflow in the test section and, hence, protected the oil on the model from moving downstream and affecting the oil leading edge which, for this case, was the downstream edge of the oil film. In order to perform transverse measurements, the oil leading edge was required to be perpendicular to the transverse direction. For this case, the oil was applied by using a thin straightedge.

3.4 Data Acquisition

The data collected during a typical LISF tunnel run included not only the two signals from the photodetectors, but also the signals from five different thermocouples and two pressure transducers. These nine analog signals were digitized through a DEC ADQ32 analog-to-digital board. The data were acquired and stored on a DEC MicroVAX computer using software written in FORTRAN. The acquisition software displayed realtime plots of the amplified signals from both photodetectors.

3.4.1 Pressure Measurement

One of the two pressure signals provided an indication of the static pressure in the test section as sensed by a 1000 torr absolute Barocel. The second pressure signal was an indication of the total pressure as sensed by a 100 psi differential Barocel. The total pressure measurement revealed some minor tunnel operating difficulties during the early stages of a run. Due to the hardware associated with controlling the wind tunnel, there was often a significant length of time required for the tunnel to reach stable operating conditions. The delay was typically between 10 and 60 seconds and limited the time interval which could be considered valid for analysis of the fringe record.

3.4.2 Total Temperature Measurement

The two types of thermocouples used during the experiment were iron-constantan (Type J) and chromel-constantan (Type E). The thermocouples were hooked into a junction box, operated at a reference temperature of 473 K, capable of handling several types of thermocouples. The initial total temperature of the flow, which was dependent upon the temperature of the storage tanks, varied from run to run. The temperature of the storage tank was affected by the ambient temperature and the recent history of the tank (i.e., recent expansions). A typical total temperature distribution during a run is shown in figure 13 and was seen to decrease approximately 10 K during the run. The spike in the total temperature distribution at the beginning of the run was the result of start-up transients. During the checkout phase, three different (Type J) thermocouples located within the tunnel stagnation chamber were used to measure the total temperature. The readings from all three thermocouples were within 1% of each other. One thermocouple was subsequently chosen to measure the total temperature throughout the duration of the LISF test runs.

3.4.3 Surface Temperature Measurement

An accurate measure of the surface temperature is important for the accurate determination of skin friction with the LISF technique since the oil viscosity is sensitive to the surface temperature. This point is illustrated for the 500 cs oil at a surface temperature of 270 K. A 1 K change in temperature changes the viscosity of the oil and hence the computed shear stress by 2%. Since the oil is extremely thin, the temperature of the oil is assumed to be equal to the temperature of the surface. Kim (ref. 27) validated this assumption analytically for conditions similar to the present case. The steps taken to measure this surface temperature are forthcoming and are discussed in some detail to build up a background of experience so that measurements can be made with greater accuracy in the future.

Although thermocouples are often used in measuring surface temperatures, difficulties in attaching these thermocouples cast doubt that the indicated temperature is the actual surface temperature. In

most cases, the mere presence of a thermocouple or any other alternative transducer will alter the actual temperature distribution near the vicinity of the attachment (ref. 39). Thus, the indicated temperature will be a measure of the perturbed temperature. A major difficulty lies in the placement of the thermocouple junction such that the junction will take on the temperature of the surface. The thermal contact between the junction and the surface is critical especially in regions where there are temperature gradients. Such is the case for the present supersonic flow where property variations are large across the boundary layer.

The flare was fabricated with two internal iron-constantan thermocouples located at $x = 12.5$ cm along $\phi = 90°$ and $\phi = -90°$. The exact thickness existing between the outside surface and the internal junction was not known but was estimated to be 0.5 mm. Unfortunately, the leads from one thermocouple were broken off inside the flare just prior to the LISF measurement runs. This left only one functional thermocouple to measure the surface temperature. Effort was then focused on verifying the reading from the existing thermocouple and/or obtaining a new, more accurate indication of the surface temperature. In the following discussion, the thermocouple located within the flare will also be referred to as the reference thermocouple.

The first attempt to make a new surface temperature measurement involved drilling a hole at an angle from the rear of the flare toward the outside surface of the afterbody. The drilling was complicated by the epoxy and pressure tubes exiting the rear of the flare. An iron-constantan thermocouple was peened inside the hole in contact with the flare material closest to the outside surface to be measured. The temperature distribution results from a test run indicated a very slow response. It was concluded that the thermocouple was not close enough to the outside surface.

Next, two type-E thermocouples were bonded to the aluminum surface of the flare. One thermocouple was bonded with Omega Engineering, Inc. (Stamford, Connecticut) thermally conducting epoxy whereas the second thermocouple was bonded with typical RTV epoxy with a much lower thermal conductivity. The amount of epoxy applied was kept to a minimum. During a run, the temperature distribution from the RTV bonded thermocouple immediately declined to a temperature value near the adiabatic wall temperature. This probably indicated that some epoxy got between the junction and the surface, preventing proper contact. Thus, the RTV epoxy served as an insulator between the surface and the thermocouple junction so that the thermocouple gave an indication of the air temperature instead of the surface temperature.

The thermally conductive epoxy should alleviate the possibility of insulating the surface from the thermocouple. The temperature distribution from the thermocouple bonded with the thermally conductive epoxy compared favorably to the distribution from the reference thermocouple. One small discrepancy in the two distributions was evident very early in the runs as the externally bonded thermocouple indicated a sharper decline in temperature than the reference thermocouple. The externally bonded thermocouple reached a level systematically 2 K lower than the reference thermocouple. The thermocouple bonded to the surface—even if there was excellent contact with the surface—could still indicate a temperature lower than the actual surface temperature due to the temperature gradients in the boundary layer and the bead's finite height.

One Omega Cement-On thermocouple was installed on the aluminum surface of the flare. This commercially fabricated thermocouple was specifically designed to measure the temperature of the surface to which it is attached. The 0.254 mm diameter leads were embedded in a 0.0127 mm thick foil

which was subsequently attached to the surface with thermally conducting epoxy. After an initial period of run time, the readings from this thermocouple were slightly higher than the reference thermocouple in the flare. At the end of a typical three minute run, the Cement-On thermocouple indicated a temperature some 2 K to 5 K higher than the internal thermocouple.

Other thermocouples were employed to measure the surface temperature. The results from these thermocouples, and the results described above, led to the conclusion that the thermocouple fabricated inside the flare gave the best indication of the surface temperature. This thermocouple was used throughout the LISF data acquisition segment to provide a measure of the surface temperature.

The initial surface temperature of the model varied from run to run. Prior to the first run of the day, the entire model was at room temperature. During the run the surface temperature would decrease as shown in figure 13. Immediately after a run, the surface temperature was usually cold enough to cause condensation to form on the surface. Condensation prevented LISF measurement runs since the moisture would interfere with the oil. Between runs, either an adequate amount of time was allowed for the model to warm up to room temperature or a heat gun was used to speed the warming process.

3.4.4 Effect of Plastic Film

The accurate indication of the surface temperature was complicated somewhat by the clear plastic that was attached to the flare. Although the clear plastic was necessary to provide a proper surface to accomplish LISF measurements, its presence could impact the indicated temperature from the thermocouple below the surface. In order to estimate the effect that the clear plastic had on the indicated temperature, use was made of a heat transfer correlation. Although there are large property variations across the boundary layer in high-speed flows, a constant property correlation can be used (ref. 40) if the terms are evaluated at a proper reference temperature such as the Eckert reference temperature, T^*, which is defined by

$$T^* = T_\infty(0.5 + 0.039M_\infty^2 + 0.5\frac{T_s}{T_\infty}) \qquad (3\text{-}42)$$

where T_∞ and T_s are the free-stream and surface temperatures, respectively. With this reference temperature, Chapman (ref. 41) recommends the following heat convection correlation

$$St_x^* Pr^{*2/3} = (0.185)(logRe_x^*)^{-2.584} \qquad (10^7 \le Re_x^* \le 10^9) \qquad (3\text{-}43)$$

where St^* is the Stanton number, Pr^* is the Prandtl number, and Re_x^* is the Reynolds number. All three of these terms are evaluated at the Eckert temperature. After solving for the Stanton number from equation (3-43), the convective heat transfer coefficient, h, can be computed from the equation

$$h = \rho^* U_\infty C_p St^* \qquad (3\text{-}44)$$

The heat flux (q'') through the surface can be calculated by

$$q'' = h(T_s - T_{aw}) \qquad (3\text{-}45)$$

The adiabatic wall temperature, T_{aw}, is determined by using the recovery factor r which equals

$$r = \frac{T_{aw} - T_\infty}{T_t - T_\infty} \qquad (3\text{-}46)$$

The recovery factor, as is typical for supersonic turbulent flow of air, was assigned the value of 0.89.

Knowing the computed heat flux and the properties and dimensions of the intervening materials, the difference between the surface temperature of the plastic and the temperature sensed by the reference thermocouple can be computed. Using standard operating conditions and the analysis outlined by equation (3-46), the difference between the temperature as indicated by the thermocouple and the surface temperature $(T_{tc} - T_s)$ on top of the plastic was computed to be 0.6 K. This implies that for runs conducted with the clear plastic on top of the model, the indicated value of the surface temperature as sensed by the reference thermocouple would be in error by approximately 0.6 K. This high reading would result in calculated viscosity based on T_{tc} some 1.2% lower than the actual value based on T_s. Thus, the resulting shear stress would likewise be computed to be 1.2% low. For the present results, the effect of the clear plastic on the thermocouple reading was neglected.

Ideally, the oil temperature should be measured at the exact location of the LISF measurement during that run. This leads to a question concerning the accuracy of measuring the temperature at a single location on the flare and assuming the entire model (flare plus cylinder) is at that same temperature. Unfortunately, the particular cylinder used did not contain any thermocouples. A run was made with an iron-constantan thermocouple secured to the cylinder surface. The temperature distribution from this thermocouple was comparable to the reference thermocouple inside the flare. It was thus concluded that the temperature as indicated by the reference thermocouple was representative of the entire surface of both the flare and cylinder.

3.5 Data Reduction

The data collected during an LISF run consists of the voltage output from photodiodes along with the previously cited pressure and temperature measurements. The method employed to analyze this information and deduce the skin friction will be discussed in this subsection. After the completion of a run, the stored data were transferred from the MicroVAX computer to the SUN SPARCserver 470 (Sun Microsystems Inc.) using Transl8 (Accelr8 Technology Corp., Denver, Colorado), a data translation software package. On the SUN, the data reduction routines were written specifically to be run by PV~WAVE (Precision Visuals Inc., Boulder, Colorado), a software package for visualizing and analyzing data.

3.5.1 Wall Temperature Correction

The first step in the data reduction process was to account for the variation of the oil viscosity with time as a consequence of the changing surface temperature. A reference temperature was chosen which establishes a reference viscosity in order to normalize the fringe record. The time data were corrected using equation (3-30). The new fringe record with the temperature corrected time is compared to the uncorrected fringe record in figure 14.

3.5.2 Identification of Extremes

Next, the peaks and valleys of the fringe record were identified. One such technique was to simply find every local maximum and minimum in the voltage signal and assign them to be the peaks and valleys. For this method, smoothing of the data may be required and was an available option in the reduction software. A drawback of this method was that the time at which the local maximum or minimum was identified may, in fact, not be consistent with what the actual intensity distribution indicates as being the extreme due to noise and the finite sampling rate.

An alternative approach to identifying the fringe peaks and valleys was used in reducing the present data. This approach includes an algorithm which first determines a running average of the voltage level of the signal from a predetermined number of data points. The program then detects when the signal crosses this level either with a positive or negative slope. Once the mean level was crossed, each succeeding point was placed into a new array until the signal crossed the mean level again. The data points in the new array represent either the upper or lower half of a fringe. A least-squares method was applied to find the best curvefit of a second-order polynomial to the data. This curvefit was applied to each peak and valley so that the time interval over which the curvefit was applied varied. The time at which the extreme occurred was then determined from the curvefit. The output from the routine was a plot of the individual curvefits and the time at which each extreme was calculated to have occurred. This method was not susceptible to mean level drift errors.

Once the fringe extremes were identified, the range of valid fringes to be analyzed was determined. This range was restricted in the present study in two ways. First, there was a finite amount of time required for the pressure in the tunnel to reach the desired operating level. From the measured pressure distribution, the time at which the total pressure reached a level within 2% of the final steady level was identified. This occurred between 10 and 60 seconds after the flow of air in the tunnel began. Second, fringes occurring early in the run were contaminated by surface waves. A simple method to check for surface waves involved computing the period between each fringe peak. The period length should decrease when moving backward in time. The point at which this inequality test did not hold true identified the first valid fringe.

3.5.3 Calculation of Fringe-Time Product

There are several different techniques to determine the fringe-time product from the valid range of the fringe record. One technique is to arbitrarily select three fringes and calculate the effective fringe and time using equations (3-40) and (3-41). These two results can then be multiplied together to yield the fringe-time product. One drawback to this technique is that random errors can impact one of the fringes selected and, hence, affect the outcome. This technique also wastes much of the fringe record since only three peaks were selected as the basis for analysis.

Instead of computing just one representative effective fringe number and oil flow time for the entire fringe record, another data reduction technique involves calculating an effective fringe and effective oil flow time for each extreme. Simply substituting the effective fringe-time product for the actual fringe-time product in equation (3-7) yields

$$\tau = \frac{2 n_o \rho_o \nu_o x \cos \theta_t}{\lambda} \frac{1}{N' t'} \tag{3-47}$$

28

This equation can be rearranged into the form

$$N' = \frac{2n_o\rho_o\nu_o x \cos\theta_t}{\tau\lambda}\frac{1}{t'} = \frac{1}{C_1}(\frac{1}{t'})$$ (3-48)

The term C_1 should be constant during a particular run and was defined previously in equation (3-9). If the value of the effective fringe calculated for each extreme is plotted versus the reciprocal of the effective oil flow time, $\frac{1}{t'}$, the data should collapse along a straight line. The slope of the line is equal to $\frac{1}{C_1}$. By performing a linear least-squares curvefit to the data, the slope best representing the data can be determined. Finally, knowing C_1, the shear stress can be calculated from equation (3-9).

However, applying this approach to the experimental data revealed that particular care must be exercised in calculating the effective fringe and oil flow times. Initially, the effective values for each extreme were calculated based on the two previous extremes. The data from extremes which occurred later in the run did collapse along a particular line as shown in figure 15. These later data points are grouped close together near the origin of the plot. In contrast, fringes that occurred early in the run diverged significantly from this line and did not follow the expected trend. This behavior was attributed to random errors in the data acquisition and reduction process. These random errors are more visible in figure 15 because of the particular coordinate axes of the plot. Fringes that occur earlier in the run have shorter periods. As these periods grow shorter and shorter as the analysis proceeds backward in time, the effect of the random errors becomes more significant. In plotting the data on a reciprocal time scale, the fringes occurring earlier in the run are spread out over a larger region of the graph. Any random errors appear to be amplified since the reciprocal of small periods is large.

In light of this, a different method of calculating the effective fringe and effective oil flow times was implemented. The method was first described by Kim (ref. 27) who referred to it as the "total-peak method." The effective values for a particular extreme were calculated based on all the possible combinations of two other extremes. The results from all of these combinations were averaged to obtain an effective fringe and oil flow time based on the total fringe data. This method should alleviate the effects of random errors that were the cause of the divergence of the earliest fringes from the expected line. Figure 16 is a plot of the results from the total peak method. In comparison to figure 15, it showed significant improvement. However, the earliest fringes still tended to diverge somewhat from the expected trend. A straight line was then fit through the data and the reduced chi-square error associated with that line was calculated. The earliest fringe was removed from the analysis and the effective values for the remaining extremes in the interval were re-calculated. The slope of the line and the associated reduced chi-square were calculated for this new range of fringes. This was repeated over all possible fringe combinations. The particular fringe combination which yielded the lowest reduced chi-square was selected as being the best fit to the theory. The slope of the best-fit line yielded the fringe-time product for the run.

Another method of data reduction is the incremental-peak method as outlined in equation (3-8) through equation (3-20). The curvefit of the incremental fringe number (k_i) was first applied to all the fringes within the valid interval (fig. 8) to yield a value for the fringe-time product (Nt). The earliest fringe was removed and the analysis was repeated resulting in a new fringe-time product. This process continued until there were only four extremes left in the interval. All of the fringe-time products were averaged together and a standard deviation was computed which typically was around 2%. Considering the entire range of fringes again, the latest fringe was removed from the interval and the process of

calculating the fringe-time product was repeated by removing the earliest fringes in succession. Out of all possible fringe combinations, the one selected was based on the highest value of the correlation coefficient. Following Holman (ref. 42), the correlation coefficient, r_c, is a measure of how well the data fit the curvefit based on the theory and is defined by

$$r_c = \left[1 - \frac{\sigma_{k,x}^2}{\sigma_k^2} \right]^{1/2} \tag{3-49}$$

where

$$\sigma_{k,x} = \left[\frac{\sum_{i=1}^{n}(k_i - k_{ic})^2}{n - 2} \right]^{1/2} \tag{3-50}$$

and

$$\sigma_k = \left[\frac{\sum_{i=1}^{n}(k_i - k_m)^2}{n - 1} \right]^{1/2} \tag{3-51}$$

The actual values of the incremental fringe number are represented by k_i, the computed incremental fringe number from the curvefit is given by k_{ic}, the arithmetic mean is k_m, and n is the number of data points.

The total-peak method and the incremental-peak method were both used to reduce the LISF data. Both methods gave the same average fringe-time product over all of the possible fringe combinations. It was observed that the standard deviation of the fringe-time product using the total-peak method was slightly larger than when using the incremental-peak method. This is probably a consequence of the divergence of the earliest fringes from the curvefit for the total-peak method. When using the best curvefit as the criterion for selecting the representative fringe-time product, both typically gave the same answer. The incremental-peak data reduction results are reported in this study.

3.5.4 Calculation of Skin-Friction Coefficient

After a representative value for the fringe-time product was determined, the shear stress at the wall was calculated according to equation (3-20). Included in the software to calculate the shear stress are system inputs such as beam incidence angle and the distance from the leading edge. The viscosity of the oil was determined by the reference surface temperature used in the time-correction procedure. The total pressure and temperature were averaged over the time interval of analysis of the fringe record. The total density of the air was calculated using these two values. The free-stream density of the air, ρ_∞, was calculated from the total density assuming a Mach number of $M_\infty = 2.89$. The free-stream velocity was computed from the Mach number and the average total temperature. Finally, the shear stress results were nondimensionalized by upstream free-stream conditions using

$$C_f \equiv \frac{\tau}{\frac{1}{2}\rho_\infty U_\infty^2} \tag{3-52}$$

where C_f is the skin friction coefficient based on upstream conditions.

3.5.5 Reduction Software Check

The LISF reduction software was checked by analyzing a data record from a computer simulated run with known flow quantities and shear stress. The computer simulated run typified the experimental

runs in the present study. The first step in generating the simulated data set was to assume a surface temperature versus time distribution similar to an experimental distribution. With the predetermined shear stress at the wall, and the oil viscosity value varying as the surface temperature, a simulated fringe record was generated and stored in a file formatted like an actual data file. The data simulation rate was comparable to the experimental data acquisition rate. The data reduction software was then used to analyze the simulated data. The fringe identification routine was applied to the simulated fringe record corrected for the surface temperature distribution. The time at which each extreme occurred was checked to validate the peak finding routine. The best fringe-time product was determined. Finally, the shear stress was calculated and compared to the value used to generate the simulated fringe record. The final shear-stress results were within 1% of the value used to generate the data.

4 RESULTS AND DISCUSSION

4.1 Oil Flow Visualization

Prior to the presentation of the oil-flow visualization results, some general remarks will be made concerning the interpretation of the oil-flow records and the terminology employed. The description of the results will then begin with the postulated skin-friction line pattern noting, in particular, the location of the singular points. Then, certain aspects of the flow will be discussed in detail such as the upstream influence, the separation lines, and the attachment line. Finally, the discussion will focus on the observed topology near the $\phi = 180°$ line of symmetry.

4.1.1 Preliminary Discussion of Surface Topology

Detailed discussions of surface flow topology can be found in Maskell (ref. 43), Wang (ref. 44), Peake and Tobak (ref. 45), and Chapman (ref. 46). In 2-D flows, a line of separation can be identified as the position at which the surface shear stress goes to zero. However, separation in 3-D flows is not as easy to define. Along a 3-D separation line, the surface shear normal to that line does vanish but the tangential component of surface shear typically does not. It is only at specific locations known as singular points that both components of surface shear are identically zero.

The two main types of singular points, as taken from Peake and Tobak (ref. 45), are saddles and nodes. A saddle point is the intersection of only two skin-friction direction lines. One of these lines proceeds inward into the saddle from both sides and the second line proceeds outward from the saddle on both sides. These skin-friction lines that pass through a saddle point are also referred to as separatrixes (ref. 46). All other skin-friction lines in the vicinity of the saddle maintain the same general direction as these two separatrixes but avoid the saddle point itself. The saddle may be a point of separation or of attachment. The distinction between the two is that fluid leaves the singular point on the surface for a saddle of separation whereas fluid enters the singular point on the surface for a saddle of attachment. In either case, the surface topology of the skin-friction lines appears the same.

Nodes, the second main type of singular points, can be further divided into nodal points and foci. A nodal point possesses an infinite number of skin-friction lines which are directed outward for a nodal point of attachment and inward for a nodal point of separation. Foci differ from nodal points in that the skin-friction lines spiral into a focus of separation and spiral out of a focus of attachment.

During an oil-flow visualization run, the oil droplets do not lift off the surface at separation, but instead turn and converge together to form a line of oil accumulation. As the shear of the upstream flow pushes oil downstream and the shear of the flow in the separated region pushes oil upstream, the oil accumulates near the actual separation line. McCabe (ref. 47) conjectured that the oil accumulates just upstream of the actual separation line where there is a balance of the viscous forces and the force as a result of the large pressure gradient near separation. The proximity of the oil accumulation line to the actual separation line is dependent on the thickness of the oil. The difference of these two locations, however, is probably not significant for most cases. For this study, therefore, the location of the oil accumulation line in the oil-flow visualization has been assumed to be equivalent to the separation line.

A possible disadvantage of the accumulation of oil near the separation line is that the oil ridge may influence the flow.

Combining this behavior of oil streaks in the vicinity of a separation line and the knowledge concerning singular points leads to the following definition for a line of separation: the existence of a particular line emerging from a saddle point of separation upon which other oil-streak lines converge (ref. 48). The distinction that the saddle point must be one of separation is particularly important in this study. Note that this definition has been put forth in order to assist in the interpretation of the present results. It is not intended to be an all-encompassing definition of separation since there are aspects of 3-D separation which are still open to debate.

Figures 17 through 19 are views from different angles of the model after one run. The flow was from left to right. In figure 17, a saddle point was visible on the cylinder along $\phi = 0°$ which was aligned with the top of the cylinder in the photograph. The separation line emanating from this saddle point was evident as both the downstream and upstream oil streaks in the vicinity converged upon that line. The general location of the attachment line was visible on the flare. In figure 18, the streamwise extent of the separated zone was evident. The oil streaks on the flare downstream of attachment demonstrated turning toward the conical flow direction. Figure 19 illustrated the general nature of the flow near the $\phi = 180°$ line of symmetry. Figure 20 is a view of an oil-streak pattern on the model after a different run and provides more detail in the region near the $\phi = 180°$ line of symmetry. Figures 21 through 23 are a series of photographs of the three unwrapped MonoKote sections of the cylinder, flare, and afterbody after removal from the model.

4.1.2 Upstream Region

Upstream influence is an important characteristic of the interaction. From the oil-flow records the upstream influence location (x_u) was identified by locating the point that the oil streaks began to deflect from their original free-stream direction. For this study, the upstream influence length ($l_u \equiv x_j - x_u$) was defined as the distance between the upstream influence location and the cylinder-flare junction (x_j). For the region in the vicinity $\phi = 0°$ and for the region between $\phi = 165°$ and $\phi = 180°$, the extent of the upstream influence could not be detected from the oil-flow records since the flow, prior to separation, continued in the same direction as the free-stream flow. The upstream influence data from the oil-flow records is summarized in table 5. The upstream influence increased with increasing azimuthal angles until $\phi = 120°$. Information apparently propagated around the model such that the interaction along the $\phi = 0°$ line of symmetry affected the rest of the surface flow.

The interpretation of the oil-flow visualization results is shown in figure 24. An unwrapped pattern is shown in figure 25. Note, not all of the details of the interaction were clearly documented with a single run. Instead, numerous runs employing different fluids were taken together to provide a data base by which the interpretation was deduced. The video record of the temporal development of the oil flow complemented the process of tracking individual oil streaks and interpreting the results. There were a total of seven nodes and five saddles, thus satisfying the topological law (ref. 46) that for a closed 3-D surface, the number of nodes must exceed the total number of saddles by two (7 nodes − 5 saddles = 2). The locations of the singular points for one side of symmetry are summarized in table 6. The front nodal point of attachment ($N6$, not shown) was located on the upstream tip of the cylinder and was the source of the skin-friction lines that proceeded downstream along the cylinder toward the interaction.

33

There was a nodal point of separation ($N7$, also not shown) at the rear of the cylinder. This node served as a sink for the skin-friction lines proceeding along the cylinder downstream of the flare.

4.1.3 Separated Region

The undisturbed flow first encountered the influence of the shock wave along $\phi = 0°$. The boundary layer could not overcome the streamwise adverse pressure gradient and the flow subsequently separated. A saddle of separation ($S1$) was formed along $\phi = 0°$ as was a nodal point of attachment ($N1$) near the cylinder-flare junction. The combination of a saddle point of separation and nodal point of attachment forms what is called global separation (ref. 45). The primary separation line proceeded out of $S1$ in both directions from the line of symmetry. This separation line prevented skin-friction lines that originated from $N6$ located upstream at the cylinder tip from crossing the skin-friction lines that emanated from $N1$ on the flare along $\phi = 0°$. The skin-friction line, or separatrix, that entered the saddle of separation $S1$ divided the flow into the two symmetric regions.

The separation line that emanated from $S1$ continued along the cylinder until it entered into the downstream focus of separation $N3$. The path of this line of separation can be thought of as a base for the dividing surface that originated at the model surface and then rolled up. The flow above the surface in this vicinity will be referred to as a vortex. The position of the separation line that emanated from $S1$ for $\phi = 0°$ to $\phi = 150°$ is given in table 7. The uncertainty for these locations is estimated to be ± 0.2 cm due, in part, to the thickness of the oil accumulation line. A second separation line proceeded outward from the saddle point $S4$ located on the $\phi = 180°$ line of symmetry, and its location is also summarized in table 7. This separation line was perpendicular to the free-stream direction along most of its length. The line eventually spiraled into the focus of separation $N2$.

There was well-defined or tight convergence of the oil streaks originating upstream of the interaction upon the separation line for the smaller azimuthal angles. The convergence was not as tight for the oil streaks along larger azimuthal angles. Similarly, for oil streaks within the separated zone, those along smaller azimuthal angles converged more tightly onto the separation line than those at the larger azimuthal angles. The convergence of oil streaks upon the separation line proceeding out from $S4$ was very tight as would be expected since this line was perpendicular to the incoming flow. The lack of tight convergence made it difficult to determine the path of the primary separation line from $S1$ as it approached the $\phi = 180°$ line of symmetry. Most of the experimental runs indicated that this separation line proceeded into the downstream focus $N3$. In contrast, this separation line appeared in some runs to proceed into the upstream focus $N2$. It was concluded that the separation line originating at saddle point $S1$ proceeded into the downstream focus $N3$ as depicted in figure 25.

4.1.4 Attachment Region

Attachment is a location at which the flow above the separated zone impinges upon the surface. The attachment line has traditionally been defined for the oil-flow records as that line in which the skin-friction lines diverge and is associated with a line of separation. Hung, Sung, and Chen (ref. 48), however, point out that the condition that the skin-friction lines be divergent is ambiguous since all of the lines are divergent at the source. These same authors proposed a new definition for a line of attachment as that "skin-friction line emanating outward either from a saddle point of attachment or a nodal point of attachment and having the property of dividing its surrounding flow topology into two

34

definable sets or groups." However, according to this definition, there are other lines that meet these conditions that are not attachment lines. These definitions are more operational than rigorous. In the absence of a proper definition of an attachment line based on theoretical analysis, an attachment line was identified from the oil-flow records based on appearance. This attachment line emanated from $N1$ and was located near the cylinder-flare junction from $\phi = 0°$ to $\phi = 20°$ though its exact location was not evident from the oil-flow records in this region due to the close proximity of the line to the cylinder-flare junction. The attachment line was visible on the flare around $\phi = 20°$ at $x = 0.40$ cm and continued along the flare until it proceeded into the saddle of attachment ($S5$) at $x_a = 7.82$ cm. The attachment line never ventured more than 1.0 cm from the cylinder-flare junction at any location along its path. The maximum distance between the attachment line and the cylinder-flare junction occurred around $\phi = 90°$. The location of the attachment line is summarized in table 8.

4.1.5 $\phi = 180°$ Region

The following discussion of the surface topology in the vicinity of $\phi = 180°$ line of symmetry will be limited to one side of the symmetric flow. The saddle point of attachment $S5$ was located at the intersection of the attachment line and the line of symmetry along $\phi = 180°$. This saddle of attachment was directly connected to the upstream saddle point of separation ($S4$) by a separatrix. In the past, a direct connection between two saddle points has been considered unstable. Chapman (ref. 46) made an exception to this for cases with strong symmetry. This was experimentally illustrated in the Batcho and Sullivan (ref. 49) study of a supersonic boundary-layer corner interaction in which a saddle of separation was connected to a saddle of reattachment along a line of symmetry. The interaction occurred within a rectangular test section with a 2-D compression ramp which spanned the entire width of the tunnel. Other studies have also shown such saddle-to-saddle connections. Green (ref. 50) referred to a 2-D geometric experiment with an impinging shock that resulted in a highly 3-D flow field. The oil flows revealed a saddle-to-saddle connection along the tunnel wall centerline. Cambier and Escande (ref. 51) calculated the flow in a transonic channel test in which the experimental oil flows revealed a saddle-to-saddle connection on the two side walls. It is possible that for the present flow, the resolution of the oil-flow record was not adequate so as to indicate certain details such as other singular points which may have been present. One other possibility is that the separatrixes from the two saddles narrowly miss each other. This is unlikely, though, since both saddles are situated along a line of symmetry. It was assumed that the saddle-to-saddle connection along $\phi = 180°$ was plausible as a result of strong symmetry.

The separation line emanating from the saddle point $S4$ along $\phi = 180°$ was essentially perpendicular to the free-stream direction of the incoming flow. The region downstream of this separation line was of very low skin friction as the oil droplets did not move in many test runs except for cases with oil mixtures of low viscosity. The separation line which emerged from saddle $S4$ encountered one leg of the separation line originating from the saddle point of separation $S2$ and coiled to form the focus of separation $N2$. The other leg of the separation line from $S2$ spiraled into the focus of separation $N3$ and served as the base for a dividing surface which coiled around the fluid that lifted off the surface.

Referring again to figure 25, one side of the separatrix that proceeded into saddle $S2$ originated upstream of the interaction from node $N6$. This separatrix can be thought of as a divider between the skin-friction lines on one side of symmetry that eventually entered the upstream focus $N2$ and those that entered the downstream focus $N3$. The path of the separatrix was estimated to originally lie between

$\phi = 130°$ and $\phi = 135°$ in the undisturbed region. Oil streaks from the smaller azimuths converged onto the separation line which proceeded from saddle $S1$ which terminated at the downstream focus $N3$. Oil streaks between $\phi = 130°$ and $150°$ eventually proceeded into the upstream focus $N2$. The oil streaks between $\phi = 150°$ and $\phi = 180°$ converged upon the separation line emanating from $S4$ which eventually spiraled into the focus $N2$. The other side of the separatrix, within the separated region, that entered saddle $S2$ originated from node $N1$. This line can be thought of as a divider of the skin-friction lines, originating from $N1$, that proceeded into the focus $N2$ and those entered focus $N3$. This separatrix within the separated region was especially evident from the temporal progression of the oil flows as recorded by video. Within the separated region, oil streaks close to the $\phi = 180°$ line of symmetry proceeded upstream and converged onto the separation line proceeding from saddle $S4$ and eventually into $N2$. Other oil streaks displaced slightly farther from the symmetry line proceeded upstream and spiraled into the focus of separation $N3$.

As the vortex proceeded from the $\phi = 0°$ line of symmetry along the side of the model, some of the low-energy fluid passing over the vortex was entrained. The flow attached to the flare minus the lower-momentum portion which was entrained. In contrast, a closed bubble-type 2-D separation is inaccessible to fluid outside the bubble. For 3-D separation, with the addition of fluid as the result of entrainment, the buildup of fluid must be ventilated in some manner. The foci near the bottom line of symmetry of the present flow provided such a means. The trajectory of these vortices after they left the surface will be further discussed in the next subsection.

Downstream of attachment on the flare, the oil streaks indicated that the flow turned toward the conical flow direction (fig. 22). The oil streaks on the cylindrical afterbody were aligned with the free-stream direction (fig. 23). The noticeable deviations that occur around $\phi = \pm 90°$ are the result of extraneous shock waves originating from the side wall.

The surface topology, as visualized by the oil flow technique, was interesting especially near the $\phi = 180°$ symmetry. It does not, however, lend itself to an easy extension of the interpretation to the flow away from the surface. Caution should be used when attempting to construct the external flow model based solely on the surface flow patterns. Thus, methods to visualize the flow above the surface were employed to assist in the development of the complete flow model as discussed next.

4.2 Laser Light Sheet

The first attempt of seeding the flow for the laser light sheet investigation utilized the LDV seeding system. The first injectant consisted of only water and the second injectant attempted consisted of water, alcohol, and latex particles. Both injectants yielded a uniform distribution of aerosol throughout the tunnel. However, the light scattered by the aerosols was faint and no features of the flow were discernible. Apparently, the seeder system was not capable of delivering the amount of aerosol to have the high density of aerosol necessary for proper scattering from the light sheet.

In response, the mode of seeding was switched from global to local. In this way the aerosol could be concentrated into a small region of interest. This was accomplished by injecting different fluids

through selected pressure taps on the cylinder. The three fluids tested were alcohol, acetone, and ether. For the present experiment, ether was found to work best due to its lower vapor pressure.

A sequence of images is shown in figures 26 through 31. The flow was from left to right and the camera viewed the light sheet from an angle below the model. Ether was injected through a pressure tap located upstream of the interaction along the $\phi = 180°$ azimuth. When the light sheet was located upstream of the interaction (not shown) the light scattering aerosol was confined to a half-circular region near the surface. The outline of the scattered light indicated the extent of the seeded area. In figure 26, the light sheet was positioned in the separated region upstream of the cylinder-flare junction. As the aerosol progressed into the interaction region, it was lifted away from the surface. This is evidenced in figure 26 by the dark region near the surface indicating an absence of light scattering aerosol. Apparently, the shear layer that proceeded over the separated region was visualized.

Near the cylinder-flare junction, the image began to take on a unique intensity distribution shown in figure 27. The region along $\phi = 180°$ was very bright as was a thin layer very near the surface indicating a higher concentration of aerosol in those regions. The region near the flare surface is also brighter as a result of scattered light off the model itself. Figures 26 through 31 are photos at different streamwise locations and all possess the same characteristic intensity distribution. It is thought that the aerosol that originally proceeded over the separated region was squeezed toward the symmetry line by the outer flow and some aerosol was brought down to the surface through the attachment process. The common flow of the two main vortices was upward along the symmetry line. This would result in a spreading of the aerosol in the direction away from the model surface along the symmetry line.

In order to investigate this behavior further, the flare was rotated 20° and ether was injected through the same tap in the cylinder upstream of the interaction. The injected liquid was now along an azimuth rotated 20° with respect to the $\phi = 180°$ line of symmetry. Again, the brightest intensity of the scattered light was along the $\phi = 180°$ azimuth on the flare. This indicated that the unique intensity distribution was not just the result of the injection location since the injected fluid tended to accumulate along the plane of symmetry and not along the plane of injection.

An image with some similarities to the present images was reported by Garrison and Settles (ref. 52) in a visualization study of the interaction of a symmetrically crossing SW/BLI. Two fins at an angle of attack produced two oblique shocks which crossed and interacted with a turbulent boundary layer existing on a flat plate. The experiments were conducted at nominal Mach numbers of 3 and 4. The surface visualizations revealed two separation lines ahead of the fins which initially proceeded toward each other. Near the line of symmetry, these two lines were seen to turn downstream and proceed parallel to the line of symmetry. To obtain more details of the flow along the line of symmetry, ethanol was injected through a pressure tap in the flat plate upstream of the interaction. A laser light sheet was projected into the tunnel to visualize the aerosol. The images were described as possessing a mushroom-shaped separation structure. This shape was thought to be the result of the initially thin separated zones getting squeezed near the line of symmetry and becoming more vertically oriented.

The present flow possessed two separated regions which proceeded toward a line of symmetry ($\phi = 180°$). These two vortices were squeezed toward the line of symmetry and eventually left the surface and proceeded downstream within the boundary layer. This behavior would follow from the

intensity distributions of the images on the flare. The two vortices were believed to be located within the region close to the surface which was not illuminated in the image (fig. 32).

The laser light sheet illumination study did complement the surface topology findings even though it did not document the flow above the surface in detail. The postulated flow structure along the $\phi = 0°$ line of symmetry consisted of separation, which spiraled into a vortex, followed by attachment on the flare. The vortex continued along the model on both sides of symmetry. Near the $\phi = 180°$ line of symmetry, the postulated flow structure included two main vortices which left the surface at the foci of separation ($N2$ and $N3$) and remain embedded within the boundary layer on the flare (fig. 33). Along $\phi = 180°$, the visualized images from the light sheet indicated a flow structure consistent with this postulated flow structure.

4.3 Laser Doppler Velocimetry

A laser Doppler velocimeter was used to document the velocity field of the undisturbed boundary layer upstream of the interaction. The data provided information concerning the initial boundary-layer properties and served as a basis to judge the quality of the boundary layer. In addition, the skin friction was deduced from the mean streamwise data and served as a check on the LISF results. The LDV system was operated with both two and three channels to acquire the velocity data. The data in each channel were acquired simultaneously and then resolved into orthogonal components in the streamwise, vertical, and transverse directions.

A total of 10 mean-velocity profiles between the streamwise locations of $x = -2.0$ cm and $x = 1.0$ cm were analyzed. A typical profile of the streamwise component of mean velocity is shown in figure 34 and presented in table 9. A plot of the fluctuating velocity components is shown in figure 35. This particular profile was obtained with a 3-D LDV system so that all six Reynolds stress components could be evaluated. The distributions of the three normal stresses demonstrated the expected anisotropy of the boundary-layer turbulence with the streamwise normal stress being the largest near the wall. The $< u'w' >$ and $< v'w' >$ shear stresses should be zero in an axisymmetric boundary layer and were nearly so for the data. The $< u'v' >$ shear stress exhibited the typical distribution obtaining a maximum value near the wall.

The experimental mean streamwise velocity profiles served as data from which the local skin friction could be deduced by what are called "indirect" methods. The analysis of Sun and Childs (ref. 16) was applied to the experimental velocity profiles by curve fitting their wall-wake correlation to the data. Referring back to figure 34, the curvefit of Sun and Childs' wall-wake correlation to the data is shown as a solid line. The agreement between their universal correlation and the data implied that the turbulent boundary layer was fully developed. The wall-wake correlation, as would be expected, showed deviations below $y/\delta = 0.1$ and above $y/\delta = 0.9$. Otherwise, no other differences were observed between the data and the curvefit for all of the profiles along the length of the cylinder as would be expected for self-preserving boundary layers. The wall-wake curvefit yielded a value for the local shear stress and the boundary-layer thickness. The results of the analysis are given in table 10. Note that the skin friction was deduced from mean-velocity data acquired in the boundary layer on top of the cylinder whereas the LISF data were acquired along the side of the model. The velocity data,

as acquired by three different LDV configurations (2-D, 3-D symmetric, and 3-D nonsymmetric), were analyzed to yield a mean value for the skin friction of $C_{f_x} = 0.00144 \pm 1.6\%$.

4.4 Surface Pressure

The pressure data acquired during this study have been divided into two sets. The first set, which is not presented here, consists of data obtained when the $\phi = 0°$ azimuth of the flare was aligned with the top of the cylinder. The extent of this set is restricted, however, because data on the cylinder could be collected for only four azimuths ($\phi = 0°$, $90°$, $180°$, and $270°$) when the flare was located in this one position. Consequently, a second set of data is presented in this report and consists of pressure measurements performed along azimuths when each of the individual azimuths was aligned with the top of the cylinder. In other words, the pressure distribution for $\phi = 15°$ was obtained when the flare was rotated $15°$ from its position during the first set such that the row of taps on the flare was aligned with the top row of taps on the cylinder. This second set of data required that the flare be rotated to 13 different positions during the investigation.

The surface pressure distributions along each azimuth are presented in tables 11 through 23 and are shown graphically in figures 36 through 48. The pressure data on the flare were averaged over two runs. The runs were conducted at a total pressure of $P_t = 172.37 \pm 0.4\%$ kPa. The average value of P_∞/P_t as measured by the most upstream cylinder tap was $0.0332 \pm 0.6\%$ indicating a free-stream Mach number of $M_\infty = 2.87$. For measurements along $\phi = 0°$, only five cylinder taps were exposed whereas the rest of the taps were covered by the flare. Due to the sweep of the flare, measurements along larger azimuths allowed more of the taps on the top of the instrumented cylinder to be exposed. Hence, the surface pressure distribution of the undisturbed boundary layer was most extensively documented for the $\phi = 180°$ azimuth which is shown in figure 48. The undisturbed static pressures decreased slightly along the length of the cylinder in the downstream direction. Along a length of 6.5 cm, the drop in the undisturbed pressure with respect to the most upstream value was 2.2% which amounts to an increase in Mach number of 0.3% to $M_\infty = 2.89$. This very small pressure gradient in the upstream boundary layer was deemed to have had a negligible effect on the interaction.

4.4.1 Upstream Region

An example surface pressure distribution plot is shown in figure 49 for illustrative purposes. The generated shock caused instantaneous deflection of the flow outside the viscous dominated boundary layer. Within the subsonic portion of the boundary layer, the pressure disturbance associated with the shock was transmitted outward, including upstream of the shock. The point at which the pressure measurements first indicated a disturbance will be referred to as the upstream influence location, x_u. A consistent method of determining this location from the pressure distributions was accomplished by first drawing a line through the steepest slope of the initial rise in the pressure distribution as shown in figure 49. The intersection of the projection of this line down to the free-stream pressure level was taken to be the upstream influence location. The distance between the cylinder-flare junction and the upstream influence location will be referred to in this study as the upstream influence length ($l_u \equiv x_j - x_u$).

A summary of the upstream influence lengths is presented in table 24. The flow along $\phi = 0°$ line of symmetry was the first to experience the effects of the interaction. The upstream influence length of $l_u = 0.54$ cm along $\phi = 0°$ was a minimum for all of the azimuths. The upstream influence length for $\phi = 15°$ was slightly larger than for $\phi = 0°$ indicating 3-D effects. This increase in upstream influence was the result of the effects of cross-flow and the transverse spread of the effects of the pressure disturbance. Overall, the upstream influence length increased with increasing azimuths to a maximum of $l_u = 2.49$ cm in the vicinity of $\phi = 120°$. The upstream influence lengths indicated by the pressure measurements were consistently less than those indicated by the oil flows.

The variation of upstream influence with azimuthal angle is evident in figure 50, where the pressure distributions from five azimuths have been plotted in terms of $x - x_j$. In other words, the pressure distributions in this figure were plotted such that the location of the cylinder-flare junction for each azimuth was coincident. With a change in the abscissa, the same pressure distributions are shown in figure 51 with an abscissa of $x - x_u$ so that the upstream location for each azimuth was coincident. Examining the distributions prior to separation in the so-called free-interaction zone, the distributions of $\phi = 0°$ and $\phi = 15°$ (not shown) are very similar. The value of the initial pressure gradient prior to separation decreases with increasing azimuthal angles from $\phi = 15°$ to $\phi = 60°$. The distributions from the initial disturbance through the initial inflection point for $\phi = 60°$ through $\phi = 120°$ collapsed onto a single line indicating the same value for the initial pressure gradient. The pressure gradient increased for $\phi = 135°$ and, finally, the distributions for $\phi = 150°, 165°$, and $180°$ collapsed onto a single line.

4.4.2 Separated Region

For some SW/BLI involving separation, the pressure distributions have exhibited a plateau region between separation and attachment. Such a plateau is visible in figure 49. This region of decreased $\partial P/\partial x$ relative to the initial pressure gradient is evident in the majority of the present distributions. The absence of a plateau region for the pressure distributions along $\phi = 0°$ and $\phi = 15°$ was possibly due to the small extent of the separated region in that vicinity. The location of separation for each of the remaining pressure distributions was estimated by identifying the inflection point just upstream of the pressure plateau. The results are presented in table 25. In comparison, the location of the separation line from the oil-flow results was consistently upstream of the pressure plateau region. One possible cause for the discrepancies is that the oil accumulates upstream of the actual separation line.

The pressure at the upstream inflection of the plateau region was taken as the separation pressure, P_s, and is also presented in table 25. The separation pressure could not be determined for distributions along $\phi = 0°$ and $\phi = 15°$ since the measurements did not indicate a plateau region. In general, the separation pressure demonstrated a decreasing trend with increasing azimuthal angles until a minimum was reached in the region near $\phi = 75°$. This minimum was near the region of largest sweepback of the cylinder-flare junction with respect to the free-stream direction which was centered in the vicinity around $\phi = 60°$. Stalker (ref. 53) observed that increasing the sweepback in swept compression corners increased the extent of the plateau region while also reducing the pressure at which the plateau was formed. The present data seem to follow such behavior.

4.4.3 Post-Attachment Region

The pressure gradient is typically largest at separation and at attachment. After attachment, the boundary layer experiences continued compression until the pressure eventually levels off and reaches a peak plateau. For the present corner-type interaction, the concave curvature tends to destabilize the flow and increase turbulent mixing. This increased turbulent activity allows the flow to penetrate regions of higher pressure such as is present on the flare after attachment.

The peak pressure level attained by the flow on the flare was compared to the expected inviscid peak pressure for a 20° right angle cone at zero angle of attack. From Sims[54], the inviscid peak pressure ratio P_{pk}/P_{∞} was calculated (for $M = 2.89$) to be 2.68. The rise in pressure along $\phi = 0°$ was 3.4% below the inviscid level whereas the pressure rise was 3.4% above the inviscid predicted level along $\phi = 180°$. From $\phi = 0°$ to $\phi = 30°$, the experimental peak pressure ratio increased with increasing azimuthal angles (table 26). This behavior is expected since the tendency was for the fluid to proceed from the smaller azimuthal planes toward the larger azimuthal planes. Thus, the thinner boundary layer along $\phi = 0°$ would result in a smaller effective cone angle that the flow experiences than along $\phi = 180°$ which has a much thicker boundary layer. The flow along $\phi = 0°$ traveled approximately 2.35 cm from the cylinder-flare junction in the streamwise direction, which amounted to 21% of the ramp length, before the pressure reached the peak plateau level. The other distributions were not as quick to reach the peak plateau level. In fact, the pressure distribution for $\phi = 165°$ and $\phi = 180°$ azimuths do not reach the peak plateau level until the flow had traveled approximately 70% of the length of the flare.

The boundary layer on the ramp experienced expansion at the corner of the ramp-afterbody and the pressure dropped substantially. The pressure at the first measurement location on the afterbody for each azimuth is presented in table 27. The pressure at this location decreased a total of 8% with increasing azimuthal angles between $\phi = 0°$ and $\phi = 75°$. Between $\phi = 75°$ and $\phi = 180°$, the pressure increased a total of 44% with increasing azimuthal angle. The general trend was for the fluid to move from the smaller azimuthal angles to the larger azimuthal angles which resulted in higher pressures along the larger azimuths.

4.4.4 Pressure Contours

A contour plot of the pressure data is shown in figure 52. The contours revealed the steep adverse pressure gradient in the streamwise direction along $\phi = 0°$. There was also a steep streamwise pressure gradient in the region between $\phi = 150°$ and $\phi = 180°$ on the cylinder. The transverse pressure gradients became apparent in the plots around $\phi = 15°$ and remained significant all the way to $\phi = 150°$. The direction of the maximum pressure gradient appeared to be normal to the cylinder-flare junction. The plateau regions shown in the individual distributions are evident in the contour plot downstream of the initial pressure rise and upstream of the cylinder-flare junction from $\phi = 30°$ to $\phi = 180°$. The wavy contour line in the region near the cylinder-flare junction was due to the disparity of the amount of data taken in the transverse direction as compared to the streamwise direction and was an artifact of the contour calculation. The same contour plot is shown in figure 53 overlaid with the interpretation from the oil-flow visualization results.

4.4.5 Comparison with 2-D Data

A comparison of the present data along the $\phi = 0°$ line of symmetry to unpublished results obtained from a 20° half-angle axisymmetric flare in the same wind tunnel under the same conditions revealed only some minor differences (fig. 54). Lower free-stream pressures for the 2-D case were thought to be a consequence of the flare being located on the cylinder farther downstream than the 3-D flare since the pressure measurements along the cylinder demonstrated the general trend of decreasing pressures in the downstream direction. The upstream influence for the 2-D case was found to be 0.79 cm whereas for the 3-D case the upstream influence along the line of symmetry was found to be 0.54 cm. The difference is attributed to the 3-D nature of the flow in this study. Avduyevskii and Medvedev (ref. 55) found for 3-D flows that the upstream influence along the line of symmetry was smaller due to the transverse pressure gradients. This transverse pressure gradient on either side of the line of symmetry sweeps the low-momentum fluid away which decreases the upstream effect. The ratio of the peak pressure to the free-stream pressure for the 2-D case was slightly higher than the 3-D pressure-rise ratio. This was a consequence of the fluid being swept away for the 3-D case along $\phi = 0°$ which thinned the boundary layer.

4.5 Skin Friction

4.5.1 Measurements in Undisturbed Boundary Layer

The LISF instrument was initially used during this study to perform measurements on the cylinder upstream of the interaction. The purposes of these initial measurements were to make refinements to the hardware, to verify the software, to develop an operating procedure, and to gain experience in operating the LISF instrument. Another important item that was investigated during this check-out phase was the effect that the type of test surface had on the LISF results.

The test surface needs to produce specular light reflection which may involve either polishing the surface, utilizing a glass insert, or applying some type of coating to the model surface. One test surface examined in this study consisted of a small polished section of the stainless steel cylinder. A second surface was an adhesive-backed clear plastic. Prior to the application of the clear plastic to the cylinder, extra precautions were taken to minimize the specular reflections from the cylinder surface beneath the plastic. This included either spray painting the cylinder surface black, or adhering a piece of MonoKote to the cylinder surface prior to the application of the clear plastic. The results of measurements performed on these different surfaces are presented in table 28. The results from a second beam 5.2 mm downstream of the primary measurement beam are also included in table 28.

The average value of the skin-friction coefficient from measurements performed between $x = -5.5$ cm and $x = -2.0$ cm on the clear plastic with MonoKote ($C_{fx} = 0.00161 \pm 2.0\%$) and with the cylinder painted black ($C_{fx} = 0.00155 \pm 6.9\%$) were within 4% of each other. The average value of the skin-friction coefficient from measurements performed on the polished stainless steel ($C_{fx} = 0.00171 \pm 1.9\%$) was 6% higher than the measurements on the clear plastic with MonoKote and was 10% higher than the measurements on the clear plastic with the painted surface. From this

limited number of samples, the skin friction as indicated by the system appeared to be slightly sensitive to the particular surface on which the measurements were performed.

Besides the fact that only a limited number of samples were acquired, there are some other possible explanations for these discrepancies. First, signals from measurements performed on the polished stainless steel were of lower visibility as compared to the other two surfaces. The average signal visibility from the polished stainless steel was around 25%. The lower visibility was attributed to the higher reflectivity off the oil-stainless steel interface as compared to the oil-plastic interface. For runs utilizing the stainless steel surface, an extra filter was used to decrease the intensity of the reflected beams prior to detection by the photodiode. The visibility of the signal from both the clear plastic with MonoKote and the clear plastic with the painted cylinder was around 60%. Typical signals from these three surfaces are shown in figures 55 through 57. The zero level of the ordinate in the plots is the actual zero voltage level. The higher the visibility of the signal, the more consistent were the fringe-time products within the run for each possible combination of fringes. Second, the runs with the cylinder surface painted black with clear plastic on top were conducted during the early part of the investigation. At such time, as previously mentioned, emphasis was not solely on the acquisition of an accurate skin-friction measurement. In addition, emphasis was placed on the actual operation of the tunnel and in bringing the tunnel to operating conditions as quickly as possible with existing controls. All of this may have impacted those early measurements. The LISF measurements in the undisturbed boundary layer are shown in figure 58. The value of the skin-friction measurements, as measured by the LISF technique, decreased in the downstream direction more than what would be expected. The explanation for this behavior is not known.

To assess the accuracy of the LISF measurements, a comparison was made to results from other recognized techniques. There are instruments that are known to accurately measure the shear stress at the wall in boundary layers free of pressure and shear gradient effects. However, such instruments were not available. Thus, other standards for comparison were pursued. Similarity techniques can be used to deduce the skin friction from experimental mean-velocity profiles. One of these techniques was employed to deduce the skin friction from the LDV mean-velocity data as described in section 5.3. The results are shown in figure 58. The mean of the deduced skin-friction results, between $x = -2.0$ cm and $x = 1.0$ cm, was $C_{fx} = 0.00144$ ($\pm 1.6\%$). The mean skin-friction coefficient from the LISF measurements performed in that same region was $C_{fx} = 0.00149$ ($\pm 5.1\%$) which was 3% higher than the deduced value. A second standard with which the LISF mean result was compared was the Van Driest II theory (ref. 56) derived for a flat-plate flow. The theory predicted a skin-friction coefficient of $C_{fx} = 0.00156$. In this case, the LISF value of $C_{fx} = 0.00149$ was lower by some 5%. Since the value of the LISF result was between the two selected standards, it provided sufficient confidence that the LISF result in the undisturbed boundary layer was accurate. Kim, Lee, and Settles (ref. 57) also made a comparison of LISF measurements with other skin friction techniques and concluded that the LISF is more accurate than other present methods with an accuracy of $\pm 6\%$. The present results appear to be consistent with this accuracy estimate for the LISF instrument.

4.5.2 Corrections

The correction factor based on the effects of pressure gradient and gravity was computed for each LISF measurement according to equation 4-32. A representative value for the streamwise and transverse pressure gradients at each measurement location was obtained from interpolations of surface

43

pressure measurements. The results of the correction parameter calculations are shown in figure 59 for all three azimuths. For the skin-friction data along $\phi = 0°$, all corrections were less than 1%, with the largest correction occurring at the first measurement location downstream of attachment. For streamwise measurements along $\phi = 90°$, two measurement locations within the separated region on the cylinder possessed correction values of approximately 1%. The correction equation was also applied to the transverse measurements along $\phi = 90°$. Although not as significant as the transverse pressure gradient, the effect of gravity also had to be included for the transverse measurements. Even with these two effects combined, the correction was less than 1% for all measurements in the transverse direction.

Along $\phi = 180°$, the largest correction factor for all of the LISF measurements was computed for the first measurement location downstream of separation. At this location the skin friction was small and the pressure gradient was relatively large, the combination of which called for a 4% correction. The measurement location just upstream of attachment yielded the second highest value for the correction of 2.5%. Overall, in light of the small values of the correction factor, the data presented in this section were not adjusted according to these correction results.

For LISF measurements within regions of large shear-stress gradients, Tanner (ref. 58) derived a correction to account for the gradient between the oil leading edge and the location of the measurement beam. Simply, his theory states that during analysis of the data the shear stress is computed based on an adjusted separation distance between the oil leading edge and the measurement beam. The adjusted distance to be used should be 75% of the actual distance. For the present data, the average distance between the leading edge and the measurement beam was 2.2 mm. In light of the close proximity of the measurement location to the oil leading edge, the data were not corrected for the effects of shear-stress gradient.

4.5.3 Measurements along $\phi = 0°$

The pressure distribution for $\phi = 0°$ (fig. 60) given in table 29 was obtained when this azimuthal plane was aligned with the side of the cylinder. This particular distribution is different from the $\phi = 0°$ distribution shown in figure 36 which was obtained when the $\phi = 0°$ plane was located on top of the cylinder. One obvious difference between the two distributions is the pressure spike near the aft end of the flare ramp in figure 60. This pressure spike indicated the presence of an extraneous shock wave which either originated or was reflected from the tunnel side wall. Recall that the test section was 38.1 cm high and 25.4 cm wide. Thus, the azimuth along the flare was closer to the side wall when aligned with the side of the cylinder as compared to the top wall when aligned on top of the cylinder.

The LISF results along $\phi = 0°$ are presented in table 30 and plotted in figure 60. As the boundary layer initially experienced the streamwise adverse pressure gradient, the mean flow near the wall was retarded which resulted in a decrease of the skin friction. The data in the upstream influence region illustrated the sharp decline in skin friction ahead of separation. It is recognized that caution should be used when performing and interpreting LISF measurements close to the separation line. This line acts as an oil accumulation line which could, due to a buildup of oil, influence LISF measurements in that vicinity. However, in contrast to a 2-D case, the present 3-D case was not geometrically constrained so that the oil may have not been subject to significant buildup since it could flow along the oil accumulation line down the side of the model.

The oil flow visualizations revealed the existence of a singular point at the intersection of the separation line and the $\phi = 0°$ azimuth; thus, by definition, the skin friction will be zero at that point. A linear extrapolation of the skin-friction data upstream of separation down to the zero skin-friction level indicated that separation occurred in the vicinity of $x_s = -0.27$ cm. This extrapolated location was comparable to the separation location as revealed by the surface oil flow visualization technique which was estimated to be at $x_s = -0.30$ cm. Obviously, these two techniques are very similar since they rely on the flow of oil on the surface and should, therefore, give consistent results.

Along this same line of symmetry, the value of skin friction would be negative in the separated region since the oil flow visualizations revealed that the flow direction was opposite to the free-stream direction. Although the LISF is a point measurement technique, a finite distance is required between the measurement beam and the oil leading edge. As such, the approximately 3 mm distance between the separation line and cylinder-flare junction along $\phi = 0°$ was too restrictive so that no LISF measurements were attempted within the separated region along this azimuth. Dashed lines in figure 60 indicate the expected distribution just upstream of separation and downstream of reattachment.

In preparation for performing LISF measurements, the flare was spray painted black and the adhesive-backed clear plastic was applied. The taps in the flare along the $\phi = 0°$ azimuth were protected from the paint by masking off the immediate area around each tap. In order to avoid extra reflections off the surface near the taps or the taps themselves, the flare was rotated 2.5° and skin-friction measurements were made along this $\phi = 2.5°$ line. From the oil flow visualization results, the flow along $\phi = 2.5°$ did not diverge significantly from the $\phi = 0°$ azimuth. Hence, the results along this $\phi = 2.5°$ azimuth were considered comparable to the values along the line of symmetry and are reported as such. A slight rotation was also needed for measurements along $\phi = 180°$, but no rotation was necessary for measurements along $\phi = 90°$.

The most upstream measurement location on the ramp along $\phi = 0°$ yielded an average skin-friction coefficient of $C_{fx} = 0.00155$. Much like the region near separation, extreme care must be exercised when performing and interpreting LISF measurements near attachment. This first measurement location was downstream of attachment and illustrated that the skin friction had increased significantly between the anticipated negative values in the separated region to a level comparable to the undisturbed value in a short distance. In contrast to a 2-D separation bubble, 3-D separation can entrain fluid. As the flow proceeded over the separated region, the lower-momentum fluid of the boundary layer was entrained. Thus, the flow that attached consisted of only the outer, more energetic fluid of the original boundary layer which immediately imposed a steep velocity gradient at the surface. Further, as a result of the interaction, the increased turbulent activity led to increased mixing. This accelerated the lower portion of the redeveloping boundary layer and increased the velocity gradient.

The increased turbulent activity was partially a consequence of the passage of the boundary layer through the shock discontinuity. The adverse pressure gradient caused compression which also increased the turbulent activity through the extra strain rate $(\frac{\partial U}{\partial x})$. For the flow along the ramp, the concave curvature had a destabilizing effect on the turbulence, which further increased the turbulent activity. The pressure reached a peak plateau near $x = 2.85$ cm. The skin friction continued to increase beyond that point and eventually reached a plateau near $x = 5.17$ cm. The overall pressure-rise ratio along the $\phi = 0°$ azimuth was equal to 2.62. The overall rise in the skin-friction coefficient along this same azimuth was 2.25. The value of the skin friction in the peak pressure plateau region was $C_{fx} = 0.00335$

which amounted to an increase of 125% over the incoming level prior to the interaction. Thus, one effect of the interaction was a doubling of the local skin friction along this azimuth.

The spike in the skin-friction distribution towards the aft end of the flare was a consequence of an extraneous shock wave. The pressure measurements first indicated the influence of the extraneous shock from the tunnel wall near $x = 6.5$ cm. The shear stress measurement at $x = 6.9$ cm, which was experiencing the effects of the adverse pressure gradient of the disturbance, showed a slight decline as would be expected. The next skin-friction measurement location was in the vicinity of the maximum indicated pressure and resulted in the largest reading of the skin friction for the entire interaction of $C_{fx} = 0.00420$ ($\tau_x = 135.8$ N/m^2). A skin friction spike near a shock impingement location was also observed by Murthy and Rose (ref. 59) using buried wire gauges. The remaining shear-stress measurements along the flare downstream of the maximum pressure spike indicated a relaxation to a value comparable to the peak skin-friction plateau level on the flare upstream of the extraneous pressure perturbation.

The skin friction dropped dramatically along $\phi = 0°$ after the ramp-afterbody corner. Convex curvature had a stabilizing effect on the turbulence which contributed to a decrease in the turbulent activity. The skin friction experienced a slight dip along the afterbody and then increased to a level which was 6% lower than the level upstream of the interaction.

Along the $\phi = 0°$ azimuth, at least two LISF samples were acquired at each measurement location along the ramp of the flare except for the last two locations. Only one sample was acquired at these latter points which were downstream of the effects of the extraneous shock emanating from the side wall. The repeatability of the two samples at each location was typically within 5%. There does not exist a standard to which the present skin-friction measurements within the interaction region can be compared. This actually points out the advantage of the LISF technique as being applicable to complex flows where other methods are not accurate or easily applied.

4.5.4 Measurements along $\phi = 90°$

The pressure distribution for $\phi = 90°$ along the side of the model is given in table 31 and the streamwise skin-friction data is given in table 32. Both distributions are plotted in figure 61. In the upstream influence region, the streamwise skin friction was not only affected by the streamwise adverse pressure gradient, but also by the transverse pressure gradient. The initial streamwise pressure gradient along $\phi = 90°$ prior to separation was not as large as it was along $\phi = 0°$. On the other hand, the transverse pressure gradient was equal to zero along the lines of symmetry whereas for $\phi = 90°$ the transverse pressure gradient was significant. The upstream influence was first indicated by oil flow visualization to have occurred along $\phi = 90°$ at $x_u = 1.84$ cm. The distribution in figure 61 demonstrated that the skin friction dropped rapidly from the undisturbed level to the level at the first measurement location within the interaction region. It was not possible to distinguish the separate effects of the streamwise pressure gradient and the transverse pressure gradient on the skin friction. The streamwise skin friction then leveled out just prior to separation and maintained a slightly decreasing trend to a location just inside separation. Recall that for 3-D separation, the skin friction is equal to zero only along the direction normal to the separation line and separation does not imply that the streamwise skin friction should be negative. This is true for the data along $\phi = 90°$ where the streamwise skin friction, C_{fx}, remained positive even in the separated region. The oil flow visualizations indicated that

46

the separation line was at $x_s = 2.50$ cm. The streamwise skin friction near separation was estimated to be $C_{fx} = 0.00080$.

Toward the middle of the separated region on the cylinder, the skin friction distribution reached a minimum at $x = 3.85$ cm. Between $x = 3.75$ cm and $x = 4.00$ cm, the pressure in the streamwise direction was almost constant increasing by only 0.4%. No measurements could be attempted between $x = 3.85$ cm which was on the cylinder and $x = 5.00$ cm on the flare due to the geometry of the model. The two measurement locations on the flare within the separated region indicated a sharp increase in skin friction. The streamwise skin friction was higher in the vicinity of attachment than it was near separation. The attachment was located on the flare near $x_a = 5.25$ cm as indicated by oil flow visualizations. The region just downstream of attachment was subject to large flow turning as the perturbed flow began relaxing back toward the conical flow direction. The streamwise skin friction reached a peak near $x = 10.0$ cm which was just downstream of the streamwise peak pressure plateau. The peak value for the skin-friction coefficient along $\phi = 90°$ was $C_{fx} = 0.00220$ and was an increase of 48% over the undisturbed level.

The skin friction dropped dramatically after the expansion corner. The skin-friction distribution along the afterbody initially dropped and then increased again. This dip was also evident along $\phi = 0°$. The representative value of skin friction along $\phi = 90°$ on the afterbody was slightly more than half the value along $\phi = 0°$ even though the pressure level was the same for both.

The values for the component of skin friction in the transverse direction, shown in figure 61, were resolved from the streamwise LISF measurements and the flow-angle data from oil flow visualization. The resolved transverse data are summarized in table 33. As a result of the transverse pressure gradient, the flow in the upstream influence region along $\phi = 90°$ immediately began turning away from the free-stream direction. The skin-friction coefficient in the transverse direction increased from zero in the undisturbed boundary layer to a value of $C_{fz} = 0.00068$ at $x = 2.25$ cm. The transverse skin-friction coefficient reached a relative maximum at $x = 3.00$ cm, 0.50 cm downstream of separation. The transverse skin friction reached another maximum just upstream of attachment. Downstream of attachment, the transverse distribution demonstrated the turning of the flow toward the conical direction. LISF measurements in the transverse direction were performed at six different locations upstream and within the separated region as given in table 34. These particular measurements were in good agreement with the resolved values. The maximum flow-turning angle with respect to the free-stream direction was determined from the oil flow visualization to be 50° at $x = 3.85$ cm.

4.5.5 Measurements along $\phi = 180°$

The pressure distribution for $\phi = 180°$ along the side of the model (fig. 62) is given in table 35. The streamwise skin-friction data along $\phi = 180°$ is summarized in table 36 and is shown in figure 62. The initial effects of the interaction along the $\phi = 180°$ azimuth are evidenced by a drop in skin friction just upstream of $x = 4.5$ cm. Within the separated region, the flow direction along the $\phi = 180°$ line of symmetry was opposite to the free-stream direction. Skin-friction measurements were performed at five locations within the separated region as indicated by the negative values of skin friction in figure 62. Four of the measurement locations were on the cylinder and one was on the flare. The largest absolute magnitude measurement was $|C_{fx}| = 0.00043$, which was 29% of the undisturbed value. These

measurements within the separated region are of particular importance since accurate skin-friction data in separated flows are scarce.

A saddle of separation (S4) existed along $\phi = 180°$ from which the separation line perpendicular to the oncoming flow emanated. Interpolation between the skin-friction measurements upstream and downstream of separation gave the location of separation at $x_s = 5.20$ cm. The pressure measurements indicated that separation was at $x_s = 5.25$ cm while the oil flow visualization results indicated separation was located at $x_s = 5.00$ cm. Interpolation of the skin-friction data near attachment indicated its location to be at $x_a = 7.80$ cm which coincided with the attachment location as determined from oil flow visualization records. The pressure distribution reached a peak plateau at $x = 9.25$ cm. The maximum skin-friction coefficient of $C_{fx} = 0.00203$ was reached at the most downstream measurement location on the ramp, but the skin-friction distribution appeared to have still been increasing. This value was 41% larger than the undisturbed level. The peak level along $\phi = 180°$ was much lower than the peak level along $\phi = 0°$ partially as a consequence of the thicker boundary layer that existed along $\phi = 180°$. Additional features such as the two vortices also had an impact on the flow along $\phi = 180°$. According to the pressure measurements, a weak extraneous shock wave impinged upon the aft end of the flare resulting in a jump in the skin-friction measurements.

On the afterbody, the most upstream measurement location yielded a skin friction slightly higher than the incoming level. The skin friction decreased and appeared to approach a minimum near the farthest aft measurement location where the skin-friction coefficient was $C_{fx} = 0.00110$. The skin-friction measurements did not indicate the presence of an extraneous shock as the pressure measurements did on the afterbody.

4.5.6 Comparison of Measurements along $\phi = 0°$, $90°$, and $180°$

The streamwise skin-friction distributions from the three azimuths are shown together in figure 63. The degree of concave curvature was the same around the entire model, yet the differences in the skin-friction distributions point out the different local interactions that the flow along the three azimuths encountered. The flow along $\phi = 0°$ encountered a rather small separated region. The flow along $\phi = 90°$ encountered separation under highly swept conditions. The flow along $\phi = 180°$ encountered a larger separated region resulting from the interference of two approaching vortices near the line of symmetry. The interaction of this type is not yet well understood but offers some similarities to the crossing SW/BLI caused by dual fins. The skin friction attained the highest steady level along $\phi = 0°$. Although the boundary layer was thicker along $\phi = 180°$ as compared to $\phi = 90°$, the peak skin-friction values were approximately the same. This probably indicates that the turbulent activity was more intense along $\phi = 180°$.

The three skin-friction distributions are shown in figure 64 with the abscissa shifted so that the locations of the cylinder-flare junctions are coincident. The extent of upstream influence is evident in the figure. The skin-friction gradient after attachment was steepest for $\phi = 0°$. The saddle-of-separation to node-of-attachment combination along $\phi = 0°$ indicated that there was separation which spiraled into a vortex which could entrain the low-momentum fluid of the flow that passed over the separated region. In contrast, the saddle-of-separation to saddle-of-attachment combination along $\phi = 180°$, although difficult to interpret, clearly indicated a different type of interaction. One possible flow structure along the $\phi = 180°$ azimuth would include a single streamline connecting the two saddle points. For such a

48

case, the lower-momentum fluid that passed over the separated region would not get entrained resulting in a lower skin friction after attachment. Overall, the effect of the 3-D SW/BLI and consequent separation was a significant increase in the drag of the model along $\phi = 0°$ and, to a lesser extent, an increase in drag along $\phi = 90°$ and $\phi = 180°$.

5 CONCLUSIONS

1. An experimental study was conducted on the interaction of a supersonic, turbulent boundary layer flowing over an axisymmetric cylinder as it encountered a 3-D offset conical flare. The flow field included a generated shock system and 3-D separation with significant cross flow. The shock system was found to be steady which is important to turbulence modeling efforts. The flare ramp was of sufficient length to allow the boundary layer to relax after the shock interaction. Although of lesser interest, an afterbody section provided an expansion corner and further relaxation. The interaction is representative of practical interactions occurring on supersonic aircraft at any corner or wing- and fin-body junctions.

2. Oil flow visualizations were successful in revealing many details of the surface flow topology. Separation lines proceeding from saddles of separation along $\phi = 0°$ and $\phi = 180°$ were visible, each of which terminated into different foci of separation. Another saddle of separation was identified interspersed between these two foci. A saddle of attachment was formed at the intersection of the attachment line, which was visible along the flare, and the $\phi = 180°$ line of symmetry. This saddle was directly connected to the saddle of separation along $\phi = 180°$ as a result of the strong symmetry of the flow. The surface topology documentation is important since CFD validation must be qualitatively correct before it can be expected to be quantitatively correct.

3. The laser light sheet study complemented the surface topology study even though it did not yield detailed information of the flow field away from the surface. Near the flare along $\phi = 180°$, a unique image was recorded. Although not directly visualized, the general location of the two main vortices could be deduced from these images. The results were consistent with the postulated flow structure.

4. The HRC-1 LDV system, operated with both two and three channels, provided mean and fluctuating velocity data within the undisturbed boundary layer. The mean velocity profiles were analyzed to deduce an average value for the skin-friction coefficient of 0.00144. The velocity data will supply approach boundary-layer conditions for subsequent computations.

5. The pressure documentation over the 3-D interaction was extensive. Surface pressures were acquired every 15° around the circumference of the cylinder, flare ramp, and afterbody. The stream-wise distributions provided the location of upstream influence and separation. Together the distributions indicated the degree of transverse pressure gradient. The pressure data in the interaction itself and down-stream, where the outgoing boundary layer relaxes, will serve as a check on the predictive capabilities of CFD codes and turbulence models.

6. The application of the LISF technique to the flow was significant in many respects. It was used to obtain skin-friction data in a compressible flow contributing to the experience of applying the technique to such flows. Although the nature and the complexity of the present 3-D SW/BLI with the associated large pressure and shear gradients limits the capability and accuracy of other skin-friction measurement techniques, the LISF instrument performed measurements with good repeatability. The technique was applied to highly 3-D regions, and measurements were performed within the separated region which is especially crucial due to the scarcity of skin-friction data in such regions.

7. A new surface preparation technique for LISF measurements was implemented which involved adhering a clear plastic to the model. The visibility of the LISF signals, while utilizing this surface, was

50

60%. This surface preparation technique was quick, simple, and versatile so that LISF measurements could be performed on any type or shape of model without the need for polishing or glass inserts.

8. The LISF instrument measured a skin-friction coefficient of $C_{f_x} = 0.00149$ ($\pm 5.1\%$) upstream of the interaction. The measured value was 3% higher than the mean value deduced from the mean-velocity data and 5% lower than the value predicted by the Van Driest II theory. The close agreement provided assurance of the accuracy of the LISF measurements. The largest source of the uncertainty in the LISF results was the measurement of the surface temperature.

9. The skin-friction measurements along $\phi = 0°$ downstream of attachment demonstrated an increase of 125% over the undisturbed upstream boundary-layer value. The increase was higher along $\phi = 0°$ than along the other two azimuths. Documentation of the 3-D flow along $\phi = 90°$ included LISF measurements in the streamwise direction. Values for the skin friction in the transverse direction were resolved from streamwise LISF measurements and flow-angle data. The resolved data were in close agreement with a limited number of LISF measurements in the transverse direction. Within the separated region along $\phi = 180°$, where the flow was opposite to the free-stream direction, the maximum absolute value of the skin friction reached a value that was 29% of the undisturbed skin-friction level.

10. Frequently, only pressure measurements are available from SW/BLI experiments to validate computations. Skin-friction measurements, however, offer a more challenging test for computations since skin friction addresses more directly the accuracy of how the viscous stresses are modeled. Thus, the skin-friction measurements should significantly enhance the value of this study as a building block experiment for 3-D turbulence modeling and for CFD verification.

APPENDIX

LISF UNCERTAINTY ANALYSIS

The goal of this appendix is to examine the uncertainty in the skin-friction measurements. In general, in order to obtain reliable estimates of standard deviation and other statistical information, numerous samples are required. However, it was not possible to acquire numerous samples at each measurement location in the present study because of several factors. First, the LISF technique is capable of only point measurements requiring a single tunnel blow for each measurement location. Second, the blow-down facility was limited to a maximum of six runs per day which, combined with a time constraint on the study, imposed a limit on the number of possible LISF tunnel runs. Third, the 3-D interaction required more measurement locations to adequately document the flow as compared to a simpler 2-D interaction. Some repeat measurements were performed in certain regions such as in the undisturbed boundary layer, on the ramp along $\phi = 0°$, and in the separated zone along $\phi = 90°$ and $\phi = 180°$. The repeatability of these measurements is alluded to in the text.

For locations in which there were a limited number of samples, an estimate of the uncertainty can be obtained based on the uncertainties in the primary measurements. The LISF instrument does not directly measure skin friction; instead, the skin friction is determined quasi-directly by measuring the time variation of the oil thickness. Other pertinent measurements include the surface temperature, the distance between the oil leading edge and the measurement beam, the beam incidence angle, the total pressure, and the total temperature.

Consider the situation where a dependant variable, $R(x_1, ..., x_n)$, is obtained from measurements of a number of independent quantities, $x_1, ..., x_n$. According to Holman (ref. 42), the uncertainty of the calculated result, Δ_R, can be estimated from the uncertainty of the primary measured quantities, $\Delta_1, , ..., \Delta_n$, by

$$\Delta_R = \left[\left(\frac{\partial R}{\partial x_1} \Delta_1 \right)^2 + ... + \left(\frac{\partial R}{\partial x_n} \Delta_n \right)^2 \right]^{1/2} \tag{A-1}$$

The skin-friction coefficient in terms of the primary measured quantities is given by

$$C_f = \left[\frac{2n_0 \mu_0 x \cos \theta_t}{\lambda N t} \right] / \left(\frac{1}{2} \rho_\infty U_\infty^2 \right) \tag{A-2}$$

Combining equations A-1 and A-2, along with some rearrangement, results in

$$(\Delta C_f / C_f) = \left[\left(\Delta N t / N t \right)^2 + ... + \left(2 \Delta U_\infty / U_\infty \right)^2 \right] \tag{A-3}$$

Table 37 gives measurements from one particular run to illustrate this uncertainty analysis. The measurement location was within the undisturbed boundary layer. The values from pertinent quantities that were calculated using these measurements are included. Listed in the right hand column is the contribution of these terms to the uncertainty of the skin-friction result as computed from equation A-3. The uncertainty of the skin friction is found by taking the square root of the sum of this column.

52

The right hand column of Table 37 points out the critical measurements. Clearly, the uncertainty associated with the viscosity of the oil was the most significant contribution to the uncertainty of the skin-friction result. The uncertainty of the oil viscosity is influenced by the knowledge of the actual viscosity and the surface temperature. The manufacturer specifies an uncertainty of the oil viscosity as ±5%. However, this value was decreased by having an independent laboratory measure the viscosity at different temperatures. If the actual temperature is known, the curvefit to the data resulted in an uncertainty in the viscosity of only ±1%. The reason, then, for the relatively high uncertainty for the viscosity is due to the uncertainty of the measurement of the surface temperature.

Next in terms of significance was the uncertainty in determining the fringe-time product, Nt. This product was determined from the fringe record as outlined in section 4.4. The quality of the fringe record was mainly dependent upon the signal visibility and surface waves. The results indicated the trend that the higher the visibility, the more consistent was the Nt product. Surface waves limited the number of available fringes on which to perform the analysis. The uncertainty of the Nt product was determined by performing statistical analysis on the Nt results from all the different possible fringe combinations.

In nondimensionalizing the shear stress at the wall, the free-stream density and velocity were computed based on the measurement of total pressure and total temperature. The Mach number was assumed to be $M = 2.89$. The uncertainty in knowing the total temperature did have a slight impact on the skin-friction result through the free-stream velocity term. The relatively low uncertainty in the total pressure measurement had very little impact on the uncertainties of the free-stream density and, consequently, on the resulting skin friction. The accurate measurement of the beam leading edge is important, but due to the motion control system used, the uncertainty of this measurement was low leading to a small effect on the uncertainty of skin-friction. The beam incidence angle measurement did possess a relatively high uncertainty, but the effect upon the uncertainty of skin-friction was negligible since the angle was near normal.

Based on the above analysis, the skin-friction for this particular run can be expressed along with the uncertainty as

$$C_f = 0.00146 \pm 0.00011 (\pm 7.7\%) \qquad \text{(A-4)}$$

Accurate measurement of the surface temperature was obviously very important for the present work.

REFERENCES

1. Wideman, Jeffrey K.; Brown, James L.; Miles, John B.; and Özcan, Oktay: Skin-Friction Measurements in a 3-D, Shock-Wave/Boundary-Layer Interaction. AIAA Paper 94-0314, 32nd Aerospace Sciences Meeting, Reno, Nev., Jan. 1994.

2. Brown, J. L.; Kussoy, M. I.; and Coakley, T. J.: Turbulent Properties of An Axisymmetric Shock-Wave/Boundary-Layer Interaction Flow. IUTAM Symposium, Paris, France, Sept. 1985; also in: Turbulent Shear Layer/Shock-Wave Interactions, J. Delery, ed., Springer-Verlag, Berlin, 1986, pp. 137–148.

3. Dunagan, S.; Brown, J. L.; and Miles, J. B.: Interferometric Data for a Shock-Wave/Boundary-Layer Interaction. NASA TM-88227, Sept. 1986.

4. Dunagan, S.; Brown, J. L.; and Miles, J. B.: A Holographic Interferometry Study of an Axisymmetric Shock-Wave/Boundary-Layer Strong Interaction Flow. AIAA Journal, vol. 25, no. 2, Feb. 1987, pp. 294–299.

5. Kussoy, M. I.; Brown, J. D.; Brown, J. L.; Lockman, W. K.; and Horstman, C. C.: Fluctuations and Massive Separation in Three-Dimensional Shock-Wave/Boundary-Layer Interactions. 2nd International Symposium on Transport Phenomena in Turbulent Flows, Tokyo, Japan, Oct. 1987.

6. Brown, J. D.; Brown, J. L.; Kussoy, M. I.; Holt, M.; and Horstman, C. C.: Two-Component LDV Investigation of 3-Dimensional Shock/Turbulent Boundary Layer Interactions. AIAA Journal, vol. 26, no. 1, Jan. 1988, pp. 52–56.

7. Brown, J. D.; Brown, J. L.; and Kussoy, M. I.: A Documentation of Two- and Three-Dimensional Shock-Separated Turbulent Boundary Layers. NASA TM-101008, July 1988.

8. Brown, James L.: Geometric Bias and Time Coincidence in 3D Laser Doppler Velocimeter Systems. Experiments in Fluids Journal, vol. 7, 1989, pp. 25–32.

9. Brown, James L.; and Özcan, O.: A 3D Laser Velocimeter for Supersonic Turbulent Flows. Measurement and Instrumentation Workshop, Ames Research Center, July 25–27, 1989.

10. Řezníček, R.: Surface Tracing Methods. Handbook of Flow Visualization. Yang, W.-J., ed., Hemisphere Pub. Corp., 1989, pp. 91–103.

11. Coles, D. E.: The Law of the Wall in the Turbulent Boundary Layer. Journal of Fluid Mechanics, vol. 1, pt. 2, July 1956, pp. 191–226.

12. Van Driest, E. R.: Turbulent Boundary Layer in Compressible Fluids. Journal of the Aeronautical Sciences, vol. 18, no. 3, 1951, pp. 145–160.

13. Maise, G. M.; and McDonald, H.: Mixing Length and Kinematic Eddy Viscosity in a Compressible Boundary Layer. AIAA Journal, vol. 6, no. 1, 1968, pp. 73–80.

14. Matthews, D. C.; Childs, M. E.; and Paynter, G. C.: Use of Coles' Universal Wake Function for Compressible Turbulent Boundary Layers. Journal of Aircraft, vol. 7, no. 2, 1970, pp. 137–141.

15. Sun, C.-C.; and Childs, M. E.: A Modified Wall Wake Velocity Profile for Turbulent Compressible Boundary Layers. Journal of Aircraft, vol. 10, no. 6, 1973, pp. 381–383.

16. Sun, C.-C.; and Childs, M. E.: Flowfield Analysis for Successive Oblique Shock Wave-Turbulent Boundary Layer Interactions. NASA CR-2656, 1976.

17. Olsen, M. E.; and Seegmiller, H. L.: Low Aspect Ratio Wing Code Validation Experiment. AIAA Journal, vol. 31, no. 10, 1993, pp. 1744–1752.

18. Tanner, L. H.; and Blows, L. G.: A Study of the Motion of Oil Films on Surfaces in Air Flow, with Application to the Measurement of Skin Friction. Journal of Physics E: Scientific Instruments, vol. 9, no. 3, 1976, pp. 194–202.

19. Tanner, L. H.; and Kulkarni, V. G.: The Viscosity Balance Method of Skin Friction Measurement: Further Developments Including Application to Three-Dimensional Flow. Journal of Physics E: Scientific Instruments, vol. 9, no. 9, 1976, pp. 1114–1121.

20. Tanner, L. H.: A Skin Friction Meter Using the Viscosity Balance Principle, Suitable for Use with Flat or Curved Metal Surfaces. Journal of Physics E: Scientific Instruments, vol. 10, no. 3, 1977, pp. 278–284.

21. Tanner, L. H.: A Comparison of the Viscosity Balance and Preston Tube Methods of Skin Friction Measurement. Journal of Physics E: Scientific Instruments, vol. 10, no. 6, 1977, pp. 627–632.

22. Monson D. J.; and Higuchi, H.: Skin Friction Measurements by a Dual-Laser-Beam Interferometer Technique. AIAA Journal, vol. 19, no. 6, 1981, pp. 739–744.

23. Monson, D. J.; Driver, D. M.; and Szodruch, J.: Application of a Laser Interferometer Skin-Friction Meter in Complex Flows. Proceedings of the International Congress on Instrumentation in Aerospace Simulation Facilities, 1981, pp. 232–243.

24. Monson, D. J.: A Laser Interferometer for Measuring Skin Friction in Three-Dimensional Flows. AIAA Paper 83-0385, 1983.

25. Westphal, R. V.; Bachalo, W. D.; and Houser, M. H.: Improved Skin Friction Interferometer. NASA TM-88216, 1986.

26. Settles, G. S.: Recent Skin Friction Techniques for Compressible Flows. AIAA Paper 86-1099, 1986.

27. Kim, K.-S.: Skin Friction Measurements by Laser Interferometry in Supersonic Flows. Ph.D. Thesis, Pennsylvania State University, 1989.

28. Kim, K.-S.; and Settles, G. S.: Skin Friction Measurements by Laser Interferometry in Swept Shock Wave/Turbulent Boundary-Layer Interactions. AIAA Journal, vol. 28, no. 1, 1990, pp. 133–139.

29. Kim, K.-S.; Lee, Y.; Alvi, F. S.; Settles, G. S.; and Horstman, C. C.: Laser Skin Friction Measurements and CFD Comparison of Weak-to-Strong Swept Shock/Boundary-Layer Interactions. AIAA Paper 90-0378, 1990.

30. Seto, J.; and Hornung, H.: Internally Mounted Thin-Liquid-Film Skin-Friction Meter—Comparison with Floating Element Method With and Without Pressure Gradient. AIAA Paper 91-0060, 1991.

31. Seto, J.; and Hornung, H.: Two-Directional Skin Friction Measurement Utilizing a Compact Internally-Mounted Thin-Liquid-Film Skin Friction Meter. AIAA Paper 93-0180, 1993.

32. Bandyopadhyay, P. R.; and Weinstein, L. M.: A Reflection-Type Oil-Film Skin-Friction Meter. Experiments in Fluids, vol. 11, 1991, pp. 281–292.

33. Knight, D. D.; Horstman, C. C.; and Monson, D. J.: The Hypersonic Shock Wave-Turbulent Boundary Layer Interaction Generated by a Sharp Fin at Mach 8.2. AIAA Paper 92-0747, 1992.

34. Hubner, J. P.; and Carroll, B. F.: Thin-Oil-Film Interferometric Skin-Friction Measurements in Short-Duration Supersonic Flow. Experiments in Fluids, vol. 15, 1993, pp. 315–322.

35. Monson, D. J.; Mateer, G. G.; and Menter, F. R.: Boundary-Layer Transition and Global Skin Friction Measurement with an Oil-Fringe Imaging Technique. SAE Paper 932550, Aerotech '93, 1993.

36. Monson, D. J.: A Nonintrusive Laser Interferometer Method for Measurement of Skin Friction. Experiments in Fluids, vol. 1, 1983, pp. 15–22.

37. Bouslog, S.: private communication, June 1991.

38. Berezin, I. S.; and Zhidkov, N. P.: Computing Methods. Pergamon Press, New York, 1965.

39. ASTM Special Technical Publication 470B: Manual on the Use of Thermocouples in Temperature Measurement. American Society for Testing and Materials, 1981.

40. White, F. M.: Viscous Fluid Flow. McGraw-Hill, Inc., 1974.

41. Chapman, A. J.: Heat Transfer. Macmillan Co., 1967.

42. Holman, J. P.: Experimental Methods for Engineers. Fourth ed. McGraw-Hill, 1984.

43. Maskell, E. C.: Flow Separation in Three Dimensions. RAE Rept. Aero 2565, Nov. 1955.

44. Wang, K. C.: Separation Patterns of Boundary Layer over an Inclined Body of Revolution. AIAA Journal, vol. 10, no. 8, 1972, pp. 1044–1050.

45. Peake, D. J.; and Tobak, M.: Three-Dimensional Interactions and Vortical Flows with Emphasis on High Speeds. NASA TM-81169, 1980.

46. Chapman, G. T.: Topological Classification of Flow Separation on Three-Dimensional Bodies. AIAA Paper 86-0485, 1986.

47. McCabe, A.: The Three-Dimensional Interaction of a Shock Wave with a Turbulent Boundary Layer. The Aeronautical Quarterly, Aug. 1966, pp. 231-252.

48. Hung, C. M.; and Sung, C. H.; and Chen, C. L.: Computation of Saddle Point of Attachment. AIAA Paper 91-1713, 1991.

49. Batcho, P.; and Sullivan J.: The 3-D Flowfield in a Supersonic Shock Boundary Layer Corner Interaction. AIAA Paper 88-0307, 1988.

50. Green, J. E.: Interactions Between Shock Waves and Turbulent Boundary Layers. Progress in Aerospace Sciences, vol. 11, 1970, pp. 235–340.

51. Cambier, L.; and Escande, B.: Calculation of a Three-Dimensional Shock Wave-Turbulent Boundary-Layer Interaction. AIAA Journal, vol. 28, no. 11, 1990, pp. 1901–1908.

52. Garrison, T. J.; and Settles, G. S.: Flowfield Visualization of Crossing Shock-Wave/Boundary-Layer Interactions. AIAA Paper 92-0750, 1992.

53. Stalker, R. J.: Sweepback Effects in Turbulent Boundary-Layer Shock-Wave Interaction. Journal of the Aeronautical Sciences, vol. 27, May 1960, pp. 348–356.

54. Sims, J. L.: Tables for Supersonic Flow Around Right Circular Cones at Zero Angle of Attack. NASA SP-3004, 1964.

55. Avduevskii, V. S.; and Medvedev, K. I.: Effect of Three-Dimensional Flow on Limiting Pressure Differential for Interaction of Boundary Layer with Shock Waves. Fluid Dynamics, vol. 2, no. 2, 1967, pp. 48–51.

56. Hopkins, E. J.: Charts for Predicting Turbulent Skin Friction from the Van Driest Method (II). NASA TN-D-6945, 1972.

57. Kim, K.-S.; Lee, Y.; and Settles, G. S.: Laser Interferometer/Preston Tube Skin-Friction Comparison in Shock/Boundary-Layer Interaction. AIAA Journal, vol. 29, no. 6, 1991, pp. 1007–1009.

58. Tanner, L. H.: Skin Friction Measurement by Viscosity Balance in Air and Water Flows. Journal of Physics E: Scientific Instruments, vol. 12, no. 7, 1979, pp. 610–619.

59. Murthy, V. S.; and Rose, W. C.: Wall Shear Stress Measurements in a Shock-Wave Boundary-Layer Interaction. AIAA Journal, vol. 16, no. 7, 1978, pp. 667–672.

Table 1. Average tunnel operating conditions.

P_t	172.37 [kPa] (1.7 atm)
T_t	280 [K]
ρ_t	2.1451 [kg/m^3]
M_∞	2.89
U_∞	593 [m/s]
P_∞	5.54 [kPa]
T_∞	105 [K]
ρ_∞	0.1841 [kg/m^3]
μ_∞	7.273×10^{-6} [N s/m^2]
Re	15.0×10^6 [1/m]
δ_o	1.10 [cm]

Table 2. Location of cylinder-flare junction.

ϕ [deg]	x_j [cm]
0	0.00
15	0.23
30	0.84
45	1.65
60	2.55
75	3.46
90	4.31
105	5.08
120	5.74
135	6.27
150	6.66
165	6.90
180	6.98

Table 3. Summary of LISF system characteristics.

Laser power [mW]	5
Laser light wavelength [μ m]	0.6328
Beam spot diameter [μ m]	200
Typical beam incident angle [deg]	5
Measurement beam power [mW]	0.1
Typical distance from leading edge [mm]	2.2

Table 4. Property summary of Dow Corning 200 Fluids.

	Nominal Kinematic Viscosity		
	200 [cs]	500 [cs]	1000 [cs]
Specific gravity (@298 K)	0.967	0.969	0.970
Refractive index (@298 K)	1.4032	1.4034	1.4035
Coefficient of expansion [cc/cc/K]	0.00096	0.00096	0.00096
Surface tension (@298 K) [dynes/cm]	21.0	21.1	21.2
Reference viscosity (@313 K) [cs]	155	370	750
Viscosity-Temp coefficient [1/K]			
273 K< T ≤ 313 K	0.0170742	0.0160666	0.0175613
313 K< T ≤ 353 K	0.0160180	0.0162908	0.0161601

Table 5. Upstream influence position from oil flow visualization.

ϕ [deg]	x_u [cm]	$l_u \equiv x_j - x_u$ [cm]
0	-	-
15	-0.40	0.63
30	-0.32	1.16
45	0.05	1.60
60	0.54	2.01
75	1.15	2.31
90	1.84	2.47
105	2.51	2.57
120	2.91	2.83
135	3.73	2.54
150	4.31	2.35
165	-	-
180	-	-

Table 6. Singular point locations from oil flow visualization.

Singular Points		ϕ [deg]	x [cm]
Saddle of Separation	S1	0	-0.30
Node of Attachment	N1	0	≈ 0
Focus of Separation	N2	156	5.00
Saddle of Separation	S2	156	5.25
Focus of Separation	N3	160	5.70
Saddle of Separation	S4	180	5.00
Saddle of Attachment	S5	180	7.82
Node of Attachment	N6	-	cyl. tip
Node of Separation	N7	-	cyl. aft

Table 7. Position of separation lines from oil flow visualization.

ϕ [deg]	x_s [cm]	$l_s \equiv x_j - x_s$ [cm]
Emanating from $S1$		
0	-0.30	0.30
15	-0.19	0.42
30	0.26	0.58
45	0.60	0.95
60	1.12	1.43
75	1.73	1.73
90	2.50	1.81
105	3.20	1.88
120	3.86	1.88
135	4.56	1.71
150	5.21	1.45
Emanating from $S4$		
165	5.00	1.90
180	5.00	1.98

Table 8. Attachment line position from oil flow visualization.

ϕ [deg]	x_a [cm]	$l_a \equiv x_a - x_j$ [cm]
0	-	-
15	-	-
30	1.30	0.46
45	2.21	0.56
60	3.21	0.66
75	4.30	0.84
90	5.25	0.94
105	5.88	0.80
120	6.42	0.68
135	6.93	0.66
150	7.31	0.65
165	7.65	0.75
180	7.82	0.84

Table 9. Velocity profile of undisturbed boundary layer (run 301).

y [cm]	U [m/s]	$< u'^2 >$ [m/s]^2	$< v'^2 >$ [m/s]^2	$< u'v' >$ [m/s]^2
0.064	387.5	2198.3	400.5	-520.1
0.127	422.6	1772.7	421.0	-453.0
0.191	448.1	1490.3	405.6	-406.4
0.254	467.9	1330.9	383.1	-369.3
0.318	484.2	1182.3	375.8	-333.3
0.381	499.2	1075.6	345.7	-303.0
0.445	513.4	934.5	312.3	-265.5
0.508	526.1	809.4	275.6	-223.0
0.572	537.3	684.7	230.9	-184.8
0.635	547.1	576.3	204.3	-155.7
0.699	556.7	470.1	185.3	-143.7
0.762	565.3	358.9	147.3	-104.1
0.826	572.8	253.4	115.2	-72.4
0.889	579.2	163.3	86.4	-43.6
0.953	583.5	94.0	63.5	-22.2
1.016	586.3	53.2	46.7	-8.2
1.080	587.7	32.3	36.1	-0.9
1.143	588.1	25.0	28.3	1.0
1.207	588.3	21.1	23.6	2.1
1.270	587.8	19.1	20.5	3.0
1.397	587.5	17.2	17.5	3.1
1.524	587.2	16.4	16.2	2.9

Table 10. Deduced C_{f_x} from LDV measurements in undisturbed boundary layer.

Run	x [cm]	δ [cm]	$C_{f_x} \equiv \tau_x / \frac{1}{2}\rho_\infty U_\infty^2$
288	-2.00	1.09	0.00141
288	-1.50	1.04	0.00144
329	-1.00	1.08	0.00142
350	-0.50	1.05	0.00141
351	-0.50	1.04	0.00143
248	0.00	1.15	0.00149
301	0.50	1.08	0.00144
312	0.50	1.16	0.00145
312	0.50	1.16	0.00146
302	1.00	1.08	0.00144

Table 11. Surface pressure data along $\phi = 0°$.

	x [cm]	P/P_t		x [cm]	P/P_t
1	-2.00	0.0337	16	3.85	0.0877
2	-1.75	0.0337	17	4.85	0.0873
3	-1.50	0.0338	18	5.35	0.0881
4	-1.25	0.0338	19	5.85	0.0874
5	-0.75	0.0339	20	6.35	0.0883
6	-0.50	0.0350	21	6.85	0.0891
7	-0.25	0.0417	22	7.35	0.0890
8	0.00	0.0546	23	7.85	0.0890
9	0.35	0.0640	24	8.35	0.0888
10	0.85	0.0685	25	8.85	0.0889
11	1.35	0.0753	26	9.35	0.0887
12	1.85	0.0814	27	10.85	0.0275
13	2.35	0.0859	28	12.35	0.0249
14	2.85	0.0871	29	13.85	0.0251
15	3.35	0.0868			

Table 12. Surface pressure data along $\phi = 15°$.

	x [cm]	P/P_t		x [cm]	P/P_t
1	-2.00	0.0336	15	4.55	0.0867
2	-1.75	0.0338	16	5.05	0.0866
3	-1.25	0.0337	17	5.55	0.0871
4	-0.50	0.0338	18	6.05	0.0874
5	-0.25	0.0378	19	6.55	0.0884
6	0.00	0.0471	20	7.05	0.0893
7	0.55	0.0628	21	7.55	0.0898
8	1.05	0.0691	22	8.05	0.0895
9	1.55	0.0751	23	8.55	0.0888
10	2.05	0.0815	24	9.05	0.0893
11	2.55	0.0850	25	9.55	0.0902
12	3.05	0.0864	26	11.05	0.0273
13	3.55	0.0874	27	12.55	0.0247
14	4.05	0.0874	28	14.05	0.0243

Table 13. Surface pressure data along $\phi = 30°$.

	x [cm]	P/P_t		x [cm]	P/P_t
1	-2.00	0.0330	16	4.60	0.0861
2	-1.75	0.0331	17	5.10	0.0862
3	-1.50	0.0328	18	5.60	0.0886
4	-1.25	0.0329	19	6.10	0.0864
5	-0.50	0.0328	20	6.60	0.0885
6	-0.25	0.0333	21	7.10	0.0882
7	0.00	0.0356	22	7.60	0.0899
8	0.25	0.0410	23	8.10	0.0898
9	0.50	0.0481	24	8.60	0.0900
10	0.75	0.0514	25	9.10	0.0900
11	2.10	0.0742	26	9.60	0.0900
12	2.60	0.0795	27	10.10	0.0891
13	3.10	0.0822	28	11.60	0.0261
14	3.60	0.0845	29	13.10	0.0244
15	4.10	0.0853	30	14.60	0.0243

Table 14. Surface pressure data along $\phi = 45°$.

	x [cm]	P/P_t		x [cm]	P/P_t
1	-2.00	0.0331	18	4.30	0.0831
2	-1.75	0.0332	19	4.80	0.0843
3	-1.50	0.0329	20	5.30	0.0860
4	-1.25	0.0331	21	5.80	0.0874
5	-0.50	0.0328	22	6.30	0.0877
6	-0.25	0.0330	23	6.80	0.0902
7	0.00	0.0329	24	7.30	0.0905
8	0.25	0.0341	25	7.80	0.0907
9	0.50	0.0378	26	8.30	0.0893
10	0.75	0.0438	27	8.80	0.0904
11	1.00	0.0487	28	9.30	0.0900
12	1.25	0.0511	29	9.80	0.0899
13	1.50	0.0517	30	10.30	0.0894
14	2.30	0.0656	31	10.80	0.0892
15	2.80	0.0733	32	12.30	0.0258
16	3.30	0.0783	33	13.80	0.0242
17	3.80	0.0825	34	15.30	0.0244

Table 15. Surface pressure data along $\phi = 60°$.

	x [cm]	P/P_t		x [cm]	P/P_t
1	-2.00	0.0331	20	4.25	0.0751
2	-1.75	0.0331	21	4.75	0.0786
3	-1.50	0.0330	22	5.25	0.0820
4	-1.25	0.0329	23	5.75	0.0834
5	-0.50	0.0330	24	6.25	0.0855
6	-0.25	0.0330	25	6.75	0.0876
7	0.00	0.0328	26	7.25	0.0886
8	0.25	0.0328	27	7.75	0.0885
9	0.50	0.0328	28	8.25	0.0895
10	0.75	0.0336	29	8.75	0.0901
11	1.00	0.0372	30	9.25	0.0901
12	1.25	0.0416	31	9.75	0.0905
13	1.50	0.0456	32	10.25	0.0903
14	1.75	0.0480	33	10.75	0.0898
15	2.00	0.0497	34	11.25	0.0887
16	2.25	0.0505	35	11.75	0.0881
17	2.50	0.0515	36	13.25	0.0255
18	3.25	0.0631	37	14.75	0.0241
19	3.75	0.0701	38	16.25	0.0246

Table 16. Surface pressure data along $\phi = 75°$.

	x [cm]	P/P_t		x [cm]	P/P_t
1	-2.00	0.0334	22	4.35	0.0666
2	-1.75	0.0333	23	4.85	0.0719
3	-1.50	0.0332	24	5.35	0.0754
4	-1.25	0.0331	25	5.85	0.0800
5	-0.50	0.0332	26	6.35	0.0834
6	-0.25	0.0330	27	6.85	0.0860
7	0.00	0.0331	28	7.35	0.0884
8	0.25	0.0330	29	8.35	0.0915
9	0.50	0.0330	30	8.85	0.0913
10	0.75	0.0328	31	9.35	0.0914
11	1.00	0.0335	32	9.85	0.0925
12	1.25	0.0342	33	10.35	0.0913
13	1.50	0.0356	34	10.85	0.0914
14	1.75	0.0392	35	11.35	0.0908
15	2.00	0.0441	36	11.85	0.0905
16	2.25	0.0468	37	12.35	0.0893
17	2.50	0.0489	38	12.85	0.0899
18	2.75	0.0501	39	14.35	0.0252
19	3.00	0.0515	40	15.85	0.0249
20	3.25	0.0517	41	17.35	0.0263
21	3.50	0.0530			

Table 17. Surface pressure data along $\phi = 90°$.

	x [cm]	P/P_t		x [cm]	P/P_t
1	-2.00	0.0332	24	4.25	0.0517
2	-1.75	0.0331	25	5.10	0.0607
3	-1.50	0.0330	26	5.60	0.0671
4	-1.25	0.0330	27	6.10	0.0719
5	-0.50	0.0329	28	6.60	0.0774
6	-0.25	0.0328	29	7.10	0.0800
7	0.00	0.0326	30	7.60	0.0817
8	0.25	0.0328	31	8.10	0.0850
9	0.50	0.0326	32	8.60	0.0872
10	0.75	0.0327	33	9.10	0.0895
11	1.00	0.0331	34	9.60	0.0908
12	1.25	0.0331	35	10.10	0.0912
13	1.50	0.0323	36	10.60	0.0917
14	1.75	0.0329	37	11.10	0.0921
15	2.00	0.0341	38	11.60	0.0916
16	2.25	0.0371	39	12.10	0.0909
17	2.50	0.0406	40	12.60	0.0906
18	2.75	0.0441	41	13.10	0.0908
19	3.00	0.0467	42	13.60	0.0918
20	3.25	0.0484	43	15.10	0.0264
21	3.50	0.0494	44	16.60	0.0250
22	3.75	0.0505	45	18.10	0.0257
23	4.00	0.0507			

Table 18. Surface pressure data along $\phi = 105°$.

	x [cm]	P/P_t		x [cm]	P/P_t
1	-2.00	0.0332	25	4.50	0.0512
2	-1.75	0.0332	26	4.75	0.0520
3	-1.50	0.0331	27	5.00	0.0527
4	-1.25	0.0331	28	5.80	0.0645
5	-0.50	0.0330	29	6.30	0.0700
6	-0.25	0.0330	30	6.80	0.0753
7	0.00	0.0328	31	7.30	0.0808
8	0.25	0.0328	32	7.80	0.0850
9	0.50	0.0328	33	8.30	0.0870
10	0.75	0.0328	34	8.80	0.0899
11	1.00	0.0332	35	9.30	0.0916
12	1.25	0.0333	36	9.80	0.0927
13	1.50	0.0324	37	10.30	0.0932
14	1.75	0.0324	38	10.80	0.0953
15	2.00	0.0324	39	11.30	0.0935
16	2.25	0.0326	40	11.80	0.0928
17	2.50	0.0331	41	12.30	0.0934
18	2.75	0.0345	42	12.80	0.0927
19	3.00	0.0386	43	13.30	0.0927
20	3.25	0.0420	44	13.80	0.0927
21	3.50	0.0455	45	14.30	0.0926
22	3.75	0.0475	46	16.80	0.0276
23	4.00	0.0491	47	18.30	0.0273
24	4.25	0.0501	48	19.80	0.0290

Table 19. Surface pressure data along $\phi = 120°$.

	x [cm]	P/P_t		x [cm]	P/P_t
1	-2.00	0.0332	27	5.00	0.0511
2	-1.75	0.0332	28	5.25	0.0529
3	-1.50	0.0331	29	5.50	0.0544
4	-1.25	0.0331	30	5.75	0.0565
5	-0.50	0.0331	31	6.50	0.0688
6	-0.25	0.0330	32	7.00	0.0751
7	0.00	0.0330	33	7.50	0.0792
8	0.25	0.0329	34	8.00	0.0836
9	0.50	0.0327	35	8.50	0.0876
10	0.75	0.0327	36	9.00	0.0897
11	1.00	0.0332	37	9.50	0.0911
12	1.25	0.0332	38	10.00	0.0921
13	1.50	0.0325	39	10.50	0.0916
14	1.75	0.0324	40	11.00	0.0926
15	2.00	0.0324	41	11.50	0.0927
16	2.25	0.0325	42	12.00	0.0932
17	2.50	0.0322	43	12.50	0.0941
18	2.75	0.0323	44	13.00	0.0935
19	3.00	0.0328	45	13.50	0.0908
20	3.25	0.0336	46	14.00	0.0946
21	3.50	0.0355	47	14.50	0.0944
22	3.75	0.0387	48	15.00	0.0945
23	4.00	0.0421	49	16.50	0.0288
24	4.25	0.0450	50	18.00	0.0291
25	4.50	0.0474	51	19.50	0.0299
26	4.75	0.0494			

Table 20. Surface pressure data along $\phi = 135°$.

	x [cm]	P/P_t		x [cm]	P/P_t
1	-2.00	0.0332	28	5.25	0.0526
2	-1.75	0.0333	29	5.50	0.0559
3	-1.50	0.0331	30	5.75	0.0584
4	-1.25	0.0332	31	6.00	0.0612
5	-0.50	0.0331	32	6.25	0.0632
6	-0.25	0.0333	33	7.05	0.0733
7	0.00	0.0328	34	7.55	0.0782
8	0.25	0.0329	35	8.05	0.0818
9	0.50	0.0327	36	8.55	0.0852
10	0.75	0.0329	37	9.05	0.0890
11	1.00	0.0332	38	9.55	0.0908
12	1.25	0.0334	39	10.05	0.0915
13	1.50	0.0324	40	10.55	0.0926
14	1.75	0.0325	41	11.05	0.0919
15	2.00	0.0324	42	11.55	0.0919
16	2.25	0.0325	43	12.05	0.0919
17	2.50	0.0321	44	12.55	0.0910
18	2.75	0.0323	45	13.05	0.0927
19	3.00	0.0324	46	13.55	0.0915
20	3.25	0.0326	47	14.05	0.0929
21	3.50	0.0325	48	14.55	0.0934
22	3.75	0.0330	49	15.05	0.0933
23	4.00	0.0338	50	15.55	0.0962
24	4.25	0.0363	51	17.05	0.0323
25	4.50	0.0402	52	18.55	0.0316
26	4.75	0.0448	53	20.05	0.0308
27	5.00	0.0488			

Table 21. Surface pressure data along $\phi = 150°$.

	x [cm]	P/P_t		x [cm]	P/P_t
1	-2.00	0.0331	29	5.50	0.0565
2	-1.75	0.0333	30	5.75	0.0601
3	-1.50	0.0329	31	6.00	0.0625
4	-1.25	0.0332	32	6.25	0.0647
5	-0.50	0.0327	33	6.50	0.0663
6	-0.25	0.0331	34	6.75	0.0681
7	0.00	0.0327	35	7.40	0.0753
8	0.25	0.0330	36	7.90	0.0796
9	0.50	0.0325	37	8.40	0.0827
10	0.75	0.0327	38	8.90	0.0855
11	1.00	0.0329	39	9.40	0.0876
12	1.25	0.0332	40	9.90	0.0891
13	1.50	0.0322	41	10.40	0.0890
14	1.75	0.0324	42	10.90	0.0904
15	2.00	0.0323	43	11.40	0.0895
16	2.25	0.0324	44	11.90	0.0910
17	2.50	0.0320	45	12.40	0.0913
18	2.75	0.0322	46	12.90	0.0918
19	3.00	0.0322	47	13.40	0.0907
20	3.25	0.0324	48	13.90	0.0920
21	3.50	0.0322	49	14.40	0.0915
22	3.75	0.0325	50	14.90	0.0938
23	4.00	0.0321	51	15.40	0.0938
24	4.25	0.0324	52	15.90	0.0936
25	4.50	0.0327	53	17.40	0.0346
26	4.75	0.0357	54	18.90	0.0332
27	5.00	0.0426	55	20.40	0.0316
28	5.25	0.0514			

Table 22. Surface pressure data along $\phi = 165°$.

	x [cm]	P/P_t		x [cm]	P/P_t
1	-2.00	0.0329	29	5.50	0.0555
2	-1.75	0.0329	30	5.75	0.0584
3	-1.50	0.0328	31	6.00	0.0606
4	-1.25	0.0328	32	6.25	0.0625
5	-0.50	0.0327	33	6.50	0.0643
6	-0.25	0.0327	34	6.75	0.0665
7	0.00	0.0325	35	7.00	0.0683
8	0.25	0.0325	36	7.60	0.0754
9	0.50	0.0323	37	8.10	0.0789
10	0.75	0.0324	38	8.60	0.0823
11	1.00	0.0327	39	9.10	0.0848
12	1.25	0.0327	40	9.60	0.0862
13	1.50	0.0320	41	10.10	0.0872
14	1.75	0.0321	42	10.60	0.0882
15	2.00	0.0321	43	11.10	0.0887
16	2.25	0.0321	44	11.60	0.0892
17	2.50	0.0317	45	12.10	0.0887
18	2.75	0.0317	46	12.60	0.0894
19	3.00	0.0321	47	13.10	0.0902
20	3.25	0.0321	48	13.60	0.0902
21	3.50	0.0320	49	14.10	0.0903
22	3.75	0.0321	50	14.60	0.0918
23	4.00	0.0318	51	15.10	0.0920
24	4.25	0.0318	52	15.60	0.0925
25	4.50	0.0320	53	16.10	0.0949
26	4.75	0.0336	54	17.60	0.0359
27	5.00	0.0410	55	19.10	0.0338
28	5.25	0.0492	56	20.60	0.0314

Table 23. Surface pressure data along $\phi = 180°$.

	x [cm]	P/P_t		x [cm]	P/P_t
1	-2.00	0.0332	30	5.75	0.0593
2	-1.75	0.0333	31	6.00	0.0611
3	-1.50	0.0330	32	6.25	0.0633
4	-1.25	0.0332	33	6.50	0.0653
5	-0.50	0.0329	34	6.75	0.0678
6	-0.25	0.0331	35	7.00	0.0703
7	0.00	0.0328	36	7.35	0.0733
8	0.25	0.0329	37	7.85	0.0772
9	0.50	0.0327	38	8.35	0.0804
10	0.75	0.0328	39	8.85	0.0828
11	1.00	0.0330	40	9.35	0.0847
12	1.25	0.0332	41	9.85	0.0856
13	1.50	0.0322	42	10.35	0.0866
14	1.75	0.0325	43	10.85	0.0874
15	2.00	0.0323	44	11.35	0.0879
16	2.25	0.0324	45	11.85	0.0876
17	2.50	0.0322	46	12.35	0.0888
18	2.75	0.0322	47	12.85	0.0896
19	3.00	0.0323	48	13.35	0.0901
20	3.25	0.0325	49	13.85	0.0903
21	3.50	0.0322	50	14.35	0.0910
22	3.75	0.0324	51	14.85	0.0918
23	4.00	0.0320	52	15.35	0.0917
24	4.25	0.0323	53	15.85	0.0927
25	4.50	0.0327	54	16.35	0.0926
26	4.75	0.0357	55	17.85	0.0361
27	5.00	0.0442	56	19.35	0.0355
28	5.25	0.0521	57	20.85	0.0322
29	5.50	0.0566			

Table 24. Upstream influence position from pressure data.

ϕ [deg]	x_u [cm]	$l_u \equiv x_j - x_u$ [cm]
0	-0.54	0.54
15	-0.36	0.59
30	-0.12	0.96
45	0.18	1.47
60	0.69	1.86
75	1.32	2.14
90	1.90	2.41
105	2.66	2.42
120	3.25	2.49
135	4.01	2.26
150	4.62	2.04
165	4.70	2.20
180	4.65	2.33

Table 25. Separation pressure and separation line position from pressure data.

ϕ [deg]	x_s [cm]	$l_s \equiv x_j - x_s$ [cm]	P_s/P_∞
Emanating from $S1$			
0	-	-	-
15	-	-	-
30	0.50	0.34	1.45
45	1.00	0.65	1.47
60	1.50	1.05	1.37
75	2.00	1.46	1.33
90	2.75	1.56	1.33
105	3.50	1.58	1.37
120	4.25	1.49	1.36
135	4.75	1.52	1.35
150	5.25	1.41	1.55
Emanating from $S4$			
165	5.25	1.65	1.48
180	5.25	1.73	1.57

Table 26. Peak plateau pressure on flare.

ϕ [deg]	x_{pk} [cm]	$l_{pk} \equiv x_{pk} - x_j$ [cm]	P_{pk}/P_t	P_{pk}/P_∞
0	2.85	2.85	0.0871	2.62
15	3.55	3.32	0.0874	2.63
30	7.60	6.76	0.0899	2.71
45	6.80	5.15	0.0902	2.72
60	8.75	6.20	0.0901	2.71
75	8.35	4.89	0.0915	2.76
90	9.60	5.29	0.0908	2.73
105	9.80	4.72	0.0927	2.79
120	10.00	4.26	0.0921	2.77
135	10.05	3.78	0.0915	2.76
150	10.90	4.24	0.0904	2.72
165	14.60	7.70	0.0918	2.77
180	14.85	7.87	0.0918	2.77

Table 27. Afterbody pressure.

ϕ [deg]	P_a/P_t	P_{pk}/P_a
0	0.0275	3.12
15	0.0273	3.16
30	0.0261	3.44
45	0.0258	3.50
60	0.0255	3.53
75	0.0252	3.63
90	0.0264	3.44
105	0.0276	3.36
120	0.0288	3.20
135	0.0323	2.83
150	0.0346	2.61
165	0.0359	2.56
180	0.0361	2.54

Table 28. LISF measurements in the undisturbed boundary layer.

Run	x [cm]	τ_x [N/m^2]	$C_{f_x} \equiv \tau_x / \frac{1}{2}\rho_\infty U_\infty^2$	Comment
599	-5.00	52.01	0.00161	plastic/Monokote, 500 cs
602	-4.00	55.46	0.00166	"
595	-3.00	52.30	0.00158	"
596	-2.00	51.73	0.00158	"
646	-1.00	47.10	0.00146	"
639	0.0	48.53	0.00149	"
640	1.00	45.34	0.00141	"
645	1.00	44.01	0.00136	"
653	1.30	44.24	0.00137	"
675	1.50	44.94	0.00137	"
673	2.00	45.83	0.00142	"
659	3.00	45.13	0.00137	"
660	4.00	47.52	0.00146	"
555	-0.95	47.66	0.00147	plastic/Monokote, 200 cs
557	-0.95	51.06	0.00158	"
538	-5.76	64.17	0.00190	stainless steel, 500 cs
539	-5.47	55.70	0.00167	"
593	-3.00	57.97	0.00175	"
594	-3.00	55.70	0.00172	"
540	-4.00	46.77	0.00143	plastic/paint, 500 cs
546	-4.00	49.13	0.00151	"
548	-4.00	47.45	0.00147	"
549	-4.00	56.43	0.00171	"
550	-4.00	49.55	0.00150	"
541	-3.81	55.48	0.00169	"

Table 28. Concluded.

Run	x [cm]	τ_x [N/m^2]	$C_{f_x} \equiv \tau_x/\frac{1}{2}\rho_\infty U_\infty^2$	Comment
538	-5.24	61.56	0.00181	downstream beam
539	-4.95	55.42	0.00166	”
599	-4.48	51.50	0.00161	”
540	-3.48	50.46	0.00153	”
546	-3.48	49.35	0.00167	”
548	-3.48	49.03	0.00152	”
549	-3.48	46.81	0.00145	”
550	-3.48	51.97	0.00159	”
602	-3.48	48.60	0.00148	”
541	-3.29	50.19	0.00154	”
595	-2.48	52.48	0.00157	”
596	-1.48	50.73	0.00155	”
639	0.52	50.91	0.00156	”
640	1.52	44.22	0.00137	”
645	1.52	46.44	0.00144	”
653	1.82	47.49	0.00147	”
673	2.52	44.04	0.00142	”
659	3.52	45.96	0.00140	”

Table 29. Surface pressure data along $\phi = 0°$ (side of cylinder).

	x [cm]	P/P_t		x [cm]	P/P_t
1	-2.00	0.0323	17	3.85	0.0846
2	-1.75	0.0326	18	4.35	0.0855
3	-1.50	0.0321	19	4.85	0.0852
4	-1.25	0.0325	20	5.35	0.0856
5	-1.00	0.0319	21	5.85	0.0846
6	-0.75	0.0322	22	6.35	0.0850
7	-0.50	0.0324	23	6.85	0.0870
8	-0.25	0.0385	24	7.35	0.0887
9	0.00	0.0549	25	7.85	0.0924
10	0.35	0.0685	26	8.35	0.0886
11	0.85	0.0745	27	8.85	0.0868
12	1.35	0.0805	28	9.35	0.0860
13	1.85	0.0832	29	10.85	0.0264
14	2.35	0.0844	30	12.35	0.0254
15	2.85	0.0831	31	13.85	0.0243
16	3.35	0.0824			

77

Table 30. Average streamwise skin-friction data along $\phi = 0°$.

x [cm]	τ_x [N/ m^2]	$C_{f_x} \equiv \tau_x/\frac{1}{2}\rho_\infty U_\infty^2$
-5.00	52.01	0.00161
-4.00	55.46	0.00166
-3.00	52.30	0.00158
-2.00	51.73	0.00158
-0.95	49.36	0.00153
-0.45	31.18	0.00096
-0.35	13.57	0.00042
0.43	50.28	0.00155
0.86	64.25	0.00199
1.29	84.32	0.00261
1.72	88.53	0.00274
2.59	94.68	0.00293
3.45	103.25	0.00319
4.31	104.88	0.00324
5.17	108.43	0.00335
6.03	107.95	0.00334
6.89	105.25	0.00323
7.76	135.79	0.00420
8.62	117.05	0.00363
9.48	109.02	0.00340
11.00	49.64	0.00154
12.00	46.45	0.00144
13.00	38.84	0.00117
15.00	49.76	0.00153
17.00	46.85	0.00145

Table 31. Surface pressure data along $\phi = 90°$ (side of cylinder).

	x [cm]	P/P_t		x [cm]	P/P_t
1	-2.00	0.0317	25	4.00	0.0491
2	-1.75	0.0315	26	4.25	0.0499
3	-1.50	0.0316	27	5.10	0.0613
4	-1.25	0.0316	28	5.60	0.0688
5	-1.00	0.0311	29	6.10	0.0732
6	-0.75	0.0310	30	6.60	0.0789
7	-0.50	0.0309	31	7.10	0.0817
8	-0.25	0.0308	32	7.60	0.0833
9	0.00	0.0306	33	8.10	0.0856
10	0.25	0.0305	34	8.60	0.0869
11	0.50	0.0308	35	9.10	0.0879
12	0.75	0.0308	36	9.60	0.0887
13	1.00	0.0308	37	10.10	0.0882
14	1.25	0.0308	38	10.60	0.0880
15	1.50	0.0306	39	11.10	0.0881
16	1.75	0.0307	40	11.60	0.0876
17	2.00	0.0321	41	12.10	0.0872
18	2.25	0.0347	42	12.60	0.0871
19	2.50	0.0388	43	13.10	0.0870
20	2.75	0.0423	44	13.60	0.0872
21	3.00	0.0447	45	15.10	0.0254
22	3.25	0.0463	46	16.60	0.0240
23	3.50	0.0482	47	18.10	0.0273
24	3.75	0.0496			

Table 32. Average streamwise skin-friction data along $\phi = 90°$.

x [cm]	τ_x [N/ m^2]	$C_{f_x} \equiv \tau_x/\frac{1}{2}\rho_\infty U_\infty^2$
-1.00	47.10	0.00146
0.0	48.53	0.00149
1.00	44.83	0.00139
1.30	44.24	0.00137
2.10	28.86	0.00089
2.25	27.47	0.00084
3.00	25.52	0.00078
3.50	21.93	0.00067
3.85	16.18	0.00050
5.00	28.92	0.00089
6.00	36.75	0.00120
6.20	40.30	0.00125
6.54	41.98	0.00128
7.00	45.12	0.00143
7.54	52.54	0.00164
8.00	53.89	0.00167
8.25	61.83	0.00186
9.00	65.69	0.00198
9.61	67.09	0.00210
10.61	70.57	0.00218
11.54	71.13	0.00220
12.61	69.71	0.00212
13.86	65.06	0.00200
15.20	27.43	0.00085
16.40	17.01	0.00052
18.10	27.00	0.00083

Table 33. Resolved transverse skin-friction data along $\phi = 90°$.

x [cm]	C_{f_x}	β [deg] from oil flow	$C_{f_z} = C_{f_x} \tan\beta$
2.25	0.00084	39	0.00068
3.00	0.00078	47	0.00084
3.50	0.00067	48	0.00074
3.85	0.00050	50	0.00060
5.00	0.00089	48	0.00099
6.00	0.00120	32.5	0.00076
6.54	0.00128	24.5	0.00058
7.00	0.00143	20.5	0.00053
8.00	0.00167	17.5	0.00053
9.00	0.00198	11.0	0.00038
9.61	0.00210	10.0	0.00037
10.61	0.00218	8.5	0.00033
11.54	0.00220	7.0	0.00027
13.86	0.00200	5.0	0.00017

Table 34. Average transverse skin-friction data along $\phi = 90°$.

x [cm]	τ_z [N/m^2]	$C_{f_z} \equiv \tau_z / \frac{1}{2}\rho_\infty U_\infty^2$
2.25	24.27	0.00075
2.77	26.21	0.00081
3.00	30.49	0.00094
3.50	23.31	0.00072
3.85	19.75	0.00061
5.00	32.05	0.00099

Table 35. Surface pressure data along $\phi = 180°$ (side of cylinder).

	x [cm]	P/P_t		x [cm]	P/P_t
1	-2.00	0.0319	31	5.50	0.0577
2	-1.75	0.0322	32	5.75	0.0613
3	-1.50	0.0320	33	6.00	0.0636
4	-1.25	0.0315	34	6.25	0.0659
5	-1.00	0.0314	35	6.50	0.0678
6	-0.75	0.0314	36	6.75	0.0699
7	-0.50	0.0312	37	7.00	0.0721
8	-0.25	0.0311	38	7.35	0.0755
9	0.00	0.0308	39	7.85	0.0796
10	0.25	0.0309	40	8.35	0.0827
11	0.50	0.0310	41	8.85	0.0845
12	0.75	0.0311	42	9.35	0.0856
13	1.00	0.0310	43	9.85	0.0857
14	1.25	0.0310	44	10.35	0.0860
15	1.50	0.0306	45	10.85	0.0867
16	1.75	0.0307	46	11.35	0.0862
17	2.00	0.0308	47	11.85	0.0854
18	2.25	0.0309	48	12.35	0.0869
19	2.50	0.0305	49	12.85	0.0873
20	2.75	0.0305	50	13.35	0.0870
21	3.00	0.0311	51	13.85	0.0872
22	3.25	0.0305	52	14.35	0.0870
23	3.50	0.0313	53	14.85	0.0872
24	3.75	0.0312	54	15.35	0.0875
25	4.00	0.0298	55	15.85	0.0895
26	4.25	0.0298	56	16.35	0.0888
27	4.50	0.0313	57	17.85	0.0335
28	4.75	0.0338	58	19.35	0.0567
29	5.00	0.0427	59	20.85	0.0589
30	5.25	0.0532			

Table 36. Average streamwise skin-friction data along $\phi = 180°$.

x [cm]	τ_x [N/ m^2]	$C_{f_x} \equiv \tau_x / \frac{1}{2}\rho_\infty U_\infty^2$
1.50	44.94	0.00137
2.00	45.83	0.00142
3.00	45.13	0.00137
4.00	47.52	0.00146
4.50	35.12	0.00109
4.65	28.38	0.00087
5.50	-6.28	-0.00019
6.00	-11.88	-0.00036
6.25	-13.92	-0.00043
6.50	-13.43	-0.00042
7.20	-6.47	-0.00020
8.50	8.53	0.00026
9.00	22.36	0.00067
9.75	30.71	0.00096
10.50	38.91	0.00122
11.00	43.44	0.00131
11.20	46.08	0.00139
12.00	57.67	0.00174
12.50	57.64	0.00176
13.00	58.56	0.00182
14.00	62.72	0.00193
15.00	66.52	0.00203
16.00	73.38	0.00226
16.50	72.37	0.00227
16.90	78.49	0.00252
18.00	50.13	0.00151
19.15	39.03	0.00119
19.80	36.22	0.00110

Table 37. LISF Uncertainty analysis

		$(\Delta x_i/x_i)^2$
Nt $[1/sec]$	$126.7 \pm 3.8(\pm 3.0\%)$	0.000899
x $[mm]$	$2.49 \pm 0.05(\pm 2.0\%)$	0.000403
θ_i $[deg]$	7.4 ± 1	
$\cos\theta_i$	0.9917 ± 0.00225	0.000005
T_s $[^\circ K]$	287.3 ± 4	shown in μ_o
T_o $[^\circ K]$	289.4 ± 2	shown in U_∞
P_o $[N/m^2]$	$1.7320 \times 10^5(\pm 1.0\%)$	shown in ρ_∞
μ_o $[N\ sec/m^2]$	$0.0548 \pm 0.0035(\pm 6.3\%)$	0.004079
ρ_∞ $[kg/m^3]$	$0.1789(\pm 1.0\%)$	0.000100
U_∞ $[m/sec]$	$603.07 \pm 6.0(\pm 1.0\%)$	0.000100(x4)
C_f	$0.00146 \pm 0.00011(\pm 7.7\%)$	0.005886
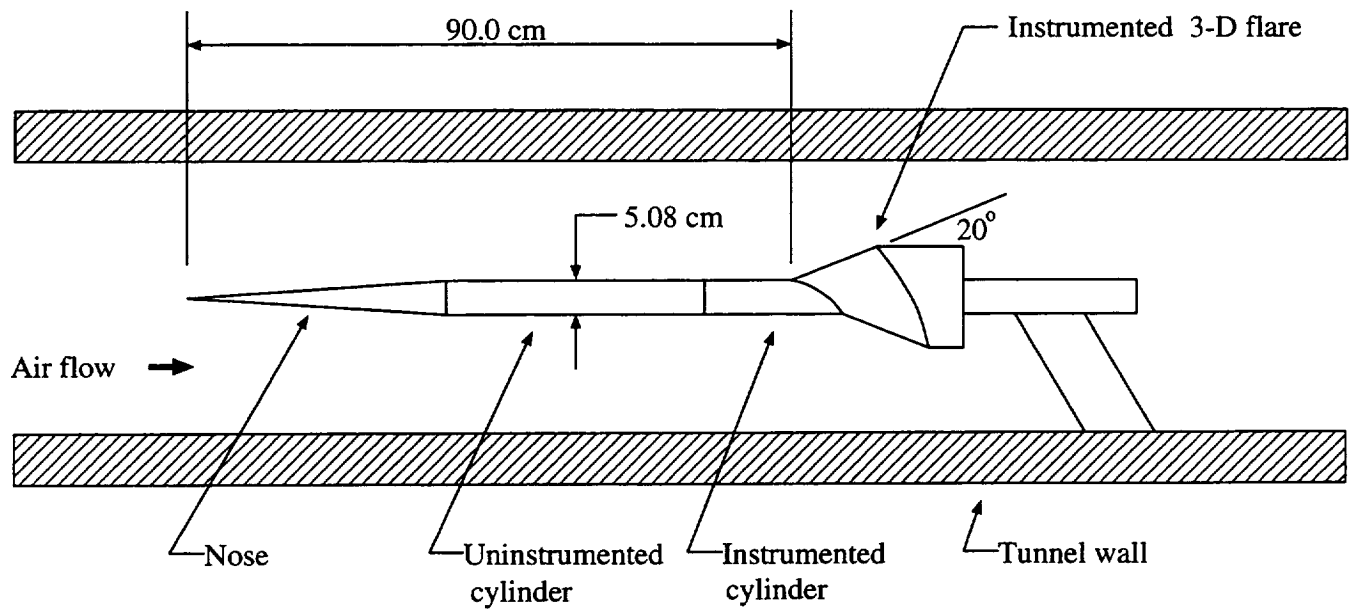
Figure 1. Schematic of model for 3-D SW/BLI test.
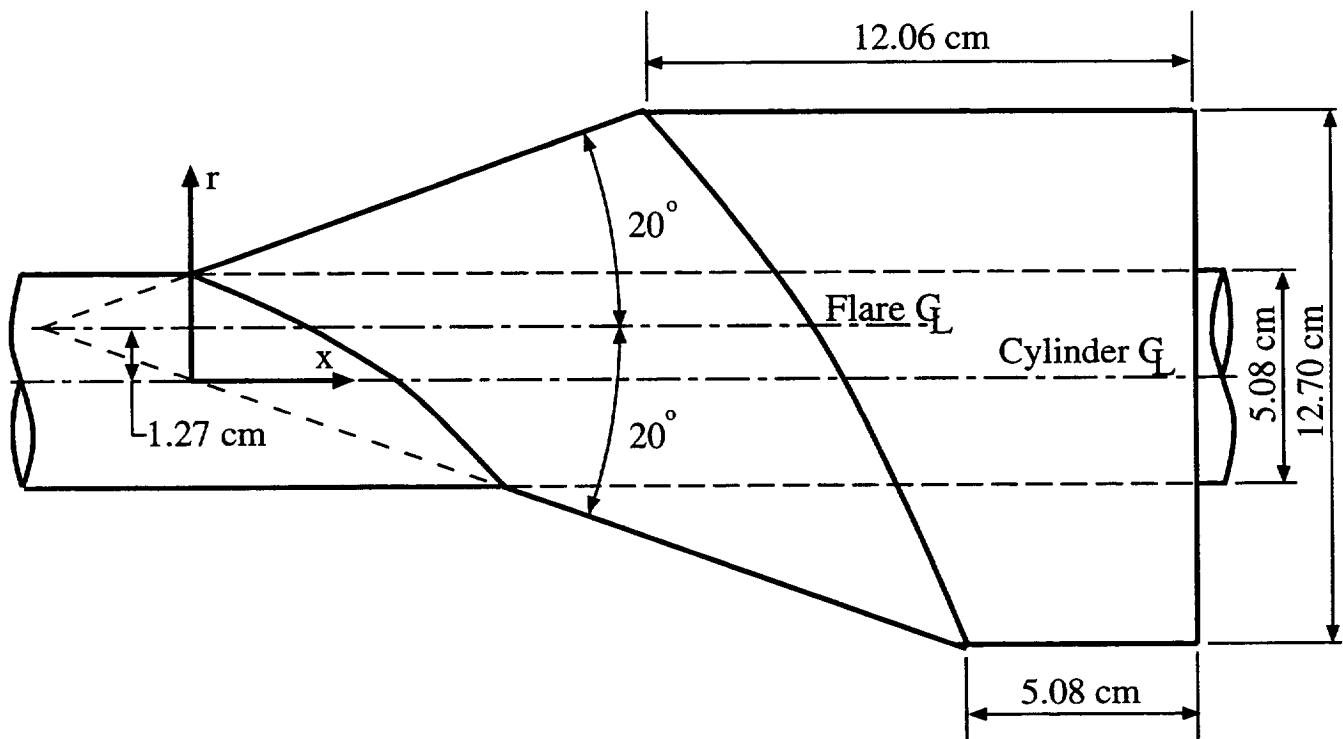
Figure 1. Concluded.
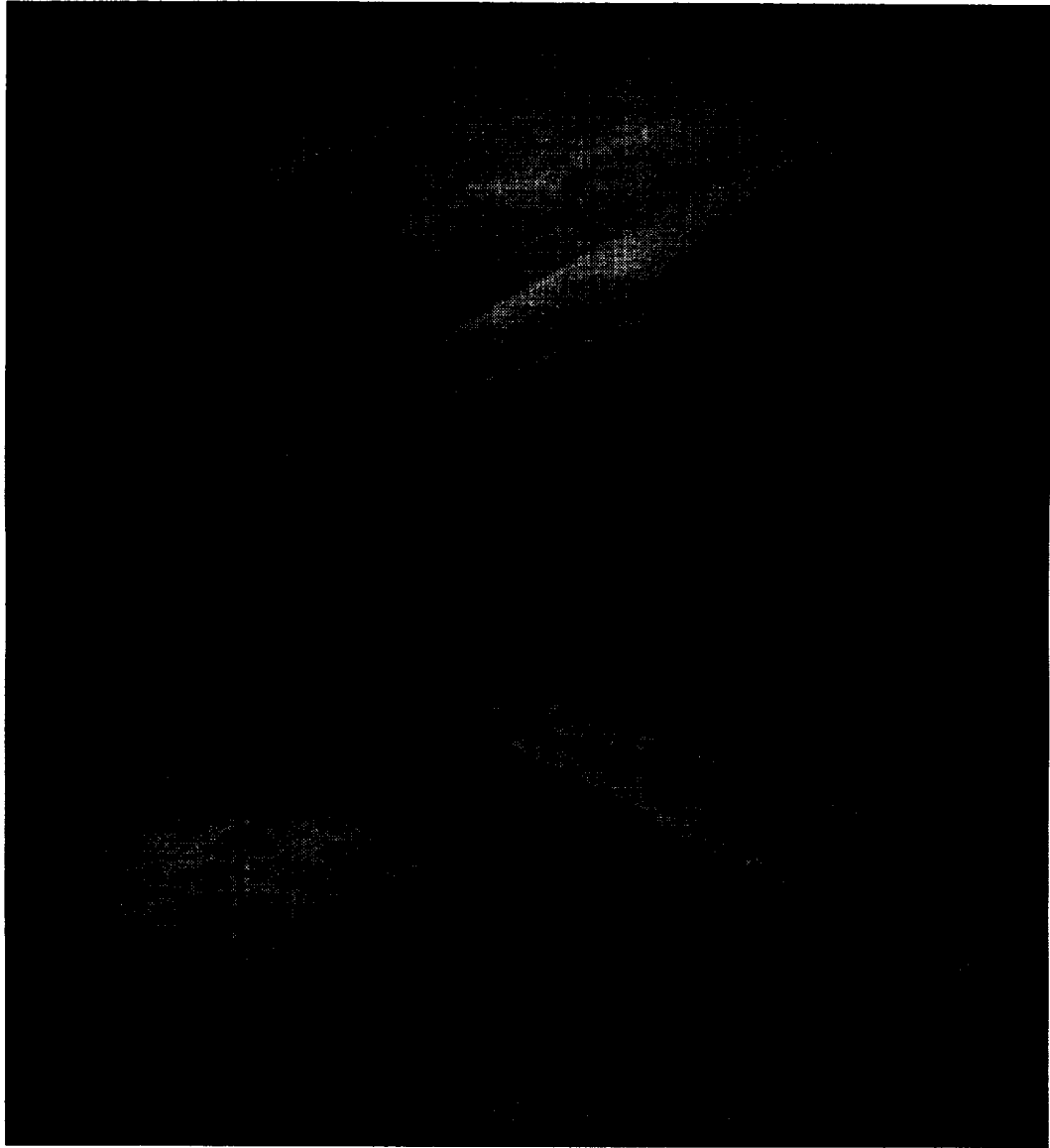
Figure 2. Schlieren visualization, $\phi = 0°$ along the top of the cylinder.
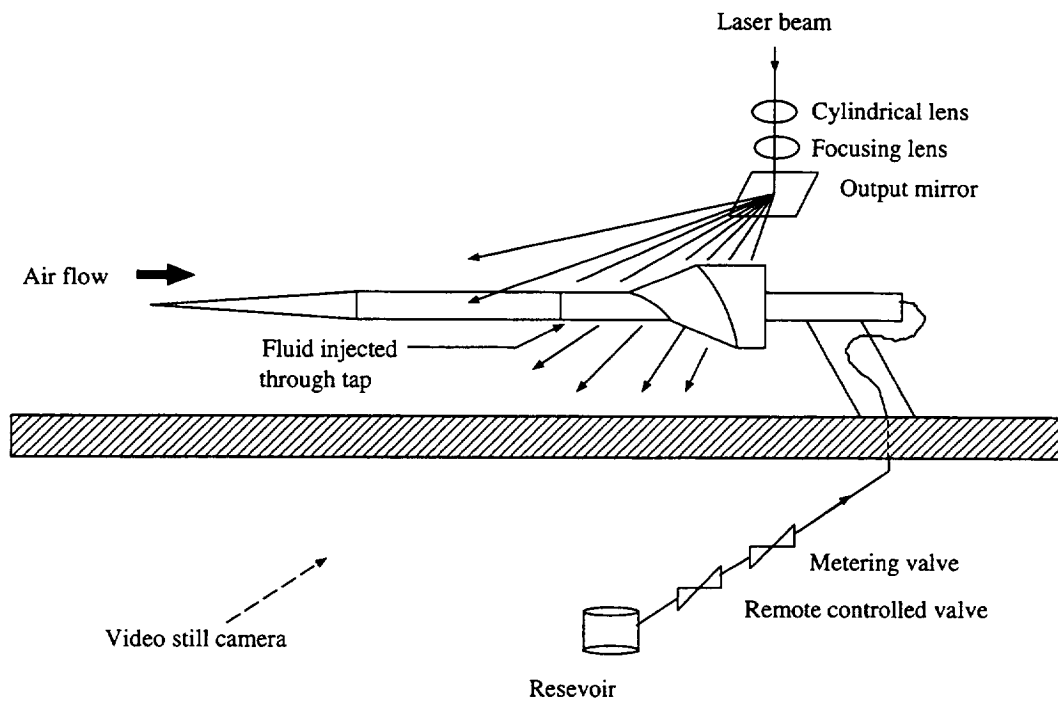
Figure 3. Laser light sheet illumination schematic.

(1) 12 W argon-ion laser, operated multiline
(2) 12 W argon-ion laser, operated singleline
(3) Mirror (typical)
(4) Collimating lens
(5) Beam expander
(6) Dispersion prism
(7) Beam splitter & bragg cell

(8) Beam reducer
(9) Mirrors, focusing lens
(10) Receiving optics
(11) Main optics table
(12) Tunnel wall
(13) BK-7 window
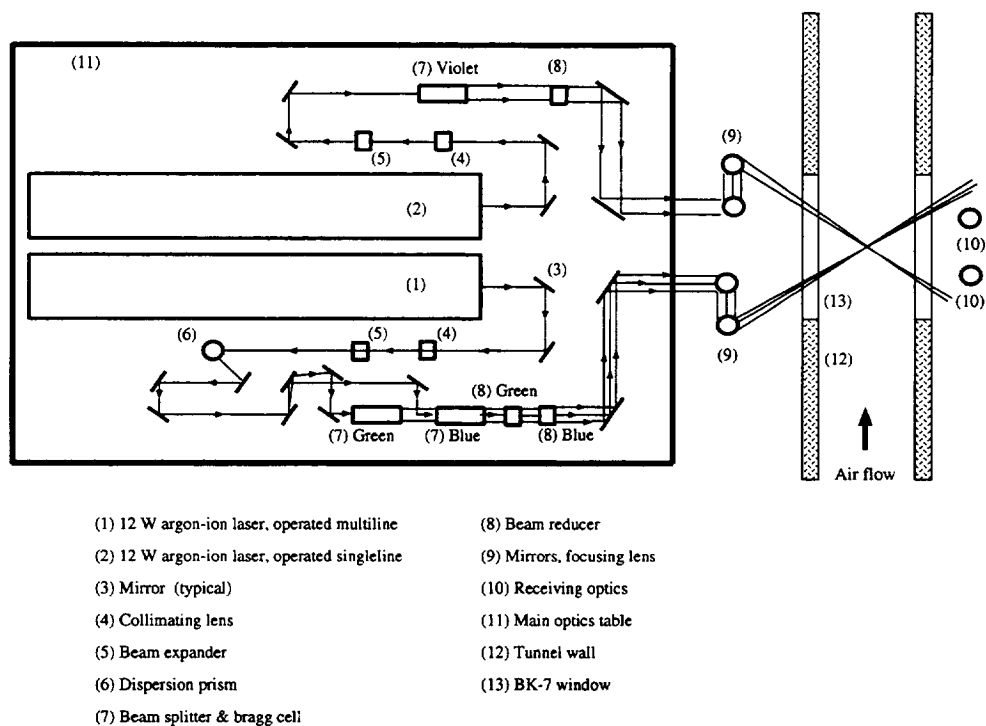
Figure 4. HRC-1 3-D laser Doppler velocimeter system.

87
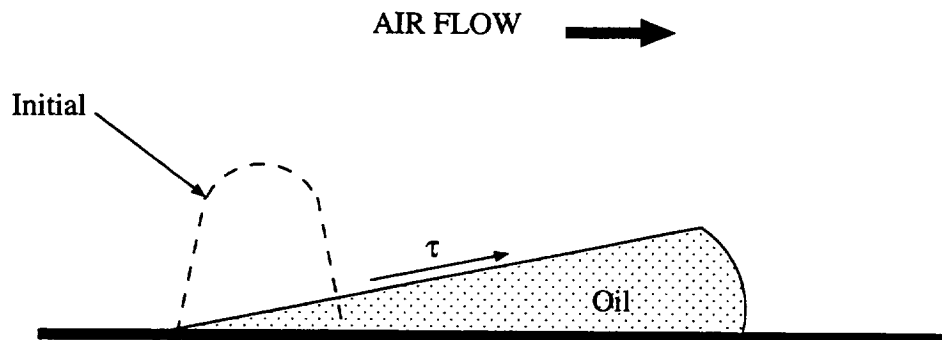
AIR FLOW ➡

Figure 5. Flow of an oil drop as result of shear of air flow.
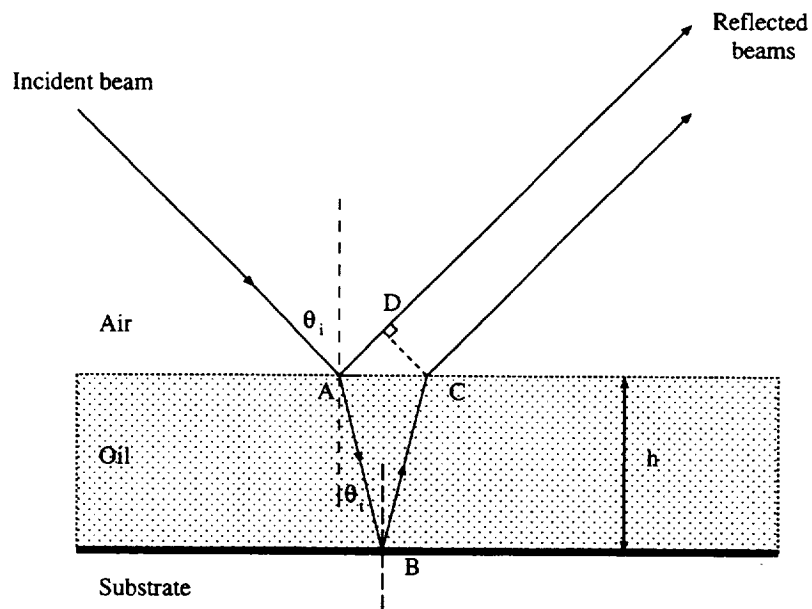
Figure 6. Single thin-film interference.
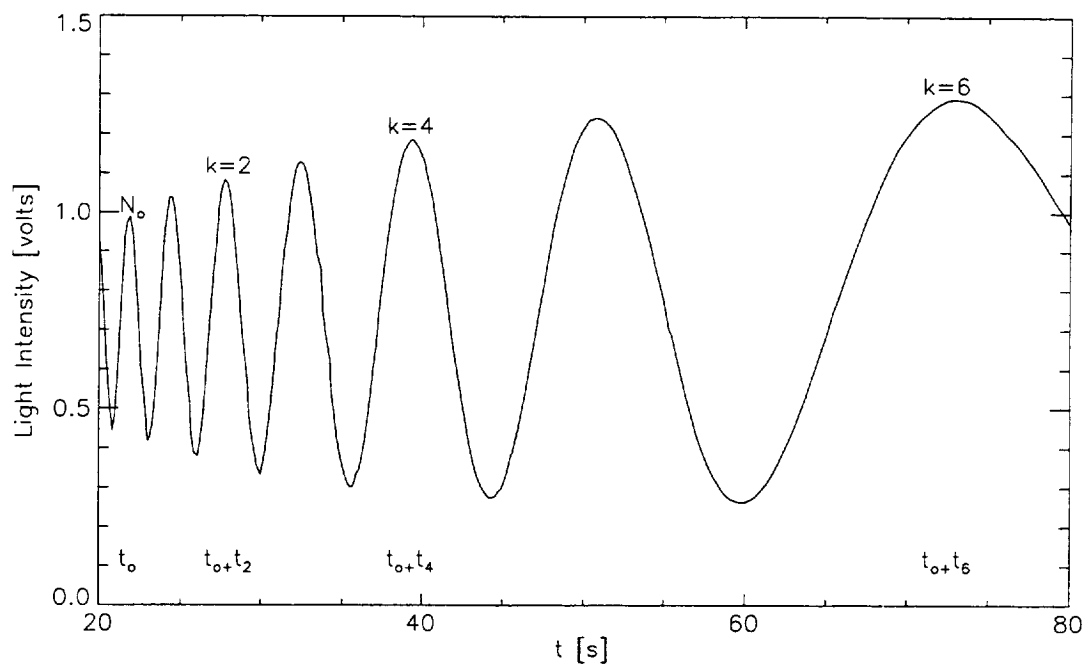
Figure 7. Selection of reference fringe and time from LISF fringe record.
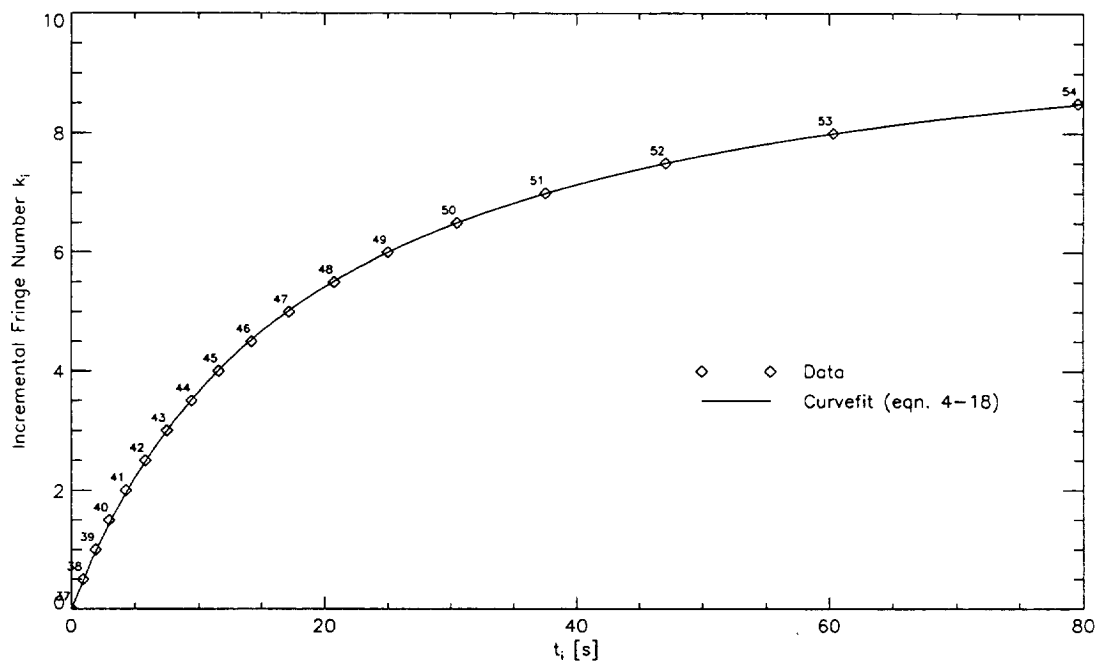
Figure 8. Curvefit of the incremental fringe number versus time data using the "incremental-peak method."

Air flow ▶
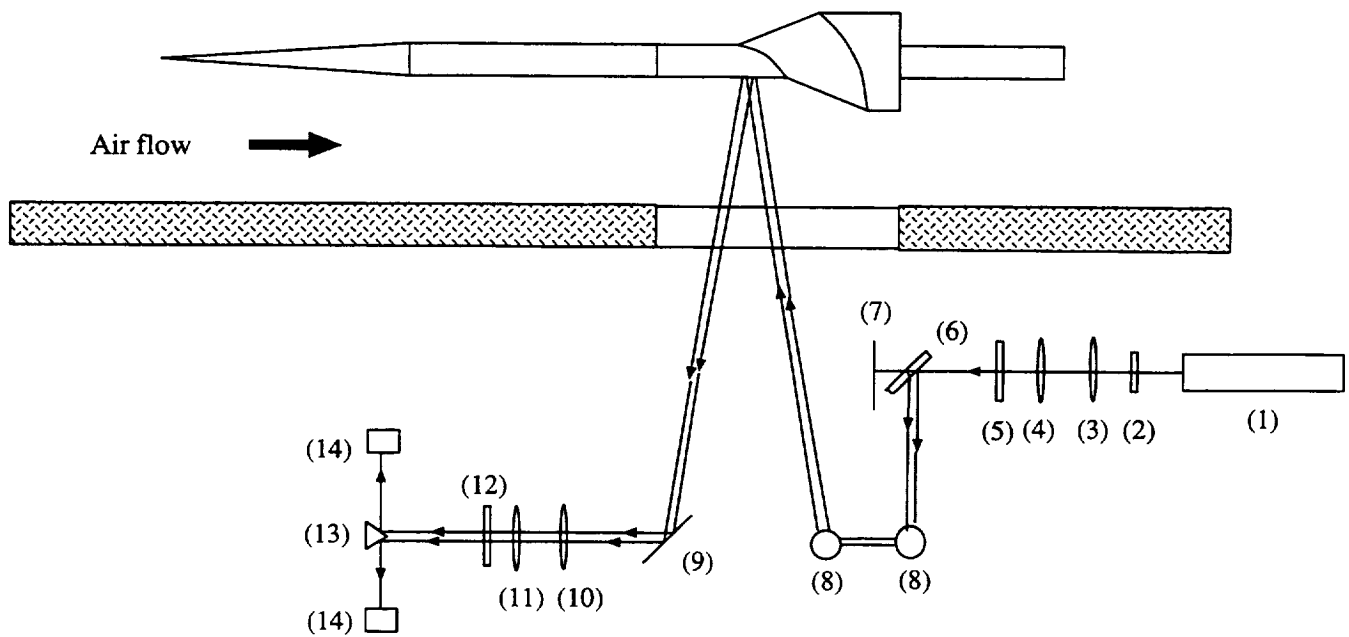
(1) 5.0 mW helium-neon laser
(2) Spatial filter
(3) Focusing lens
(4) Focusing lens
(5) Neutral density filter
(6) Interferometric flat
(7) Beam stop

(8) Vertical assembly of mirrors
(9) Mirror
(10) Collimating lens
(11) Focusing lens
(12) 0.6328 micron filter
(13) Reflective prism
(14) Photodiodes

Figure 9. Schematic of HRC-1 laser interferometry skin friction meter.
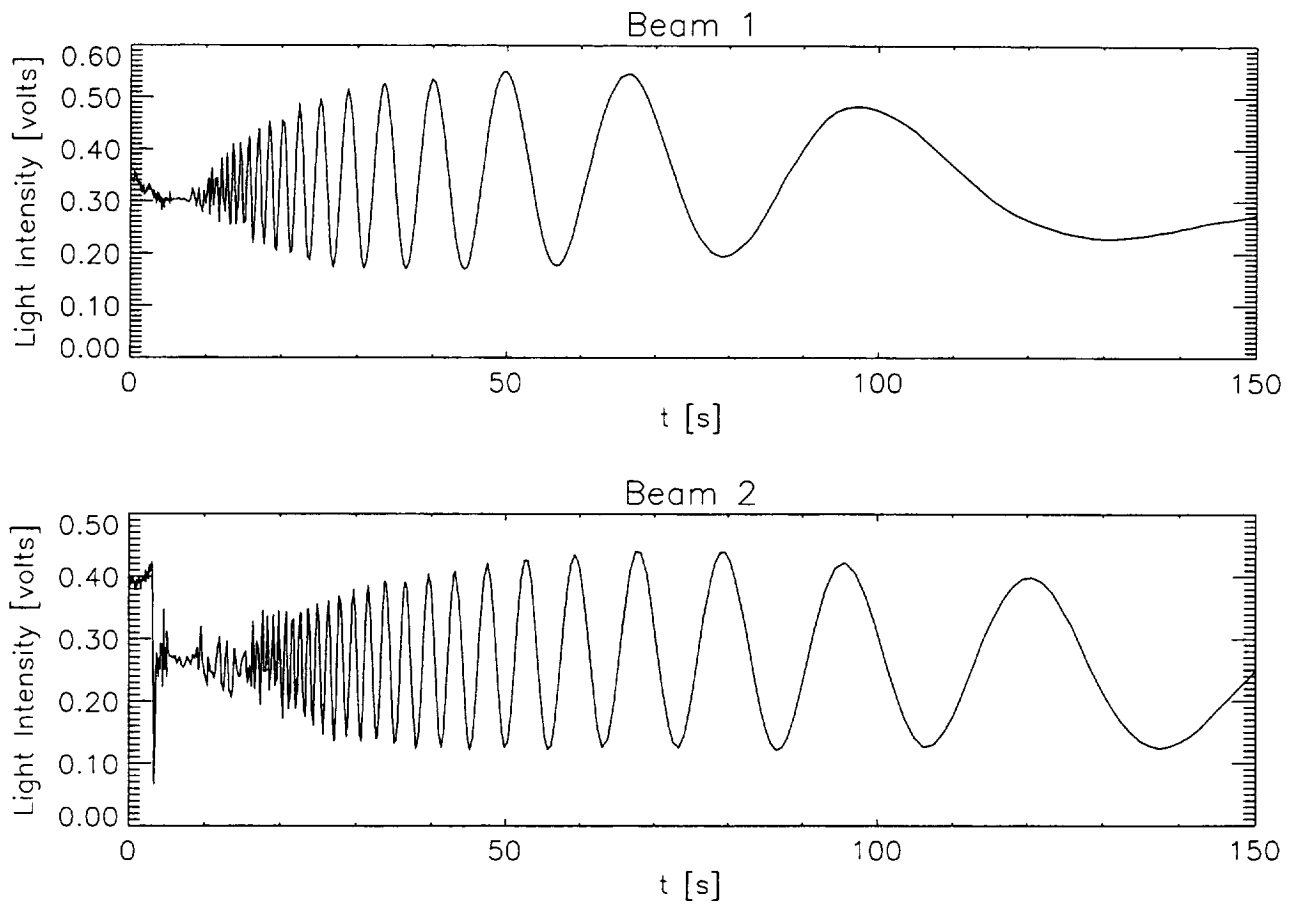
Figure 10. Typical fringe record of dual-beam LISF meter.
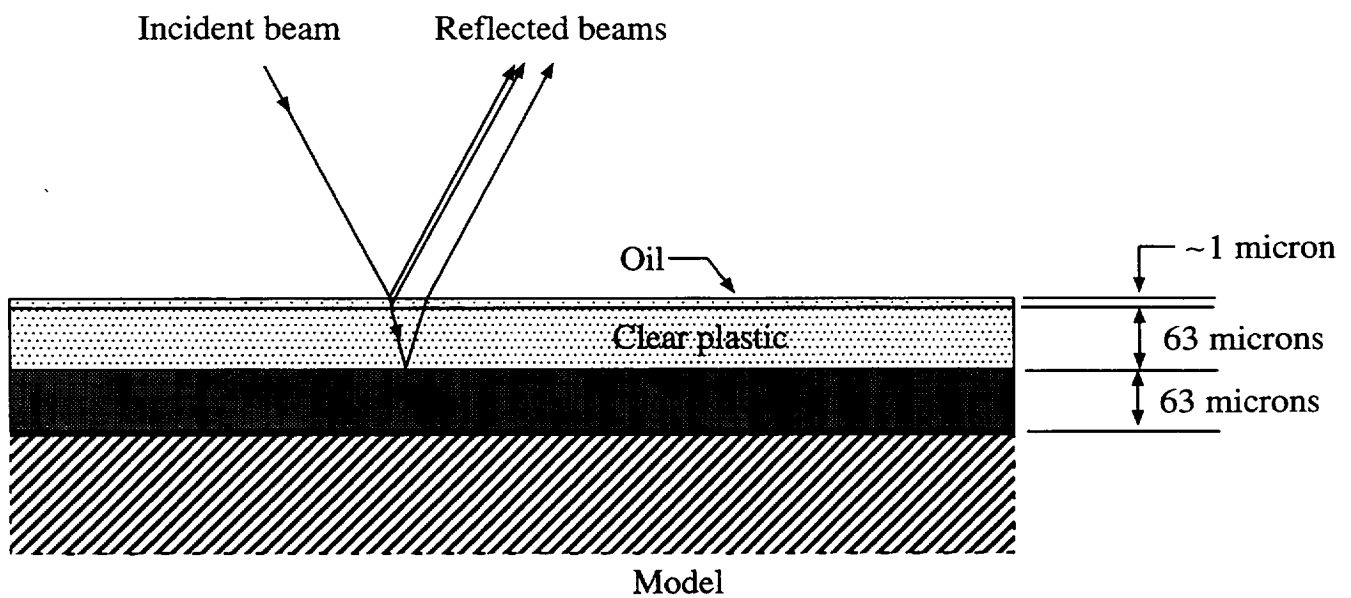
Figure 11. Detail of model surface covered with Monokote and plastic.
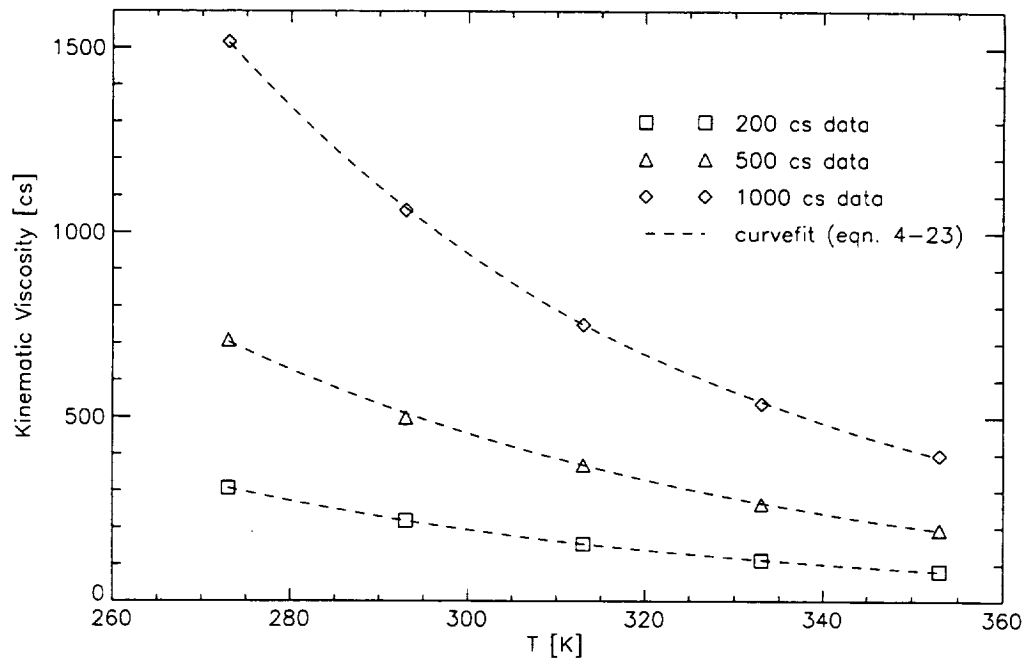
Figure 12. Curvefit of measured viscosity data for Dow Corning 200 Fluids.
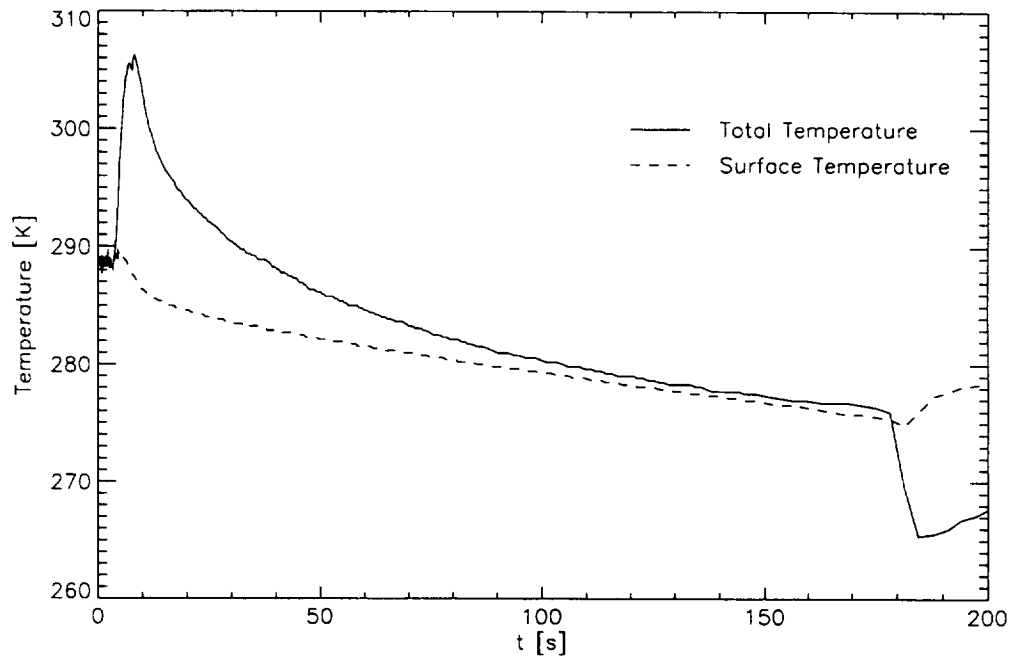
Figure 13. Total and surface temperature distributions during a typical run.

C-2
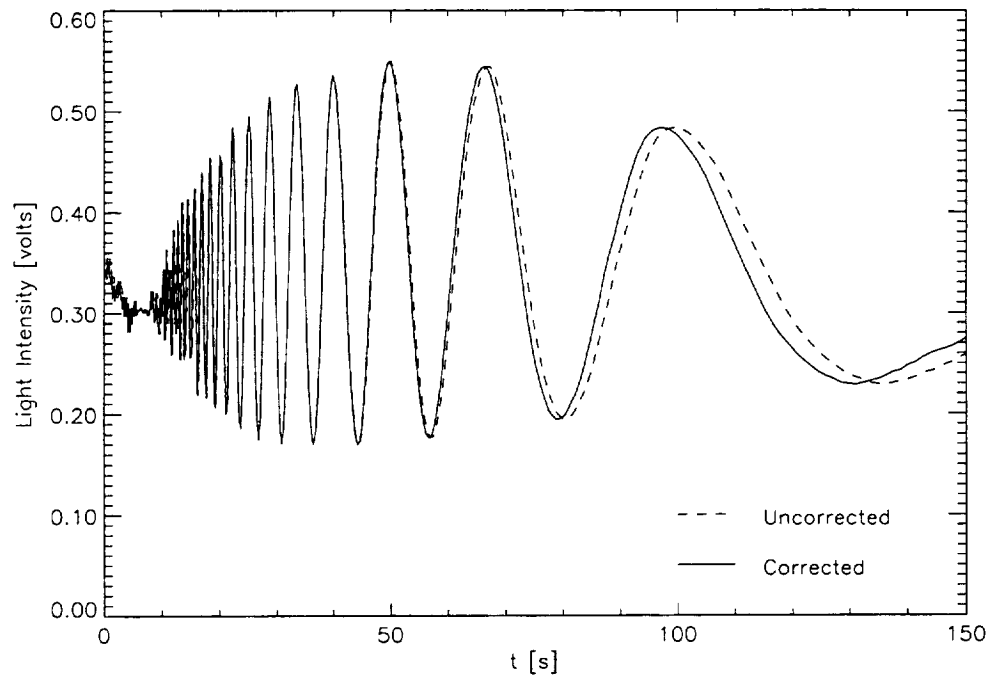
Figure 14. Comparison of uncorrected fringe record to temperature corrected fringe record.
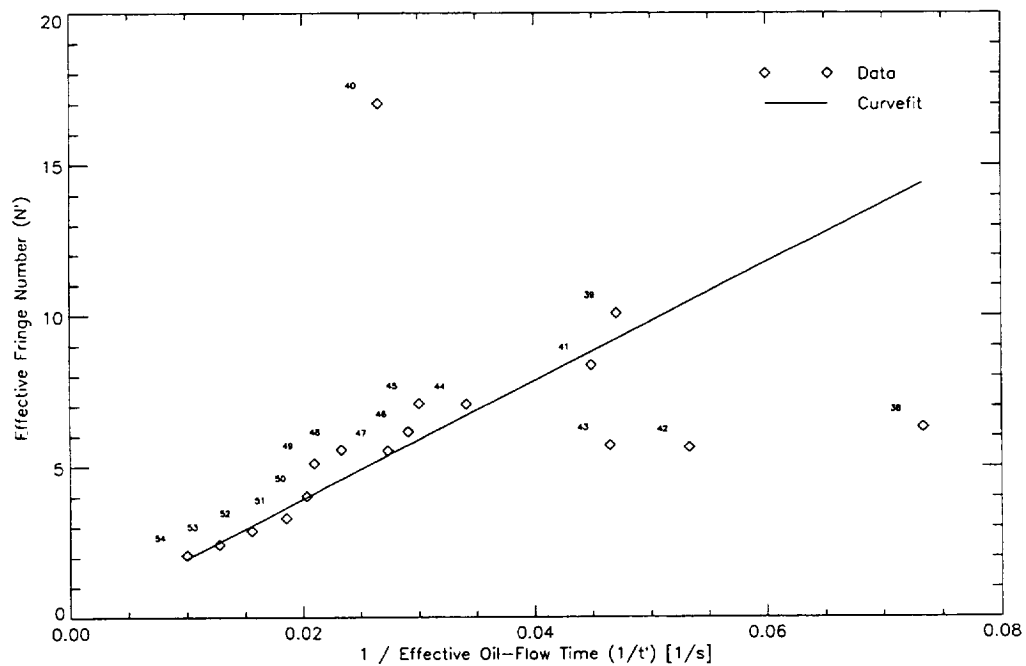
Figure 15. Curvefit of effective fringe number versus time from calculations based on the two previous fringes.

93
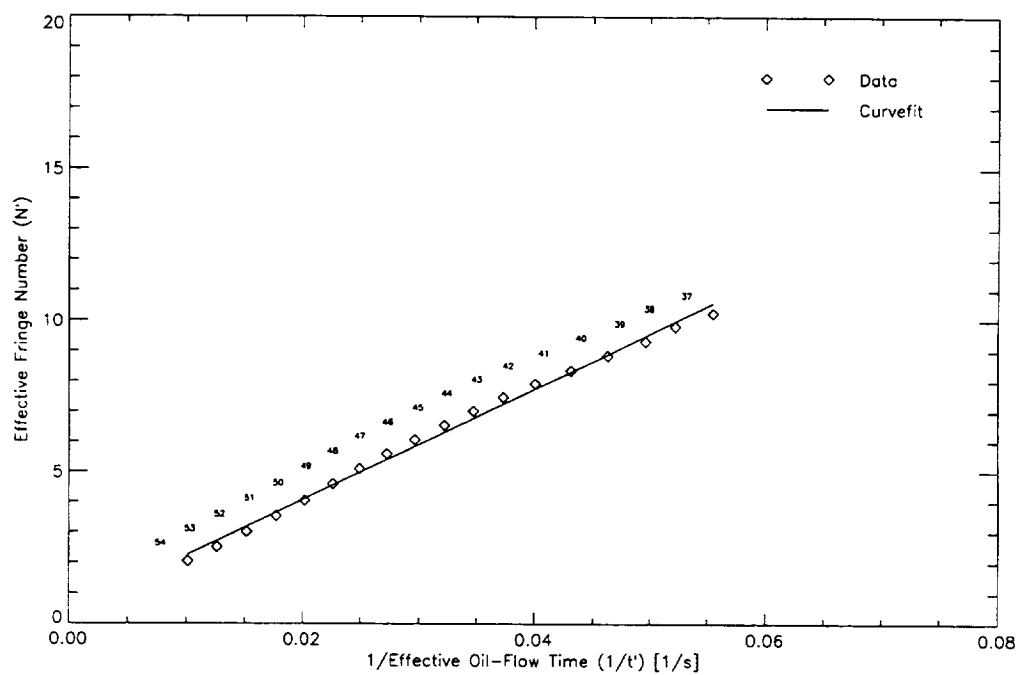
Figure 16. Curvefit of effective fringe number versus time from calculations using the "total-peak method."
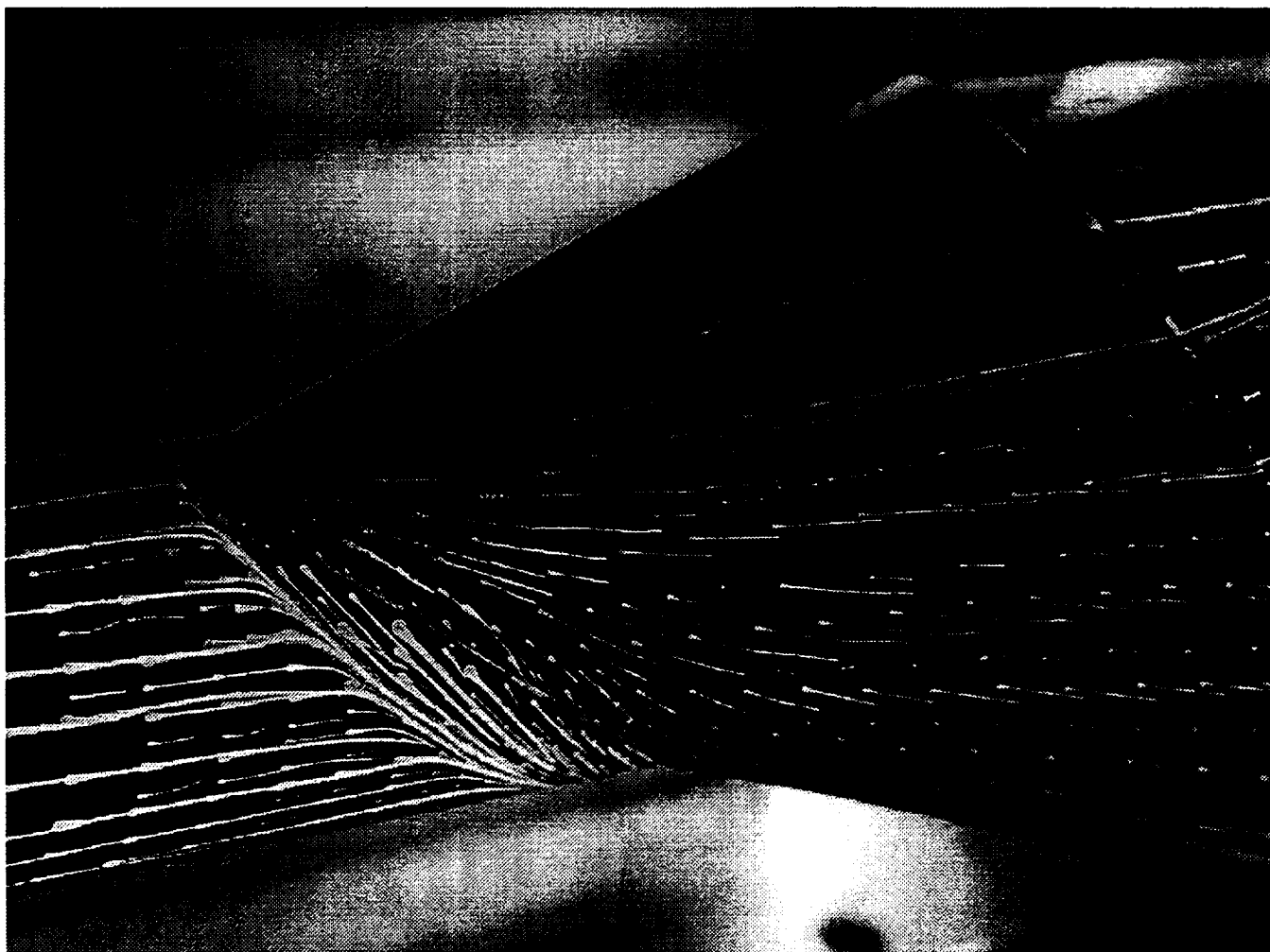
Figure 17. Post-run photograph of model with oil-streak pattern (view from $\phi \approx 45°$).
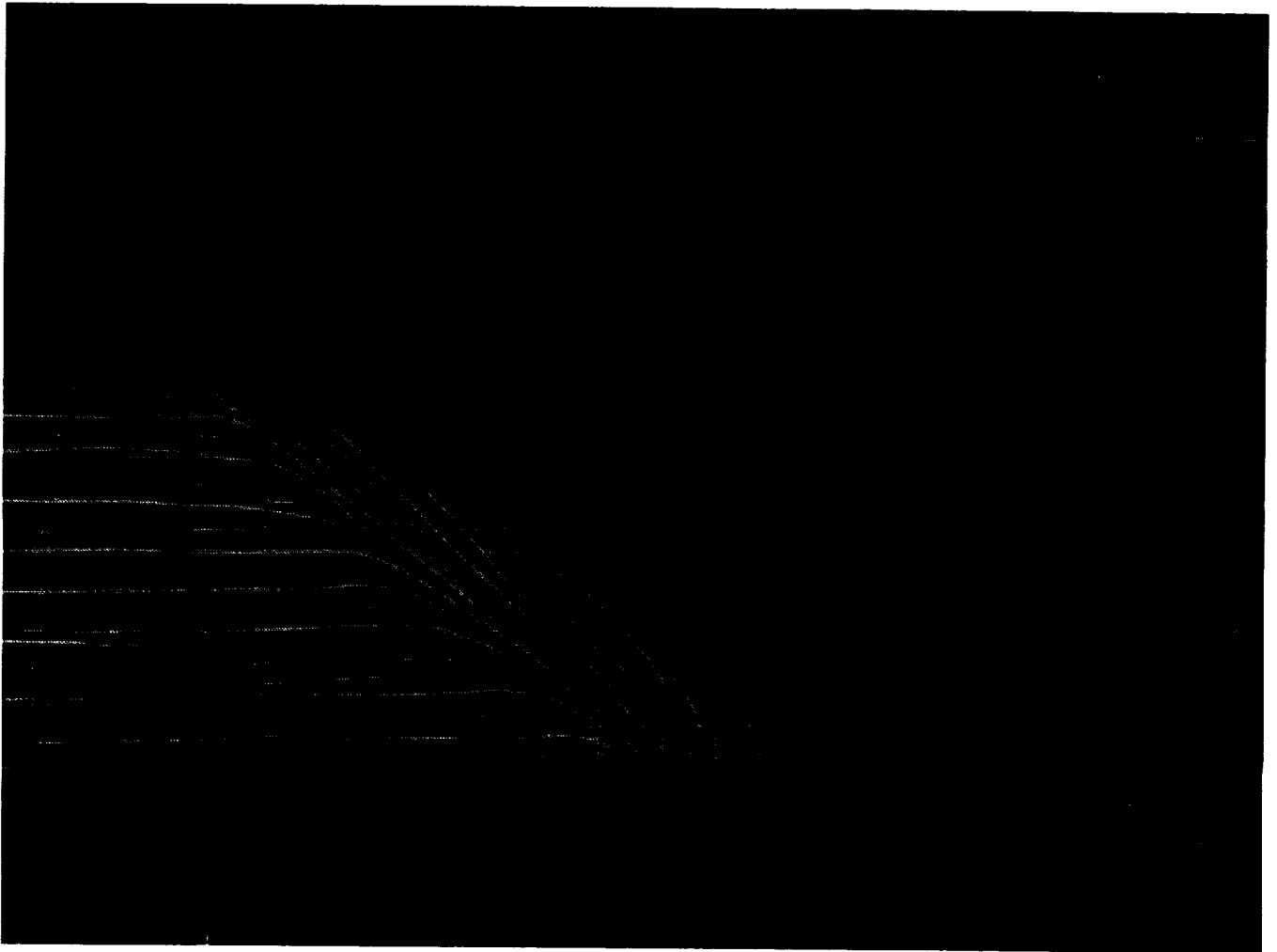
Figure 18. Post-run photograph of model with oil-streak pattern (view from $\phi \approx 90°$).
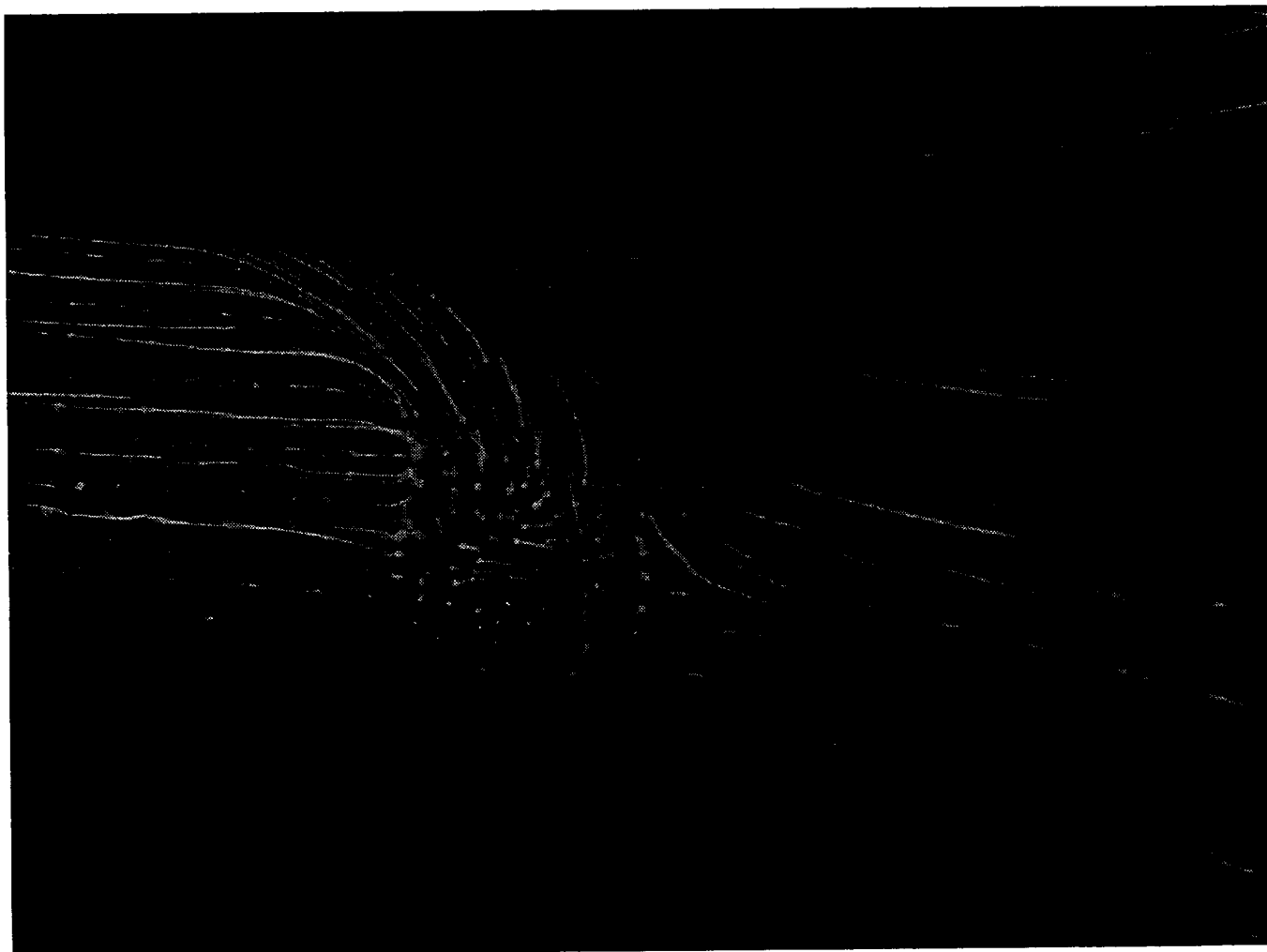
Figure 19. Post-run photograph of model with oil-streak pattern (view from $\phi \approx 180°$).

Figure 20. Post-run photograph of model with oil-streak pattern (view from $\phi \approx 165°$).
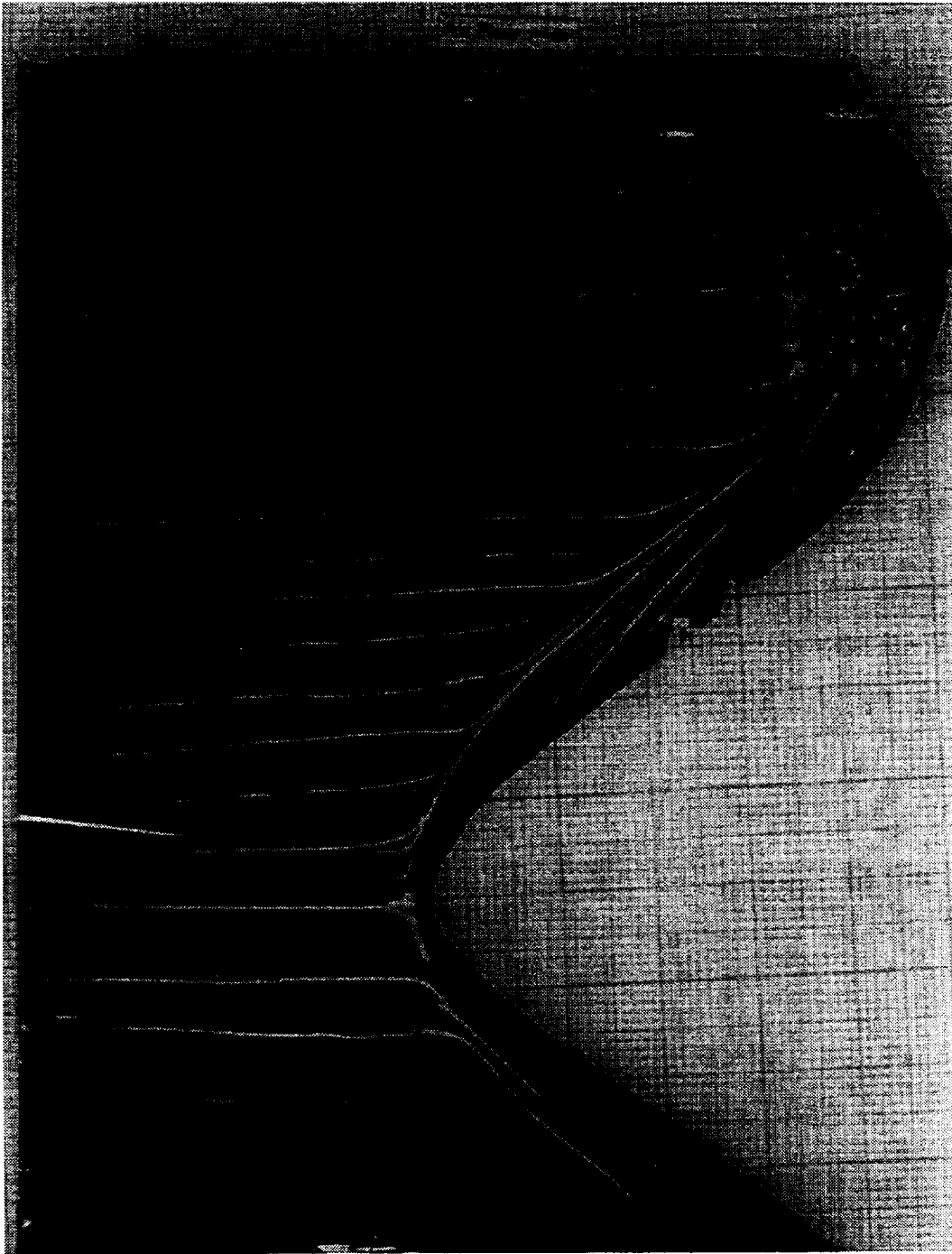
Figure 21. Unwrapped Monokote section from cylinder.
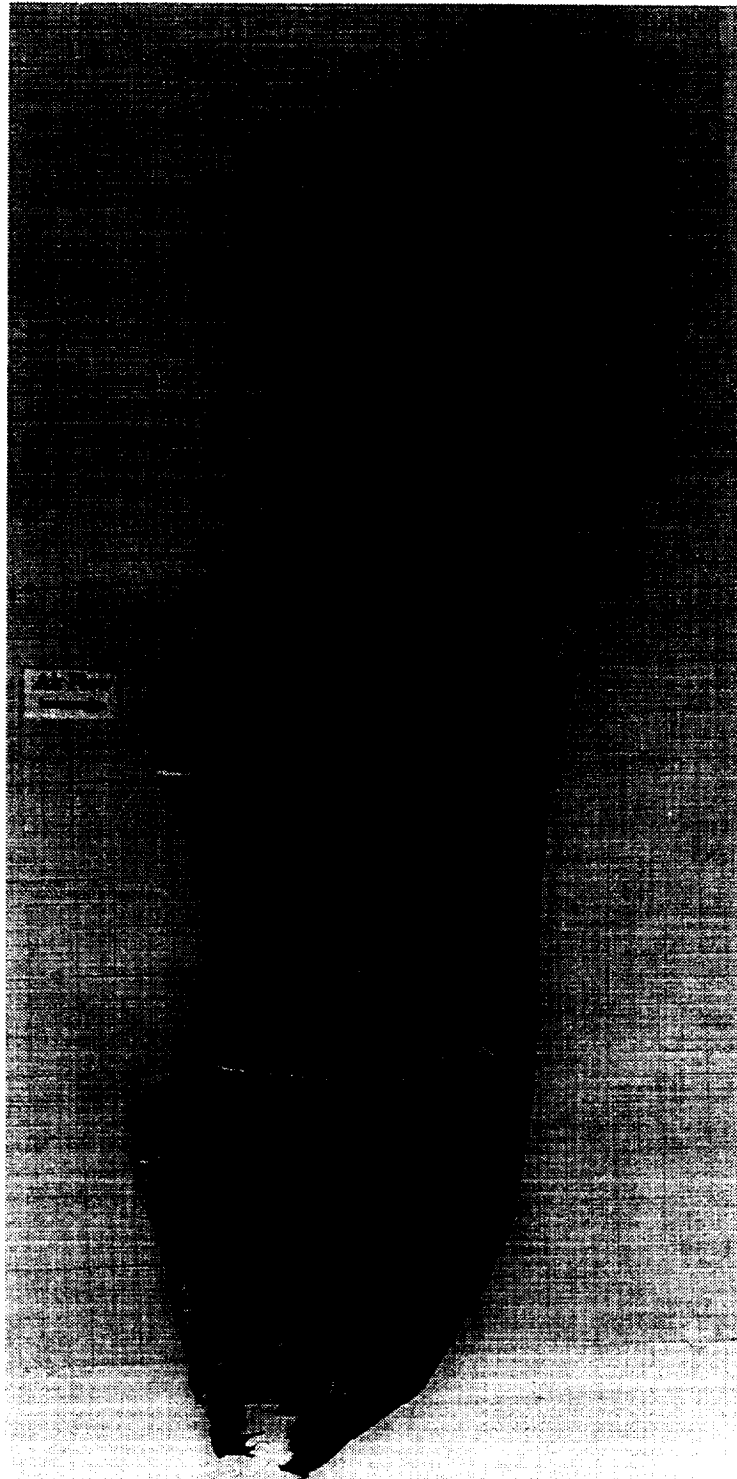
Figure 22. Unwrapped Monokote section from flare ramp.
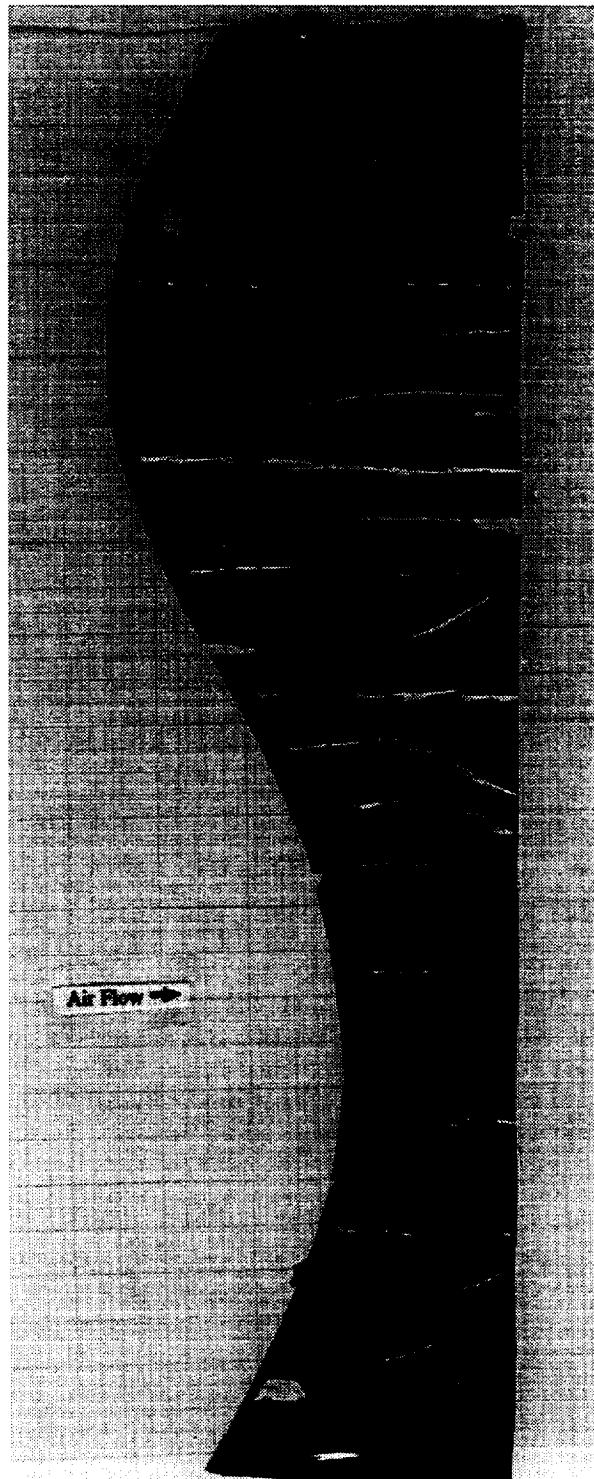
Figure 23. Unwrapped Monokote section from flare afterbody.
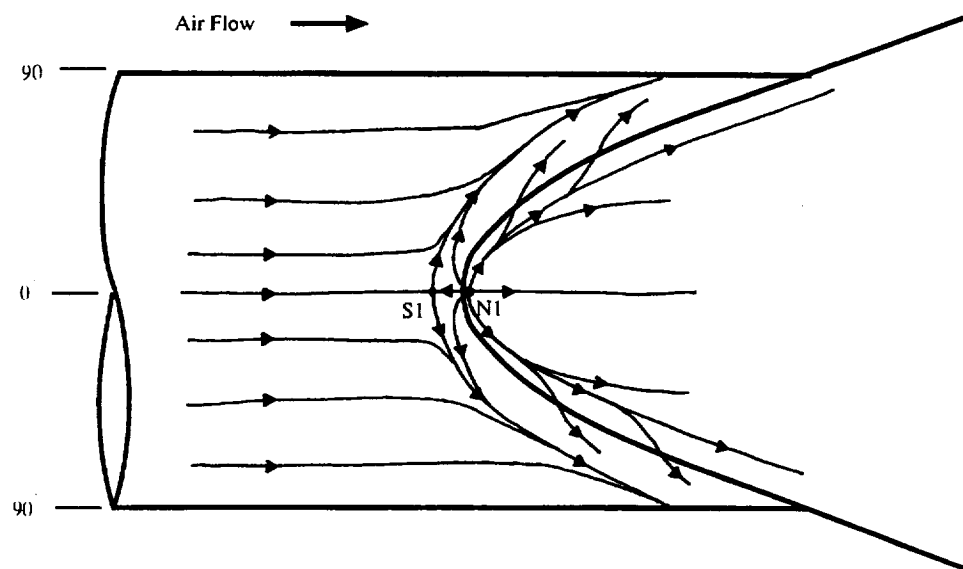
Figure 24. Postulated skin-friction line pattern.
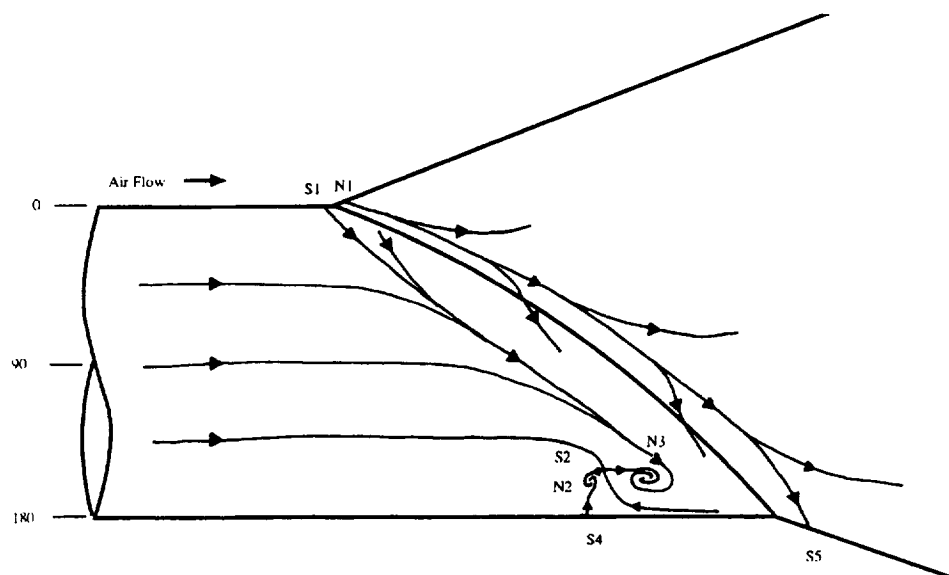
Figure 24. Continued.
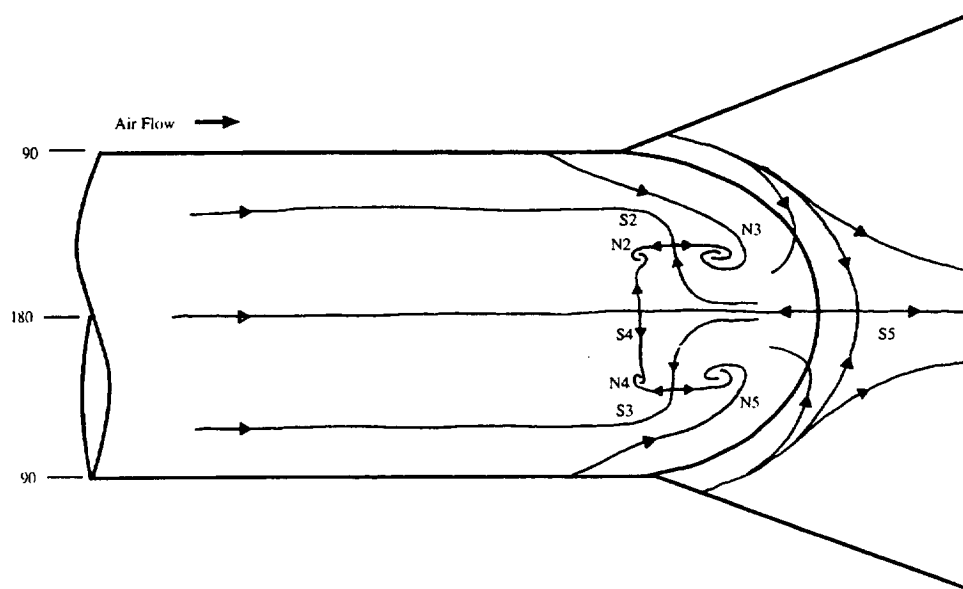
Figure 24. Concluded.
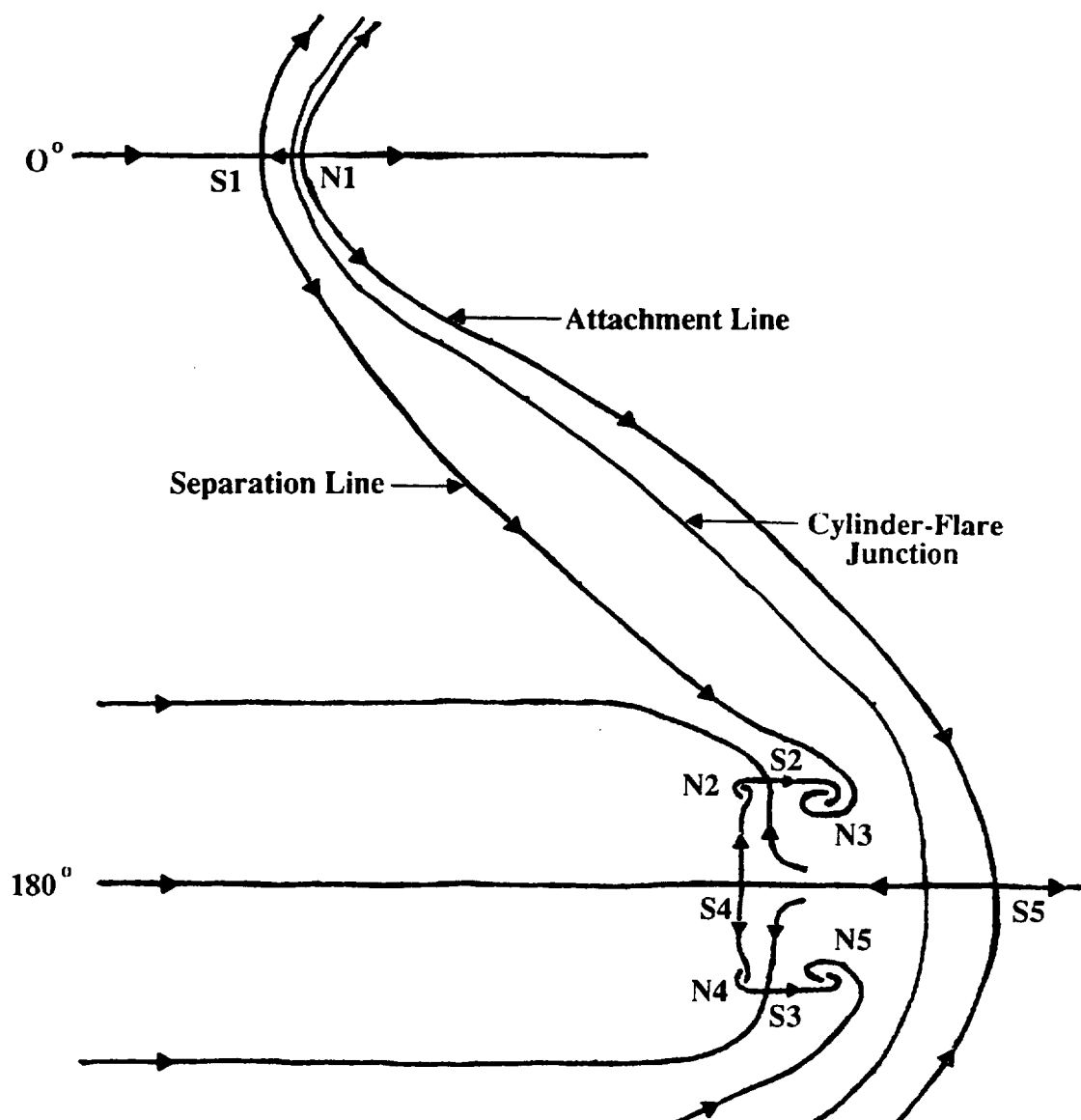
Figure 25. Unwrapped postulated skin-friction line pattern.
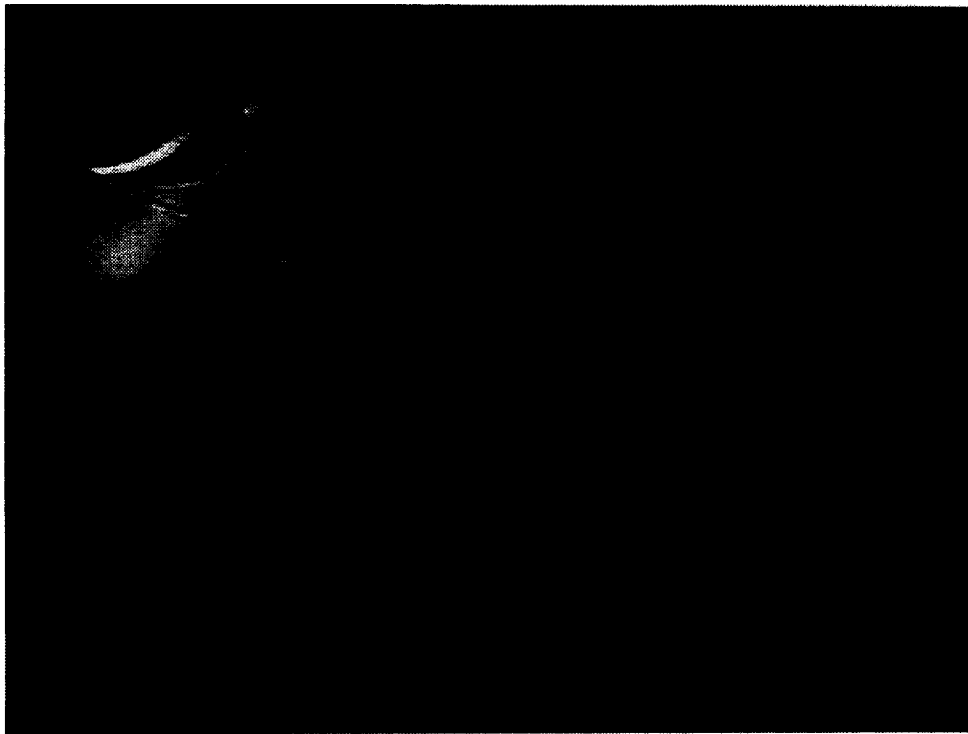
Figure 26. Laser light sheet located at $x = 5.7$ cm (view from $\phi \approx 150°$).

Figure 27. Laser light sheet located at $x = 7.0$ cm (view from $\phi \approx 150°$).

Figure 28. Laser light sheet located at $x = 8.3$ cm (view from $\phi \approx 150°$).

Figure 29. Laser light sheet located at $x = 9.5$ cm (view from $\phi \approx 150°$).
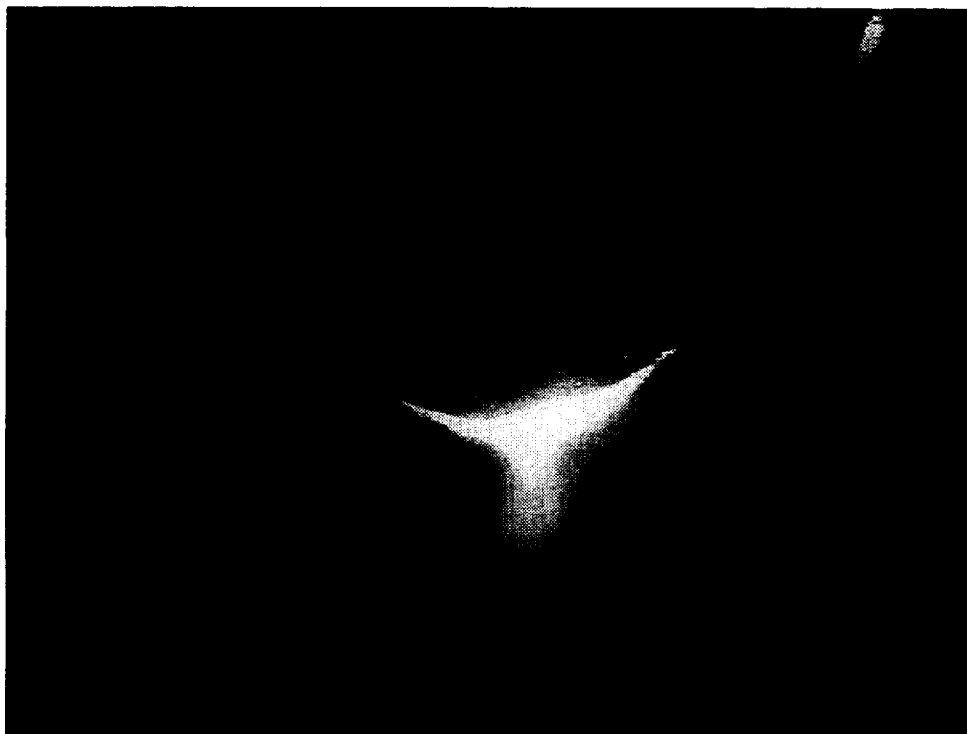
Figure 30. Laser light sheet located at $x = 10.8$ cm (view from $\phi \approx 150°$).

Figure 31. Laser light sheet located at $x = 13.4$ cm (view from $\phi \approx 150°$).
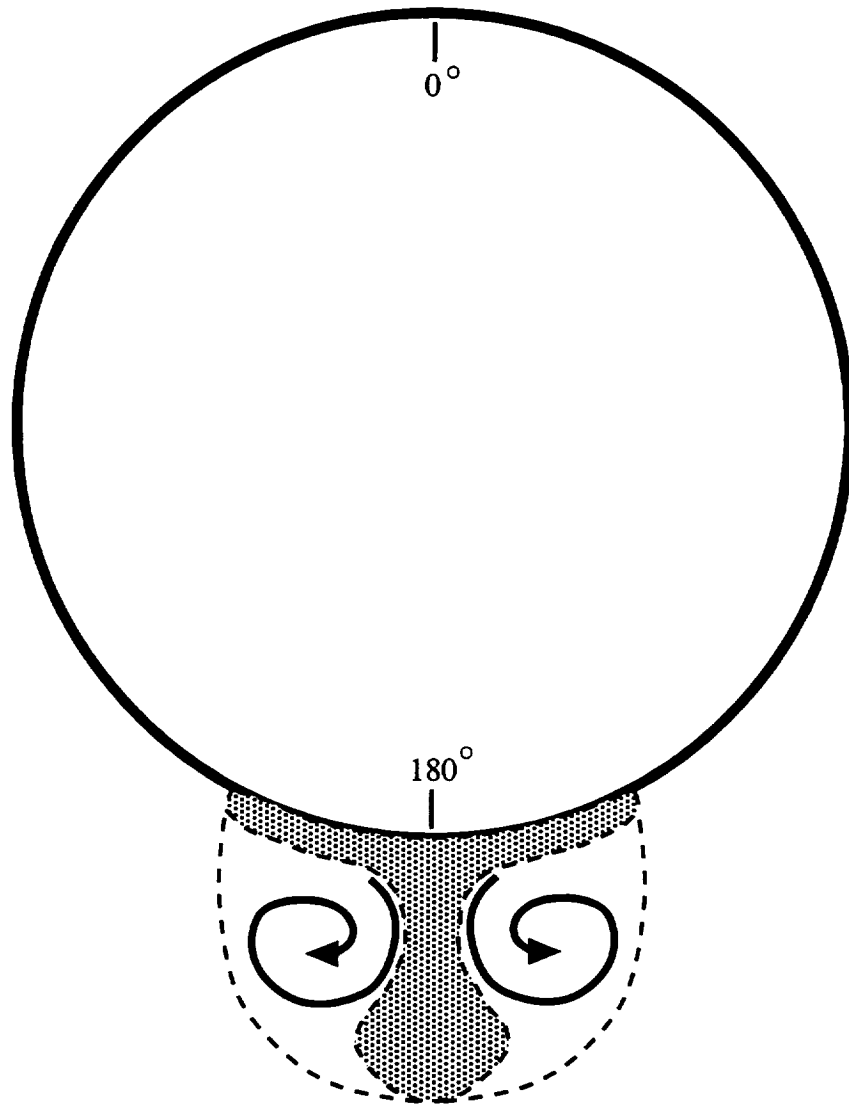
Figure 32. Interpretation of light sheet images along $\phi = 180°$ (looking downstream).

SHOCK WAVE

AIR FLOW →

δ

0°

90°

180°

δ
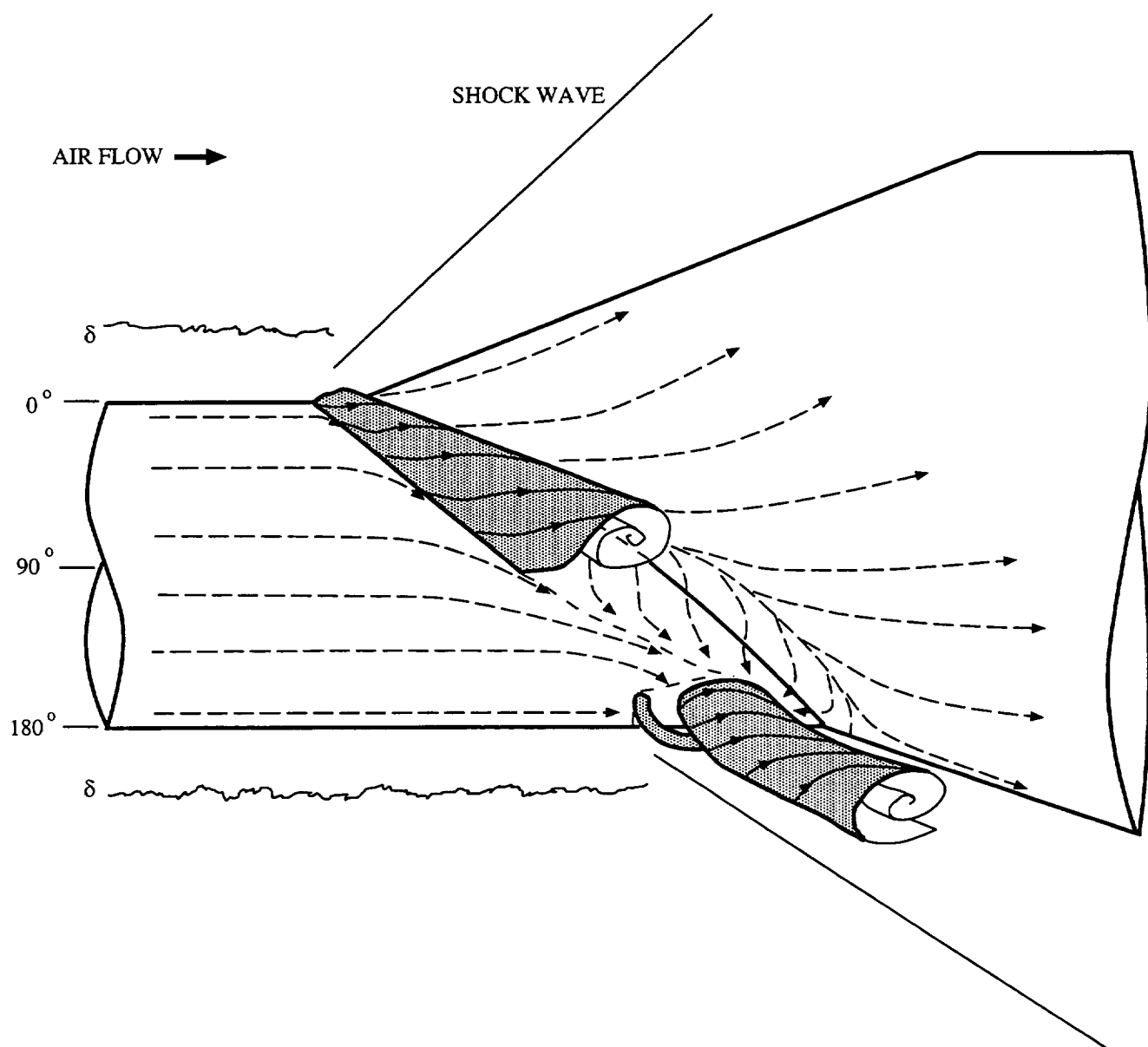
Figure 33. Postulated flow structure.

109
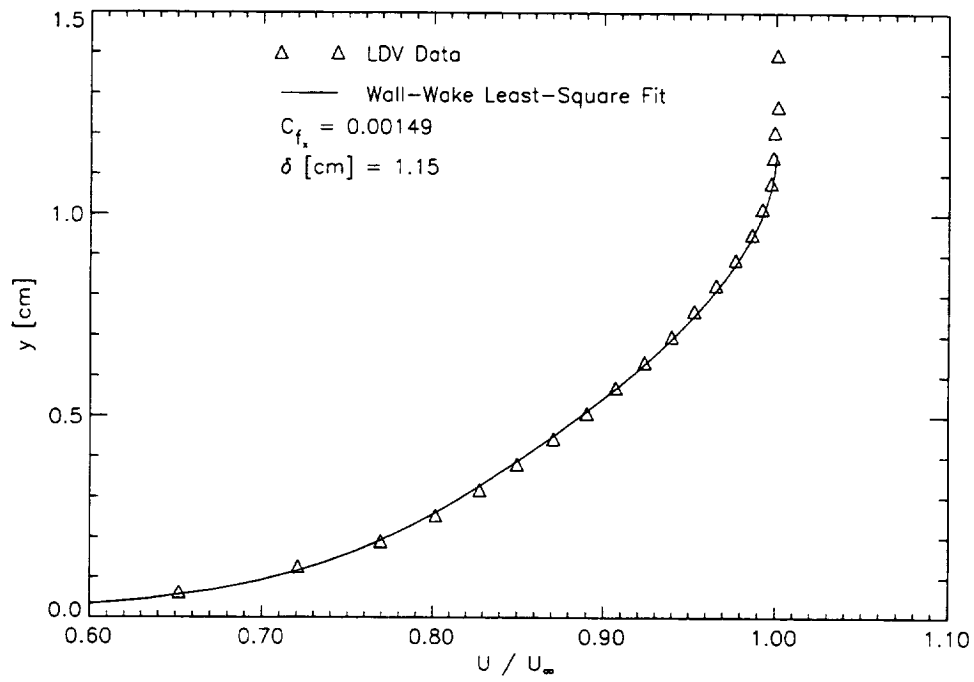
Figure 34. Mean-velocity profile in undisturbed boundary layer.
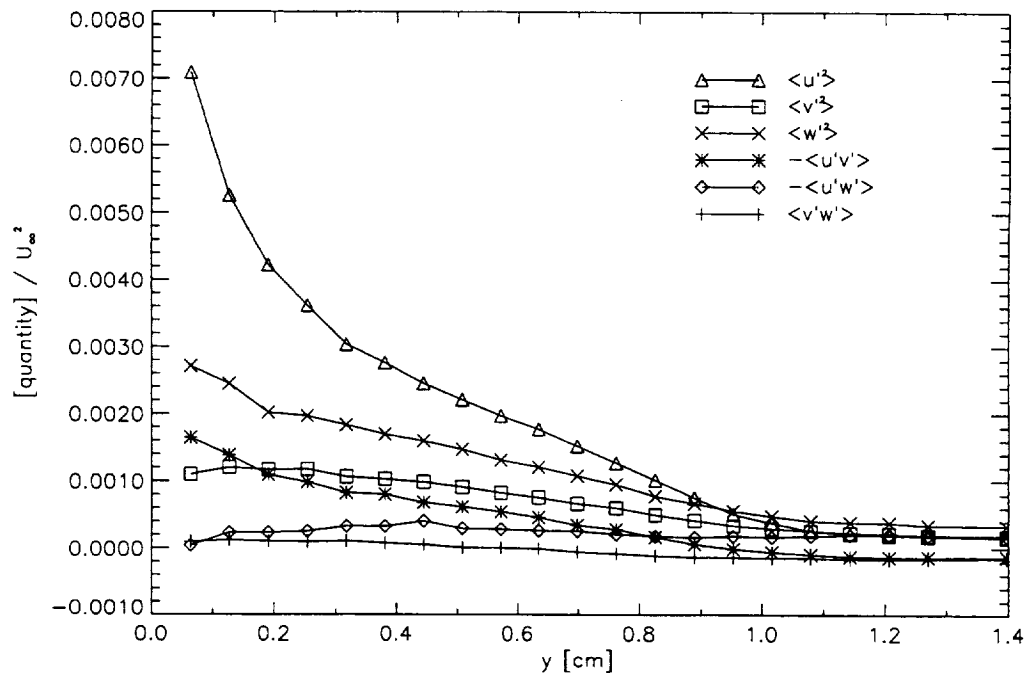
Figure 35. 3-D LDV turbulence measurements in undisturbed boundary layer.

110
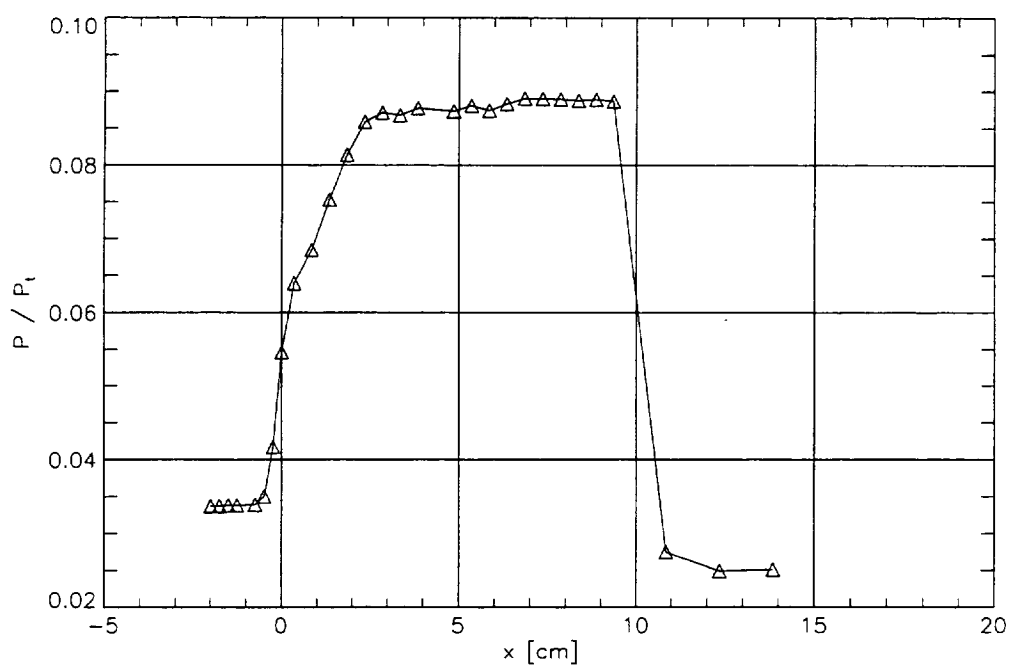
Figure 36. Surface pressure distribution along $\phi = 0°$.
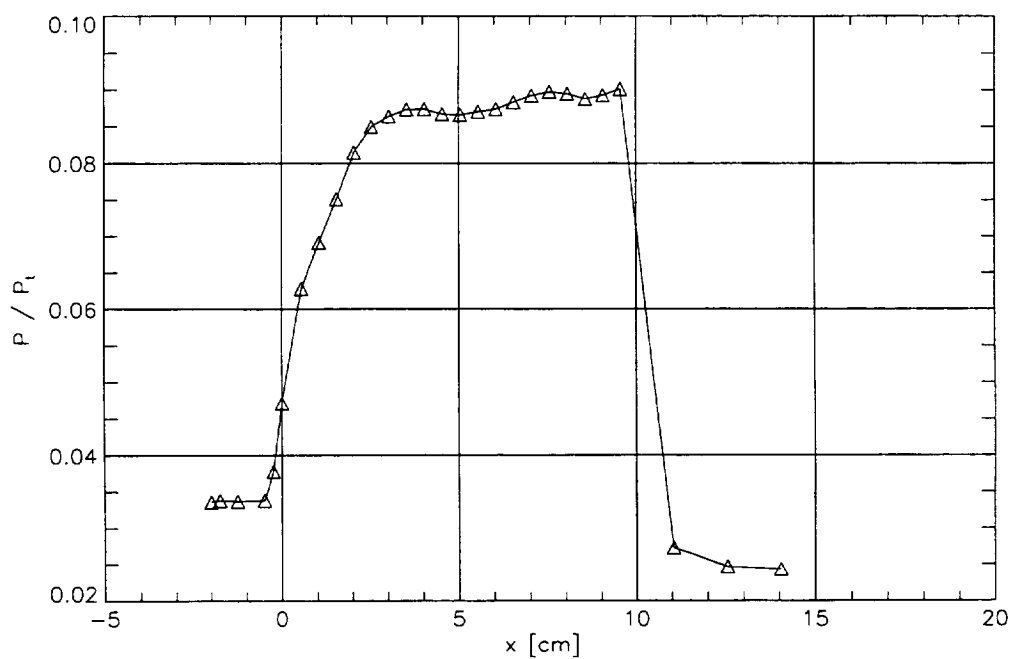
Figure 37. Surface pressure distribution along $\phi = 15°$.

111
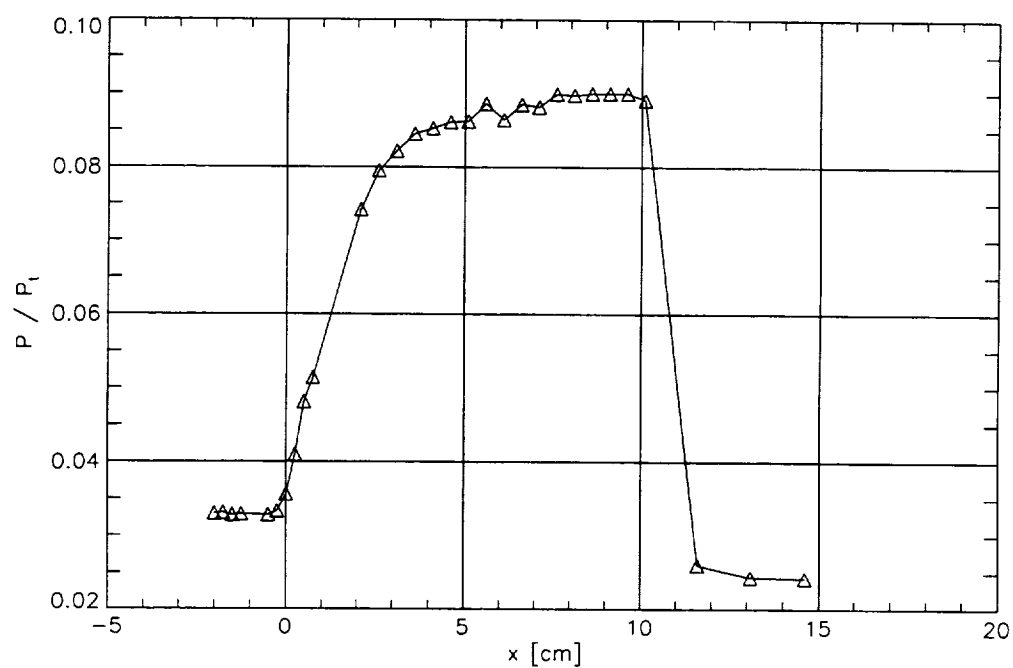
Figure 38. Surface pressure distribution along $\phi = 30°$.
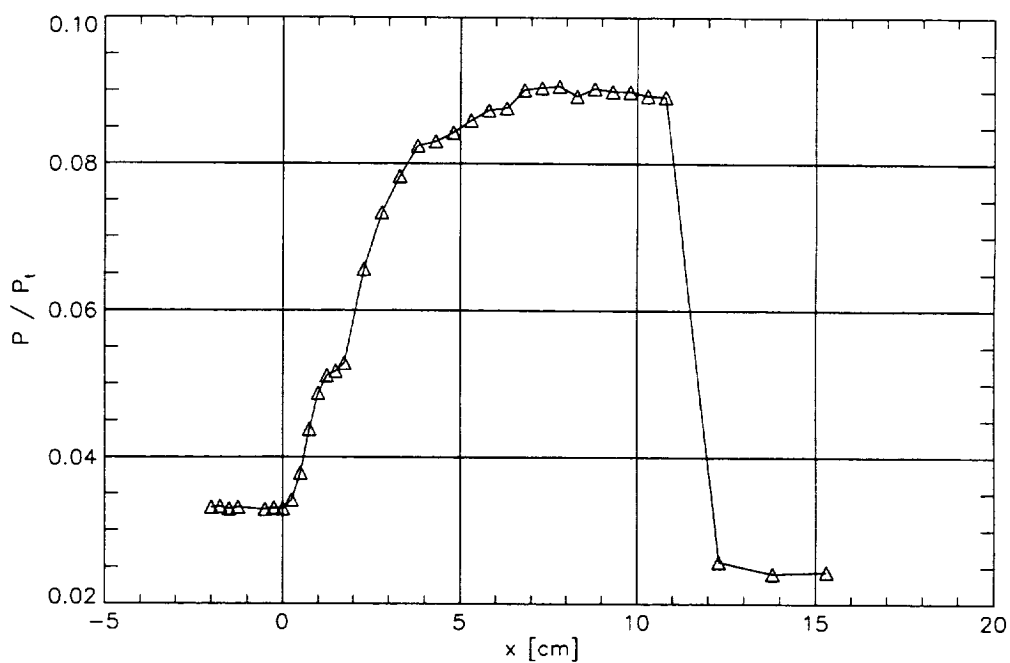
Figure 39. Surface pressure distribution along $\phi = 45°$.
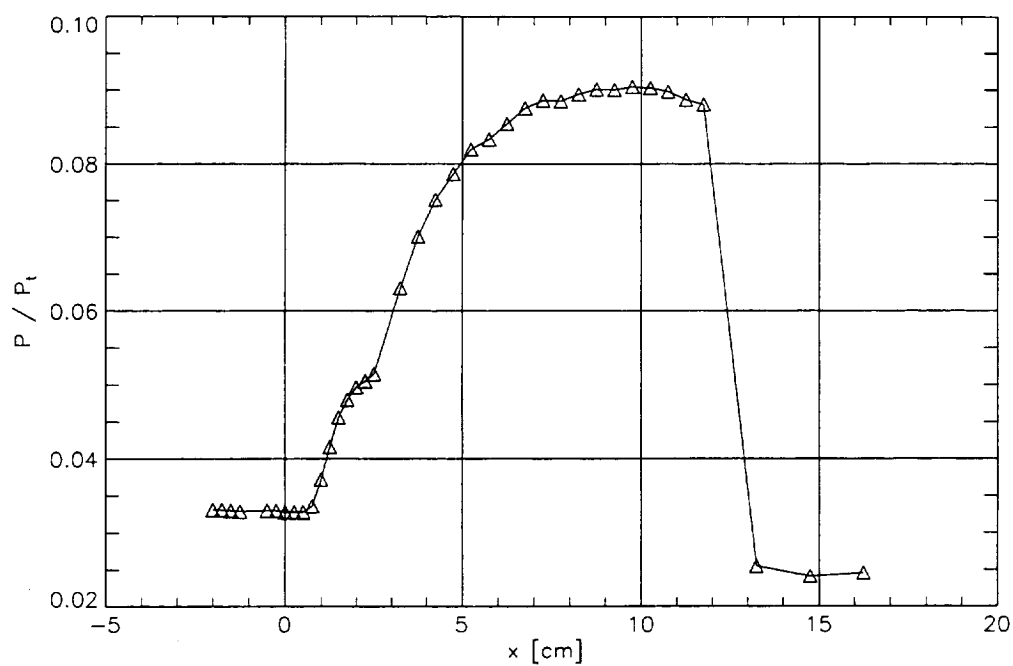
Figure 40. Surface pressure distribution along $\phi = 60°$.
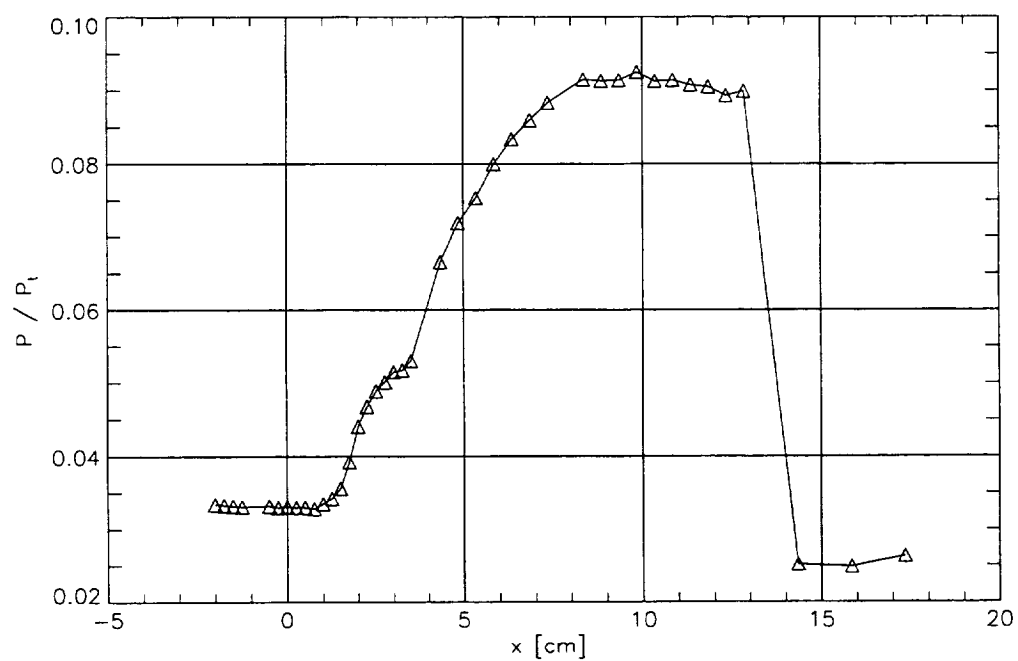
Figure 41. Surface pressure distribution along $\phi = 75°$.

113
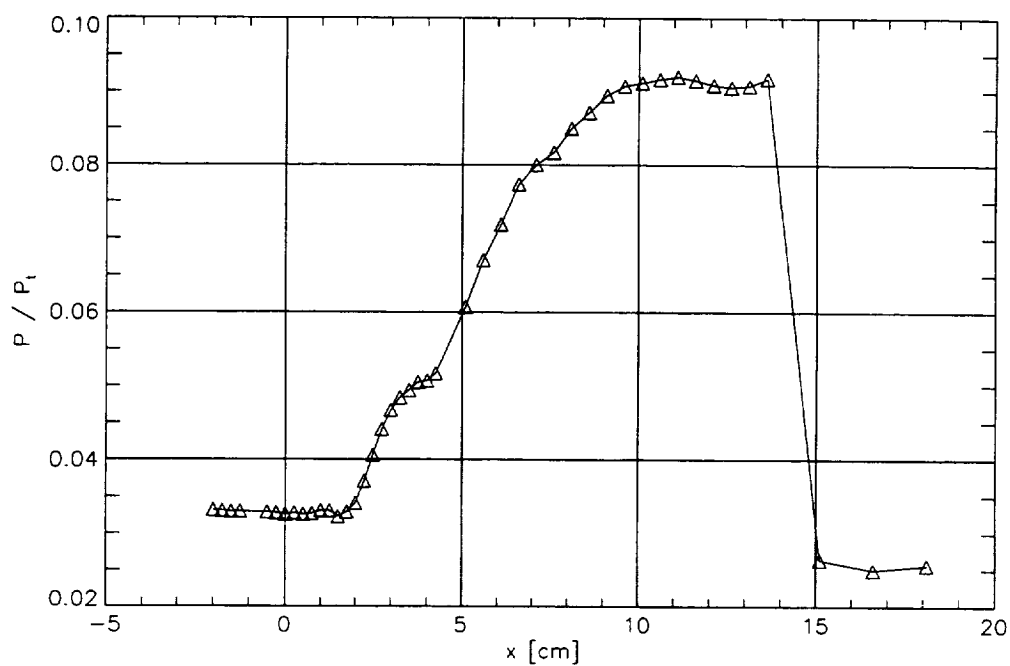
Figure 42. Surface pressure distribution along $\phi = 90°$.
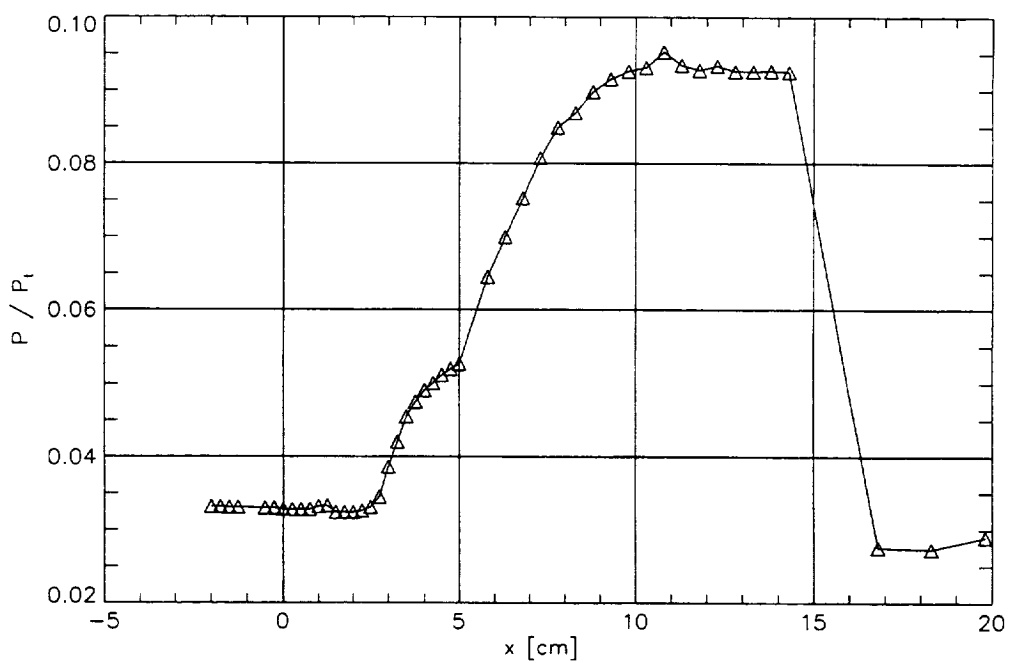
Figure 43. Surface pressure distribution along $\phi = 105°$.

114
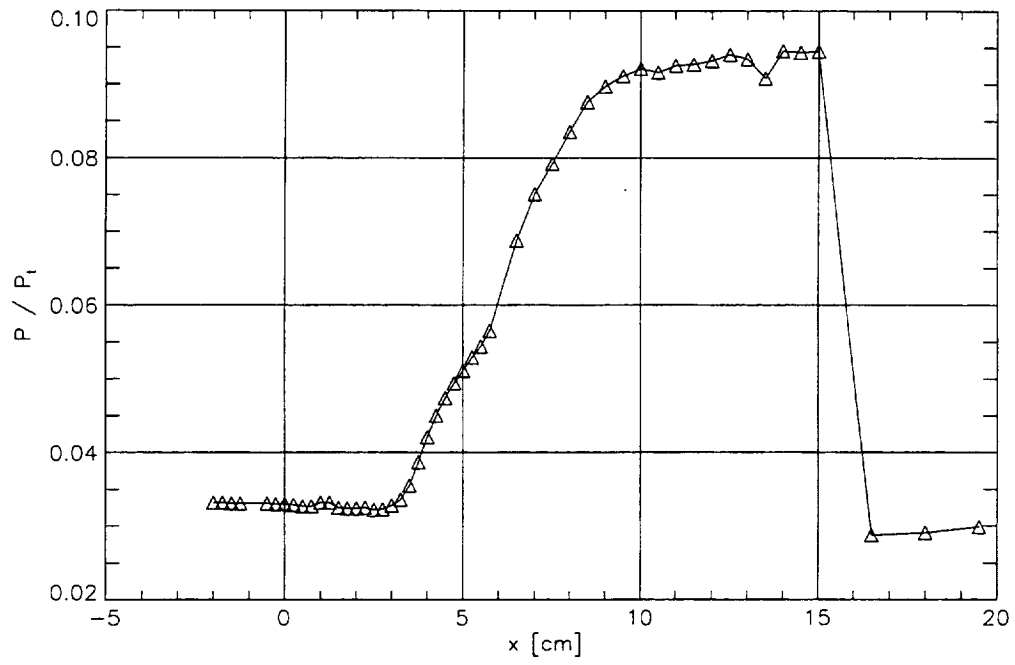
Figure 44. Surface pressure distribution along $\phi = 120°$.
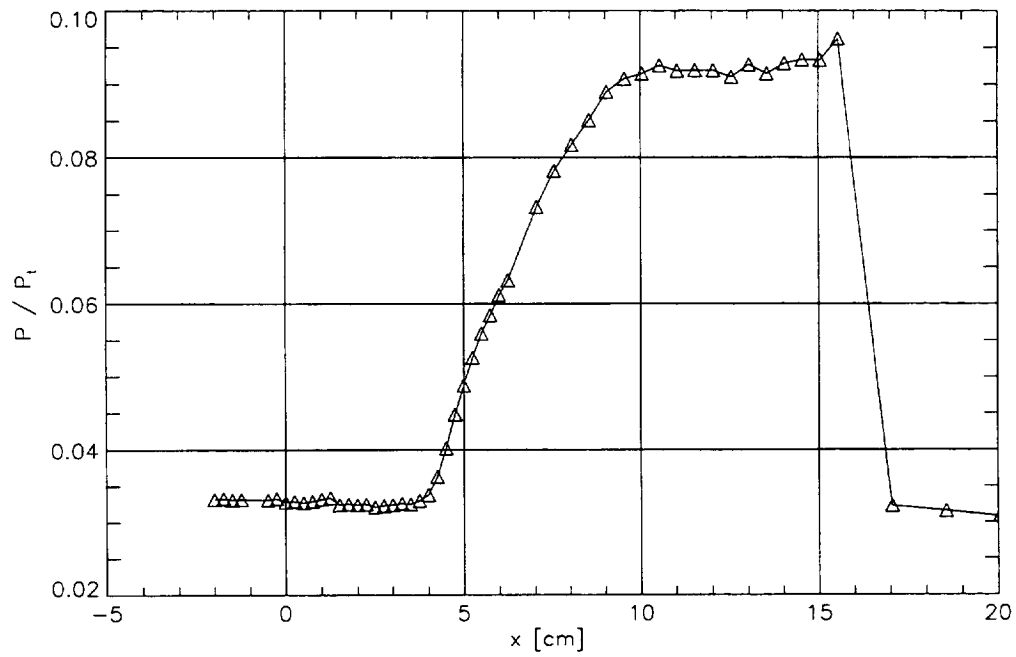
Figure 45. Surface pressure distribution along $\phi = 135°$.
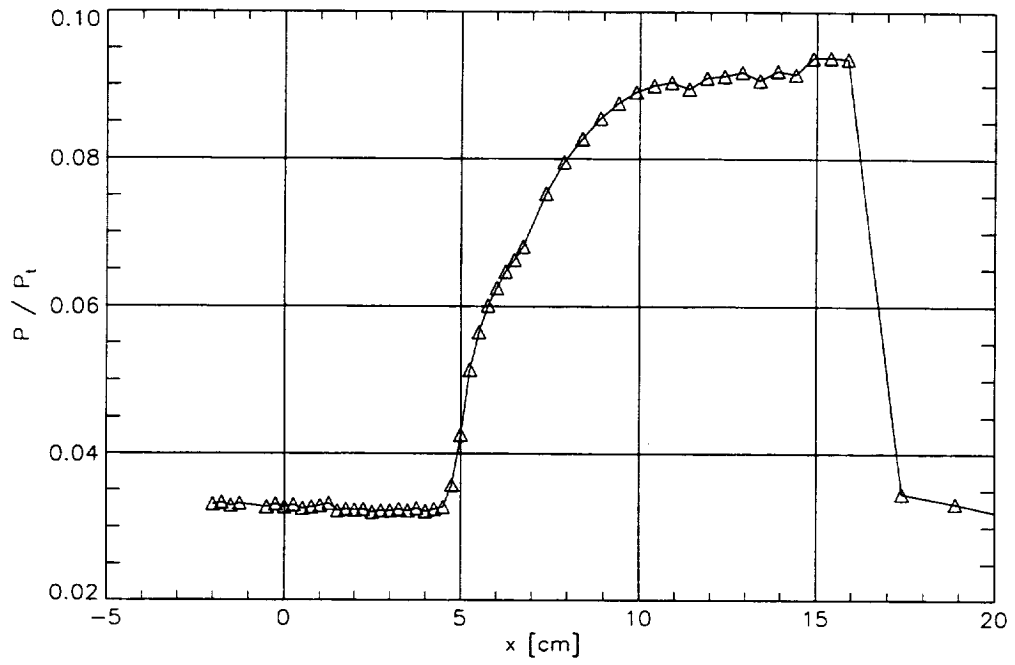
Figure 46. Surface pressure distribution along $\phi = 150°$.
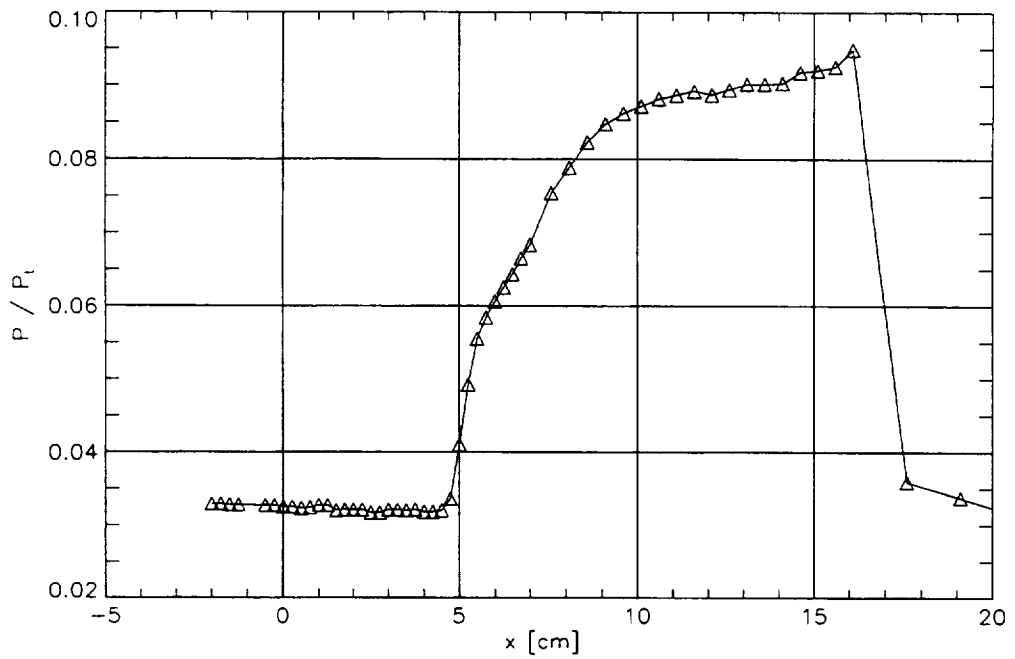
Figure 47. Surface pressure distribution along $\phi = 165°$.
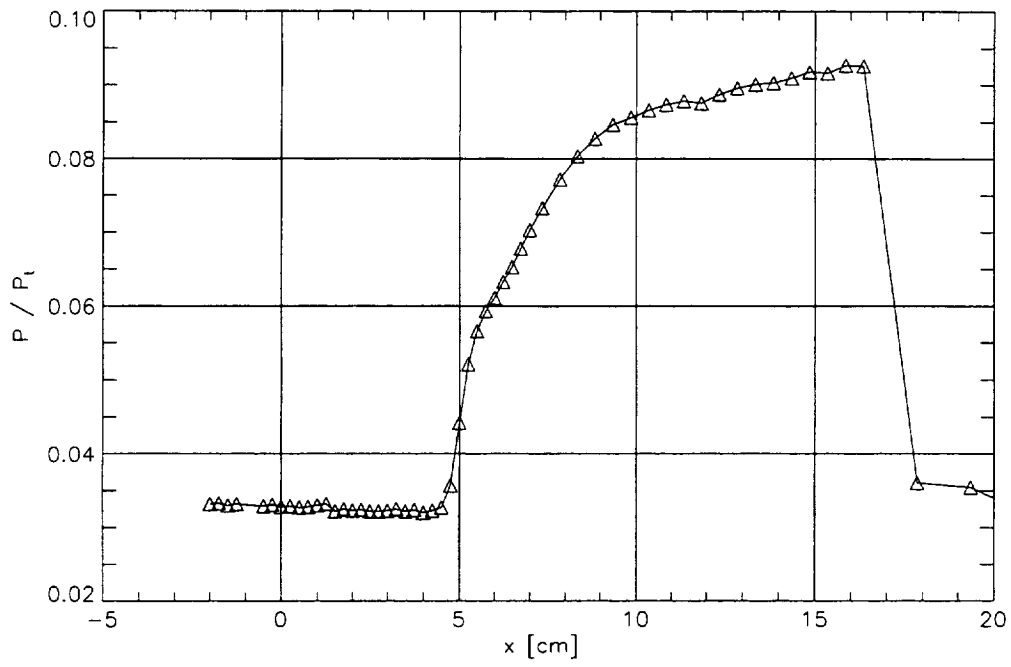
Figure 48. Surface pressure distribution along $\phi = 180°$.
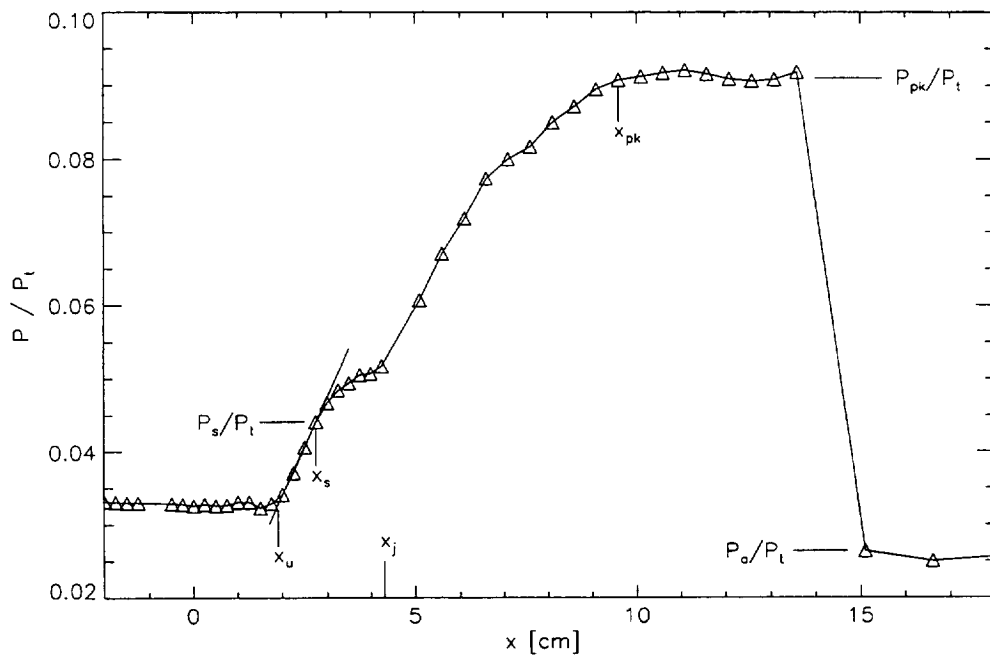
Figure 49. Example pressure distribution.

117
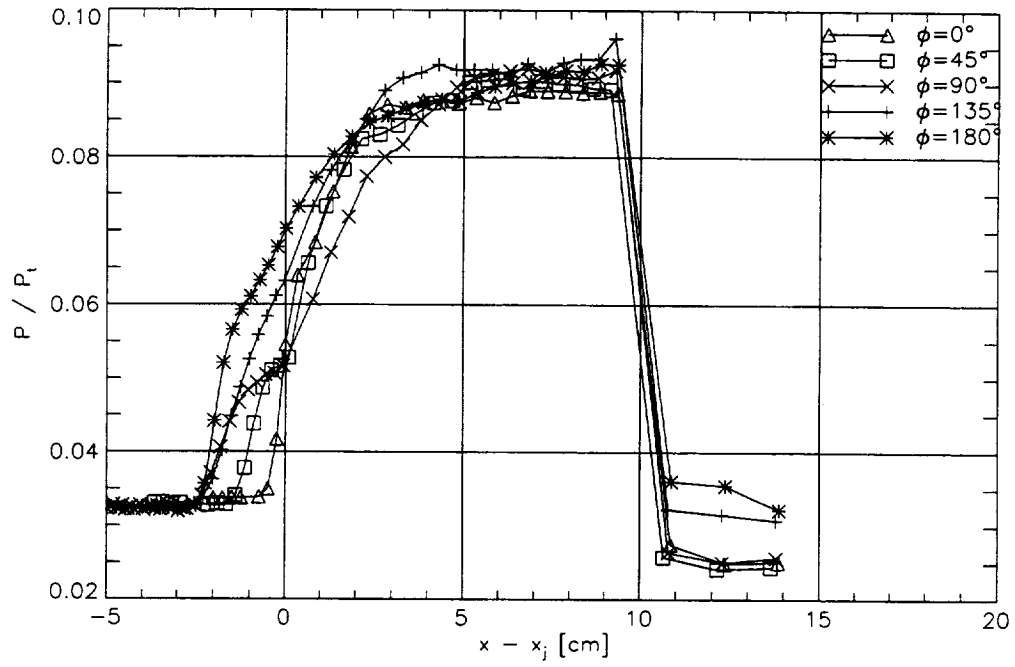
Figure 50. Surface pressure distribution with the cylinder-flare junction along each azimuth coincident.
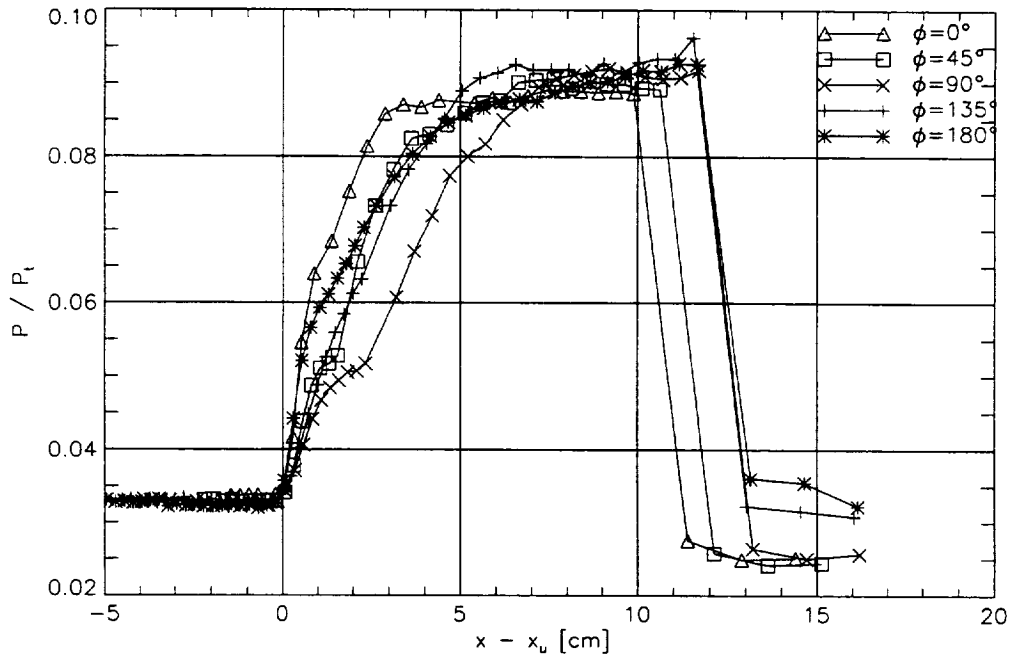
Figure 51. Surface pressure distribution with upstream influence location along each azimuth coincident.

118
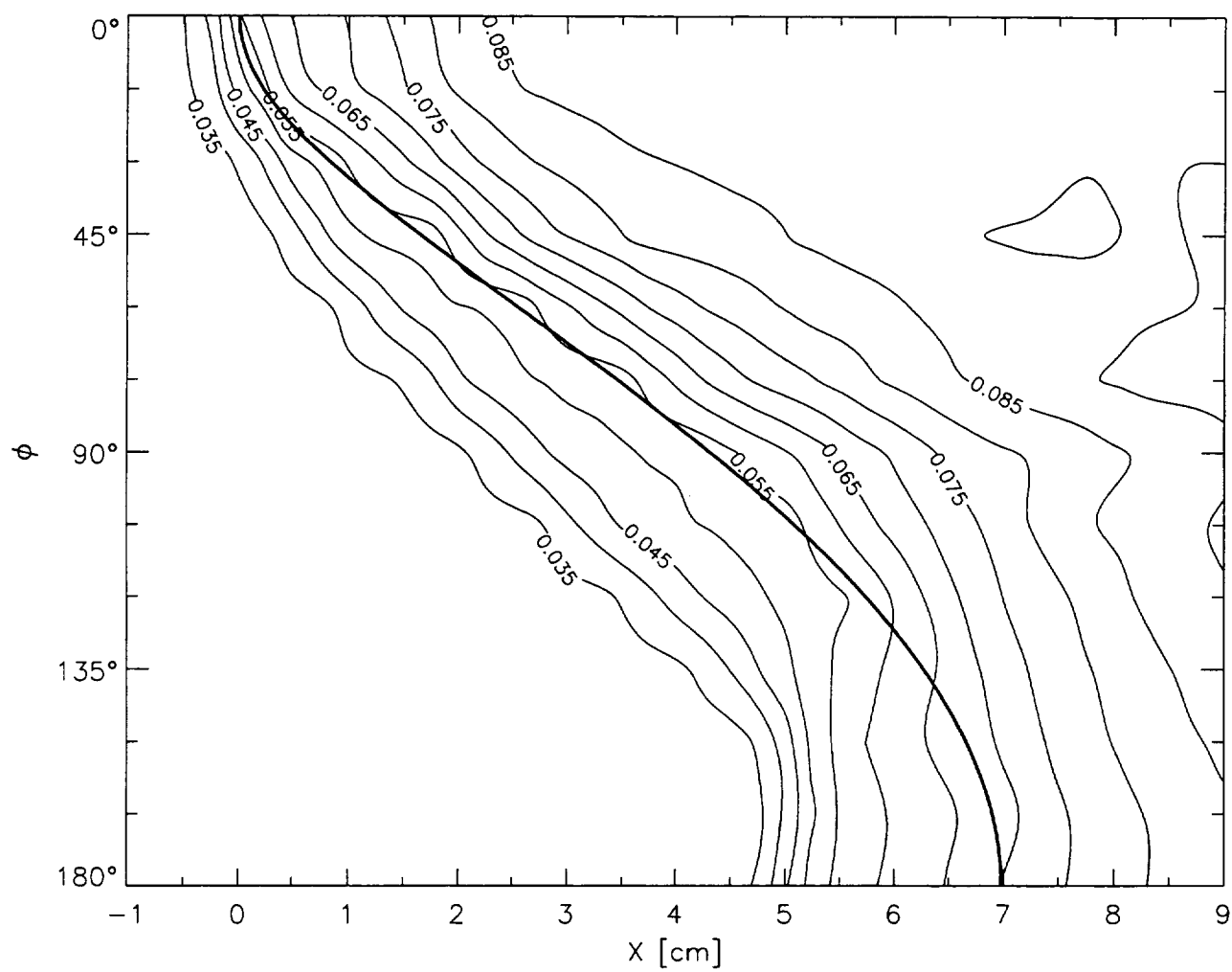
Figure 52. Surface pressure contour plot based on P/P_t.
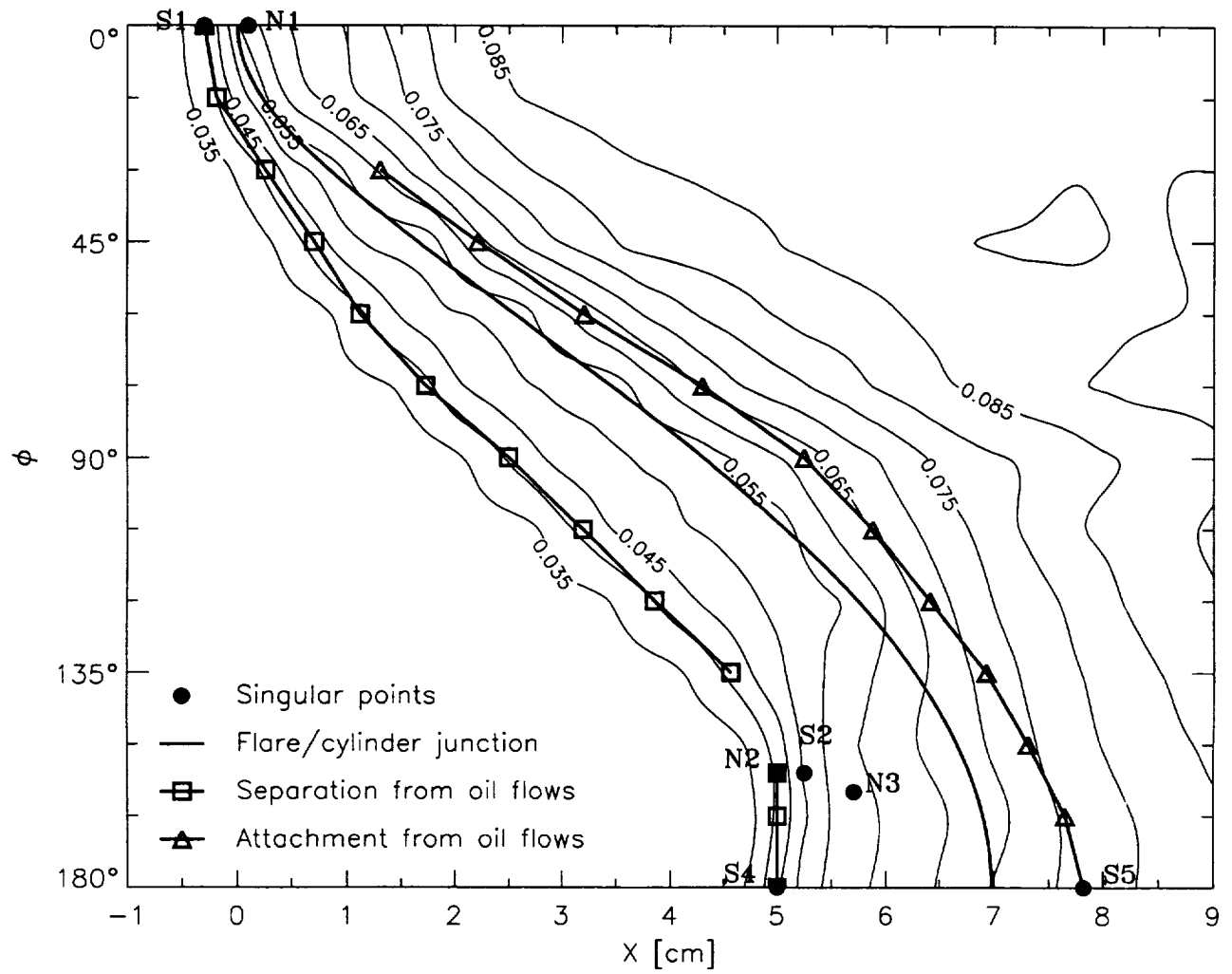
Figure 53. Surface pressure contour plot based on P/P_t along with oil-flow results.
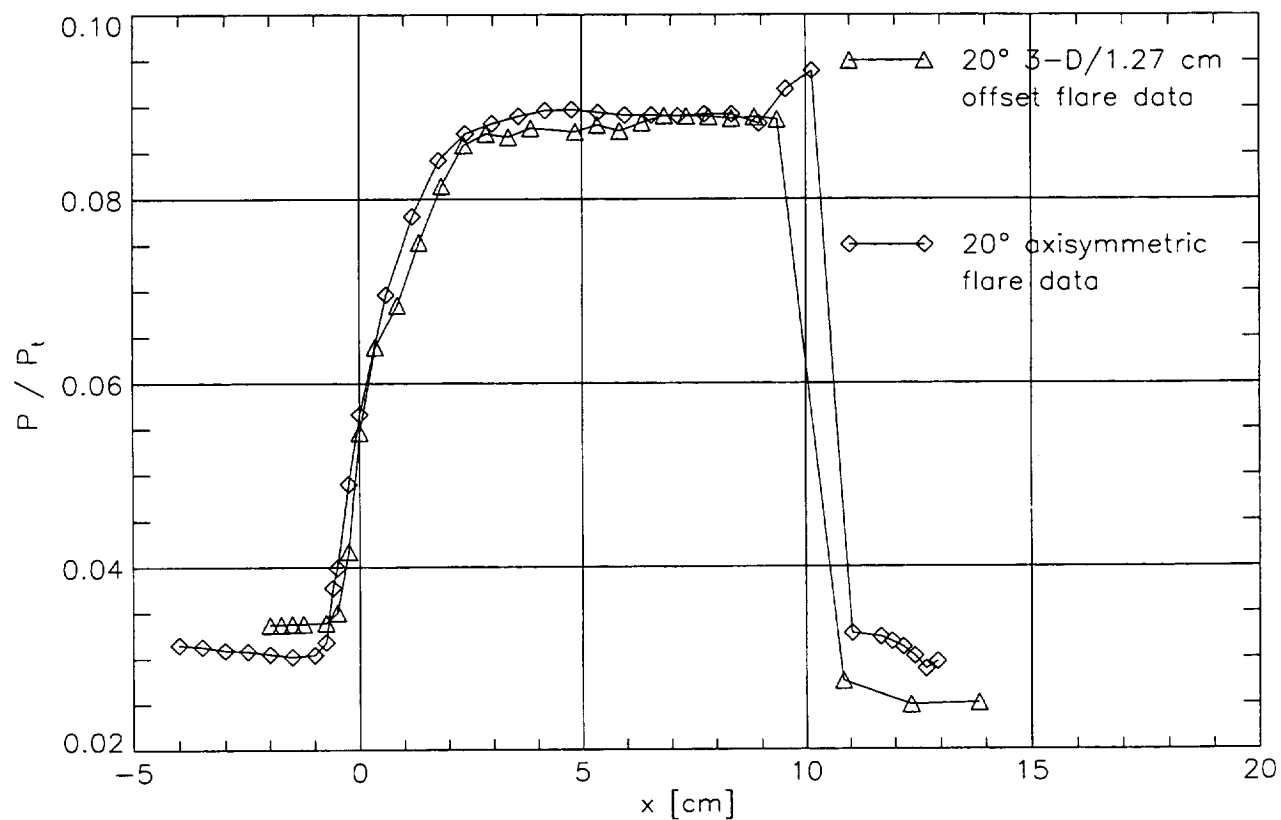
Figure 54. Pressure distribution for 20° axisymmetric flare and 20° 3-D/1.27 cm offset flare (along $\phi = 0°$ line of symmetry).
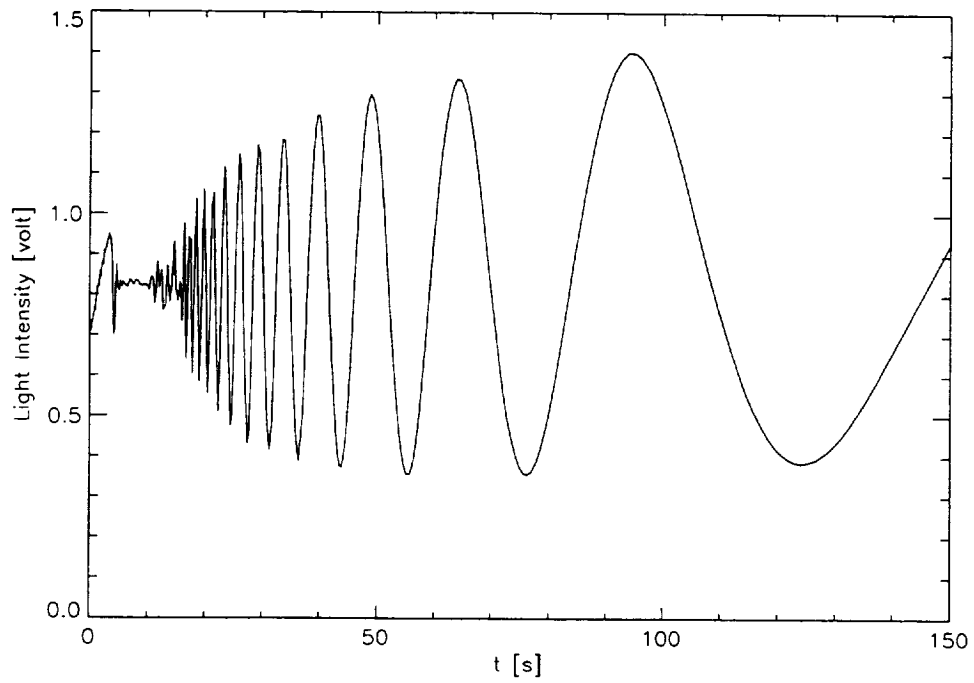
Figure 55. LISF signal from plastic surface over Monokote.
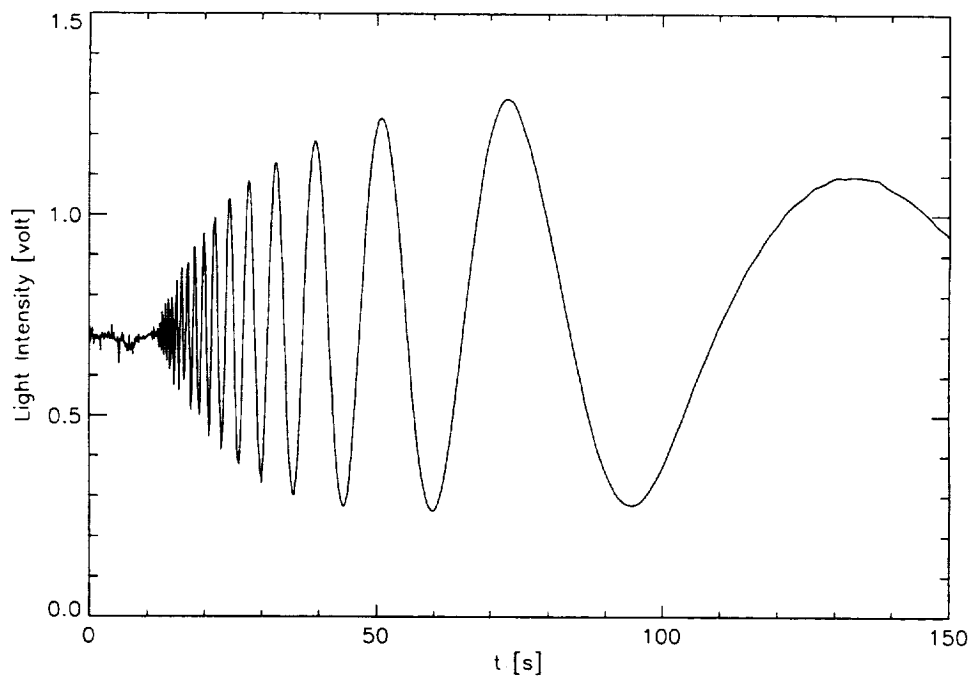
Figure 56. LISF signal from plastic surface over painted model.
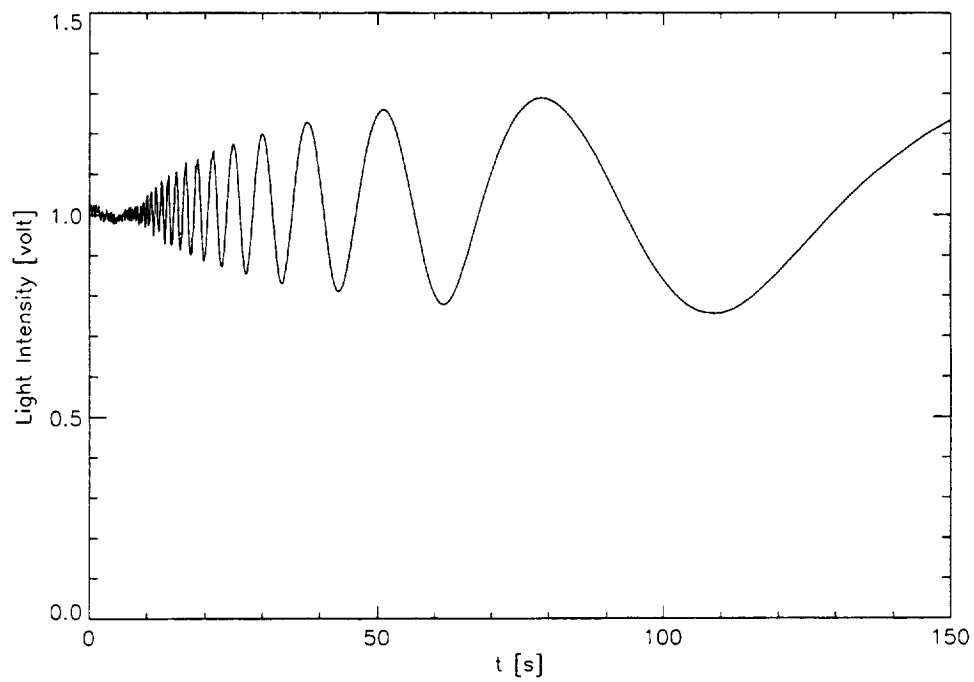
Figure 57. LISF signal from polished stainless steel.
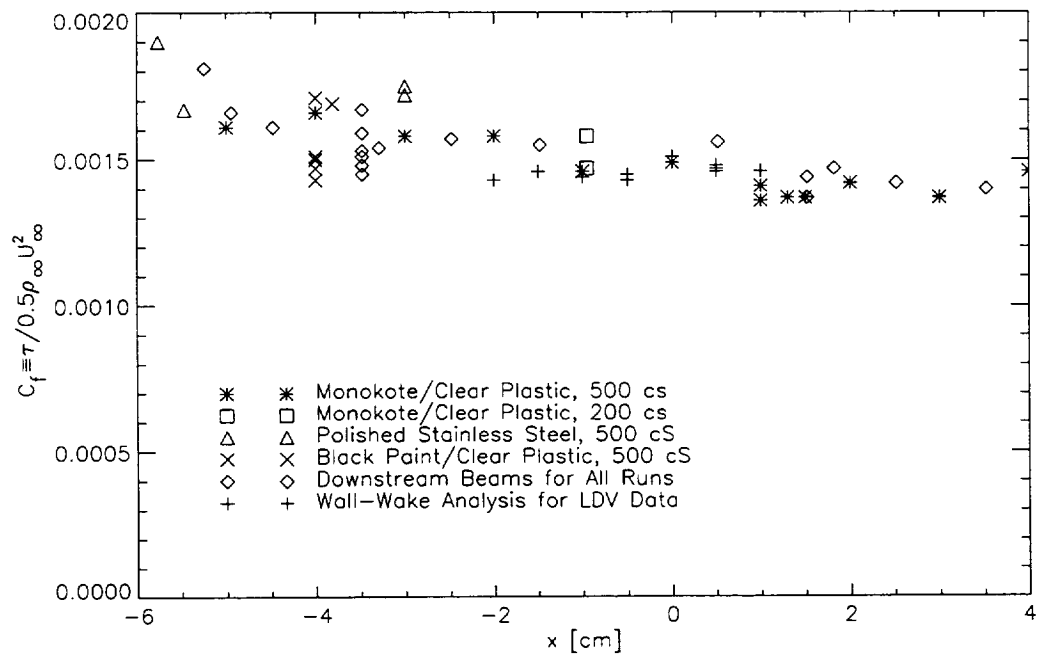
Figure 58. Skin-friction measurements in undisturbed boundary layer.
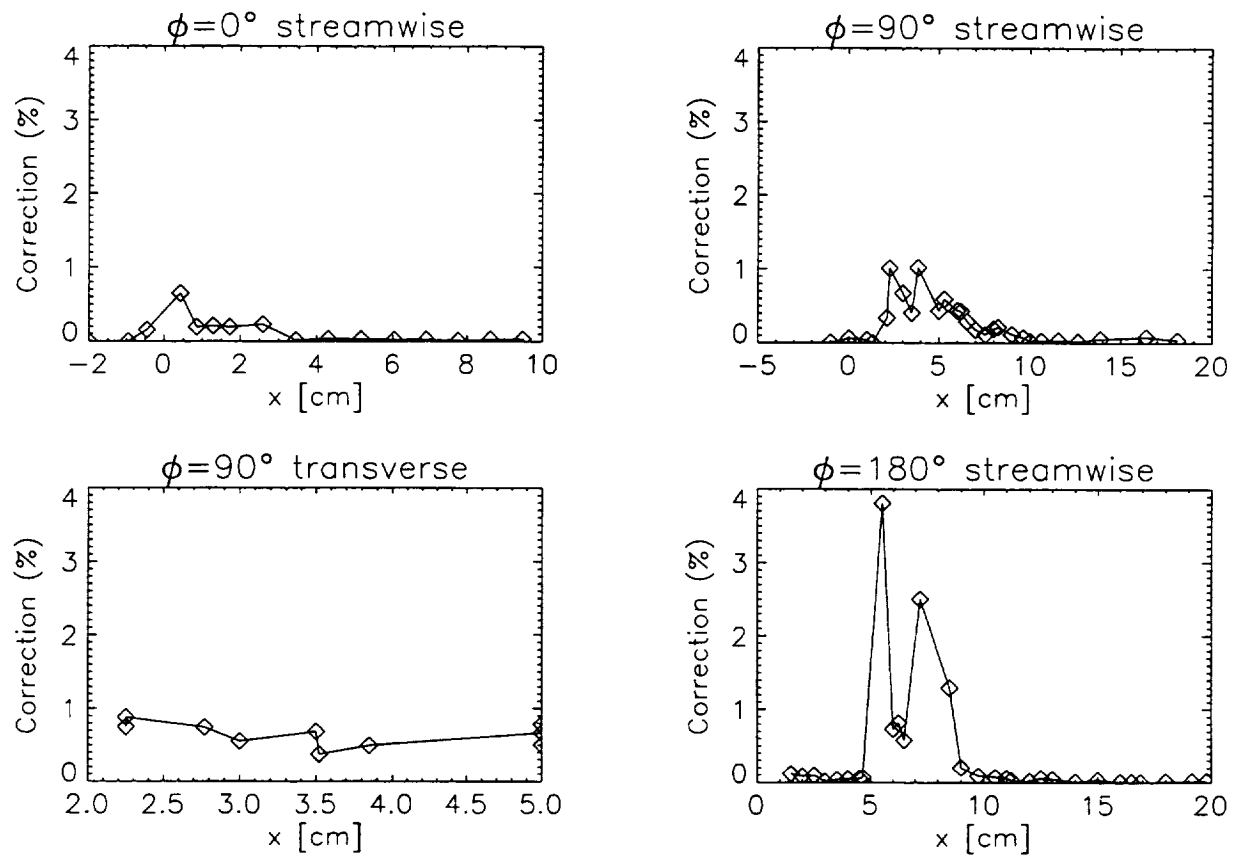
Figure 59. Value of correction factor at each LISF measurement location.
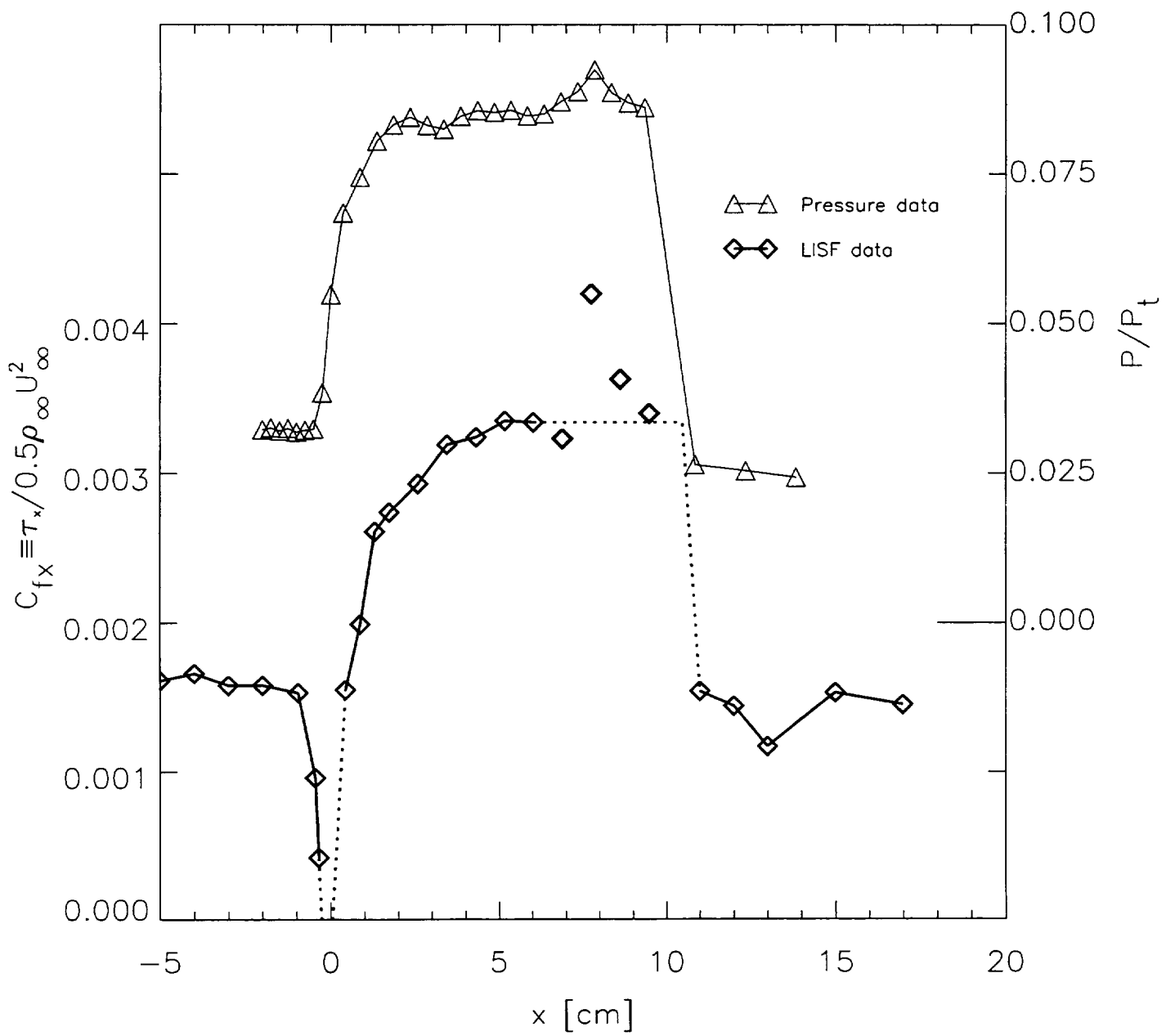
Figure 60. LISF streamwise skin-friction measurements along $\phi = 0°$.
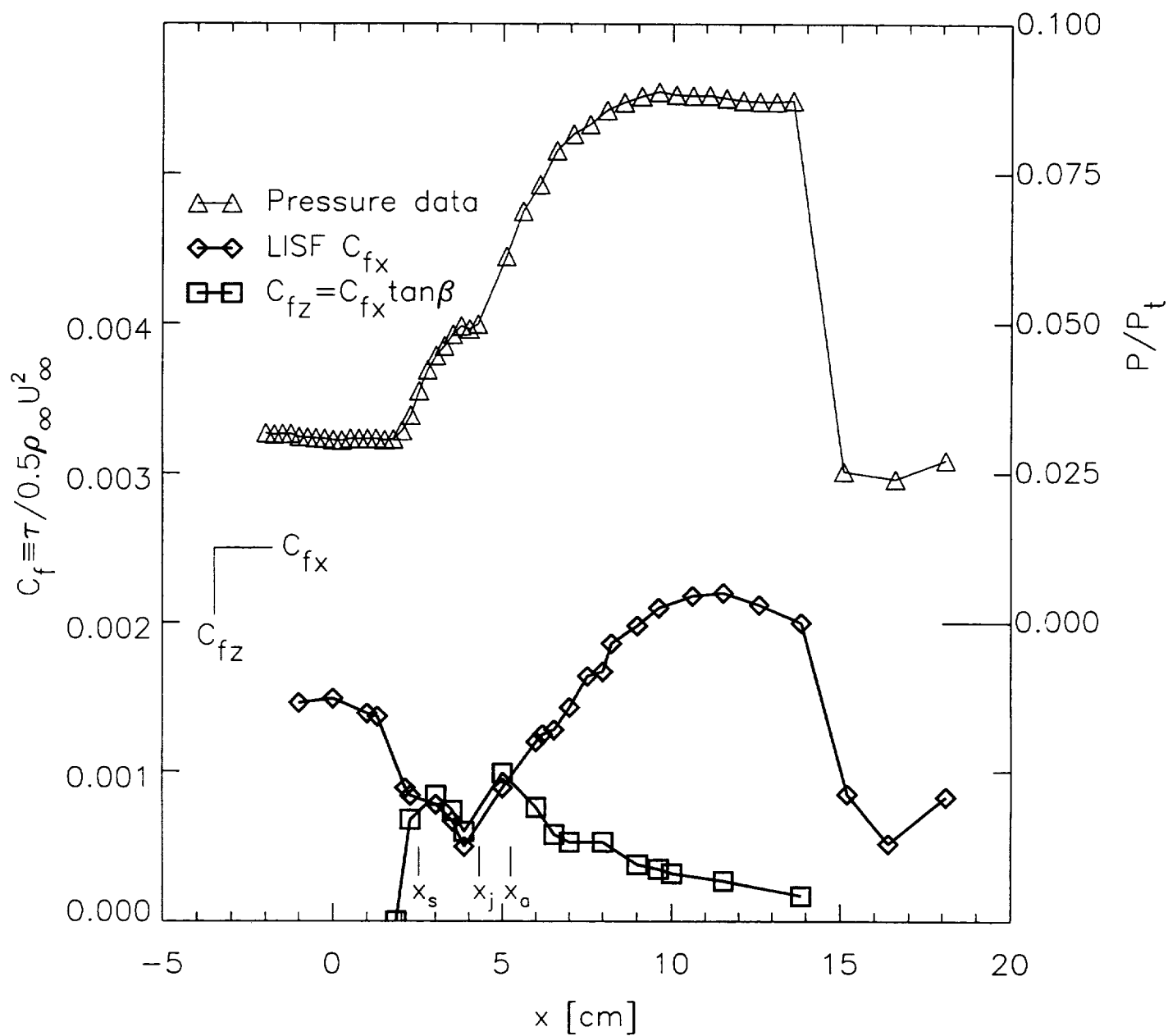
Figure 61. LISF streamwise and resolved transverse skin-friction measurements along $\phi = 90°$.
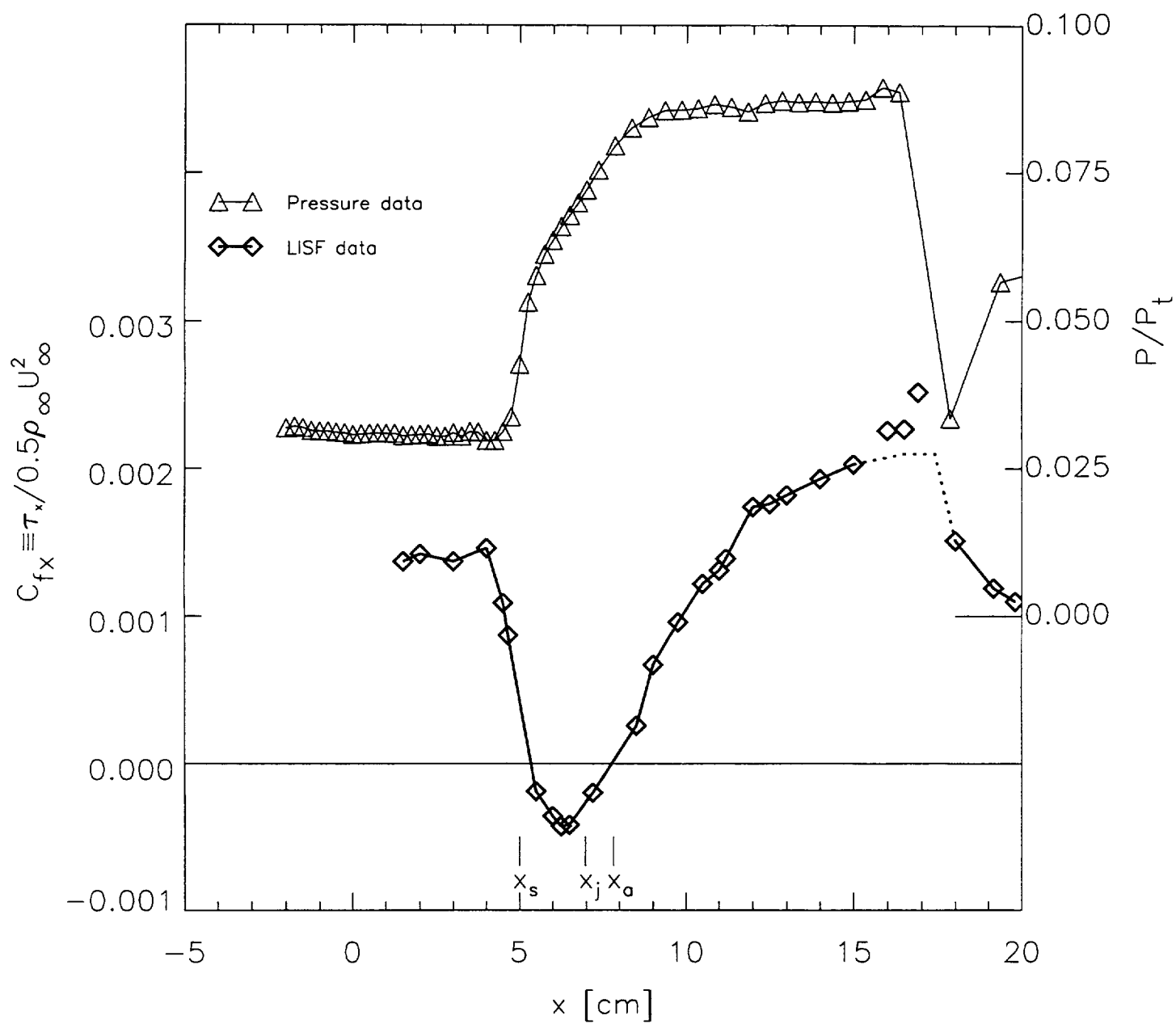
Figure 62. LISF streamwise skin-friction measurements along $\phi = 180°$.
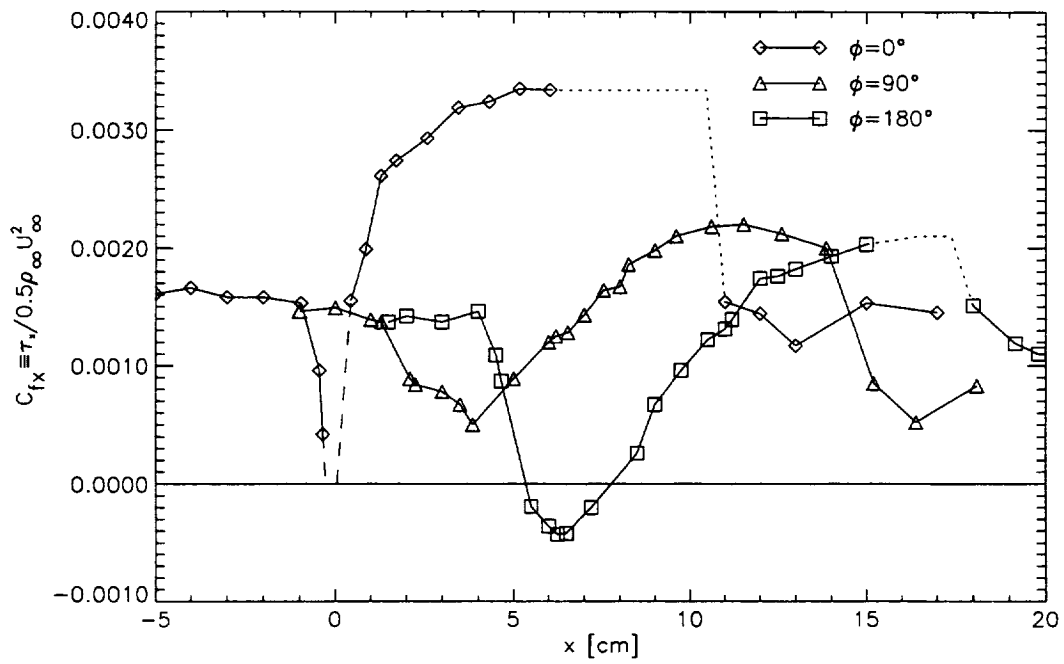
Figure 63. Streamwise skin-friction distributions along $\phi = 0°$, $90°$ and $180°$.
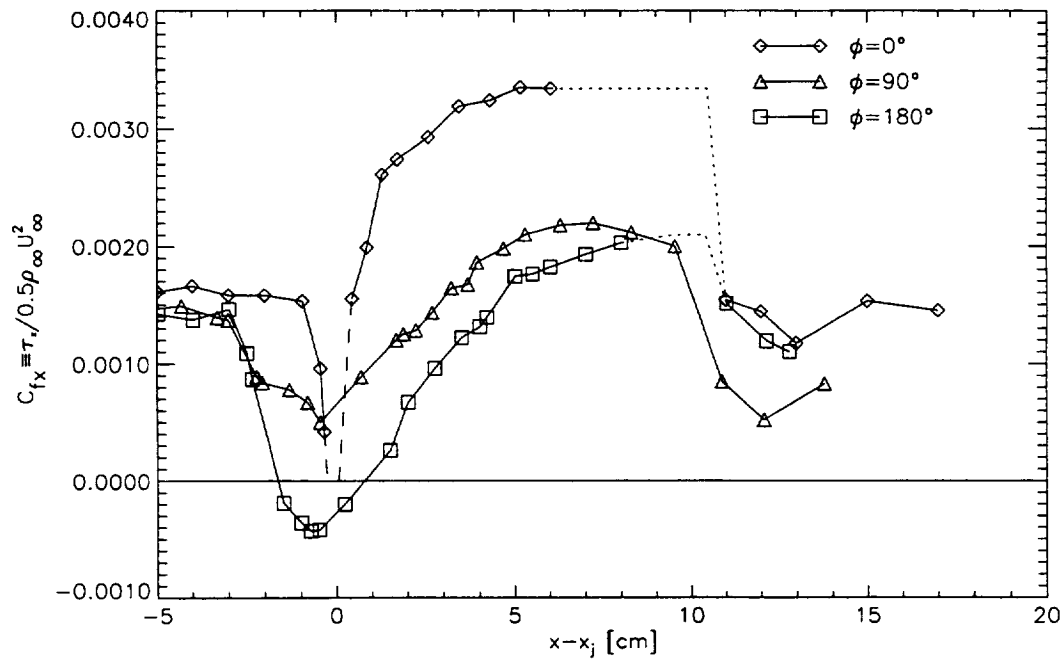
Figure 64. Streamwise skin-friction distributions along $\phi = 0°$, $90°$ and $180°$ with coincident cylinder-flare junctions.

REPORT DOCUMENTATION PAGE

Form Approved
OMB No. 0704-0188

1. AGENCY USE ONLY (Leave blank)	2. REPORT DATE June 1994	3. REPORT TYPE AND DATES COVERED Technical Memorandum

4. TITLE AND SUBTITLE

Surface Documentation of a 3-D Supersonic, Shock-Wave/Boundary-Layer Interaction

6. AUTHOR(S)

Jeffrey K. Wideman,* James L. Brown, John B. Miles,* and Oktay Özcan **

5. FUNDING NUMBERS

505-70-59

7. PERFORMING ORGANIZATION NAME(S) AND ADDRESS(ES)

Ames Research Center
Moffett Field, CA 94035-1000

8. PERFORMING ORGANIZATION REPORT NUMBER

A-94084

9. SPONSORING/MONITORING AGENCY NAME(S) AND ADDRESS(ES)

National Aeronautics and Space Administration
Washington, DC 20546-0001

10. SPONSORING/MONITORING AGENCY REPORT NUMBER

NASA TM-108824

11. SUPPLEMENTARY NOTES

Point of Contact: James L. Brown, Ames Research Center, MS 229-1, Moffett Field, CA 94035-1000; (415) 604-6229
*University of Missouri, Columbia, Missouri; **Istanbul Technical University, Istanbul, Turkey

12a. DISTRIBUTION/AVAILABILITY STATEMENT

Unclassified — Unlimited
Subject Category 34

12b. DISTRIBUTION CODE

13. ABSTRACT (Maximum 200 words)

The experimental documentation of a three-dimensional shock-wave/boundary-layer interaction in a nominal Mach 3 flow is presented. The model consisted of a sting-supported cylinder, aligned with the free-stream flow, and a 20° half-angle conical flare offset 1.25 cm from the cylinder centerline. Surface oil flow, laser light sheet illumination, and schlieren were used to document the flow topology. The data includes surface-pressure and skin-friction measurements. A laser interferometric skin friction instrument was employed to acquire the skin-friction data. Included in the skin-friction data are measurements within separated regions and 3-D measurements in highly-swept regions. The skin-friction data will be particularly valuable to turbulence modeling and computational fluid dynamics validation.

14. SUBJECT TERMS

Shock wave interaction, Turbulent boundary layer, Three-dimensional flow, Skin friction, Topology, Wind tunnel tests

15. NUMBER OF PAGES
136

16. PRICE CODE
A07

17. SECURITY CLASSIFICATION OF REPORT Unclassified	18. SECURITY CLASSIFICATION OF THIS PAGE Unclassified	19. SECURITY CLASSIFICATION OF ABSTRACT	20. LIMITATION OF ABSTRACT